МОСКОВСКИЙ ГОСУДАРСТВЕННЫЙ УНИВЕРСИТЕТ
ИМЕНИ М.В.ЛОМОНОСОВА
БИОЛОГИЧЕСКИЙ ФАКУЛЬТЕТ

На правах рукописи

Май Лиша

Молекулярное моделирование структурных перестроек канала KCNQ1 под влиянием биоактивных соединений и мутаций

Специальность 1.5.2. Биофизика

ДИССЕРТАЦИЯ
на соискание ученой степени
кандидата биологических наук

Научный руководитель:
кандидат физико-математических наук Новоселецкий Валерий Николаевич

Москва – 2026

LOMONOSOV MOSCOW STATE UNIVERSITY

BIOLOGICAL FACULTY

As a manuscript

Mai Lisha

Molecular Modeling and Structural Insights into KCNQ1 Channel Regulation by Bioactive Compounds and Mutations

Specialty 1.5.2 – Biophysics

DISSERTATION (THESIS)

for the Degree of Candidate of Biological Sciences

Supervisor, PhD

Valery N. Novoseletsky

Moscow – 2026

CONTENTS

1.Introduction

1.1. Relevance of the research topic

KCNQ1 channels play a vital role in cardiac repolarization through their assembly with auxiliary KCNE subunits, forming the slowly activating delayed rectifier current (I_{Ks}) that regulates heart rhythm stability [1, 2]. Therefore, the KCNQ1 potassium channel is the main target for treating long QT syndrome (LQTS) which causes approximately 1 in 2000 to 2500 individuals and can lead to sudden cardiac death [3]. Additionally, KCNQ1 mediates ionic and fluid homeostasis in epithelial tissues, where its activity is modulated by tissue-specific KCNE subunits [4, 5].

KCNQ1 activity is modulated by an integrated regulatory network including auxiliary subunits, membrane lipids, and intracellular signaling proteins. Co-assembly with KCNE subunits determines KCNQ1 voltage dependence, gating kinetics, and pharmacological sensitivity, enabling tissue-specific modulation [6]. The membrane phospholipid phosphatidylinositol 4,5-bisphosphate (PIP_2) is a vital lipid cofactor that transduces voltage-sensor (VSD) movements driven by changes in membrane potential to opening of the pore domain (PD) [7, 8]. Regulation also involves the long intracellular C-terminal domain of KCNQ1, which determines binding to calmodulin (CaM) for proper folding, assembly, and trafficking [9, 10]. This C-terminal domain also provides an anchoring platform for Yotiao (AKAP9) to mediate phosphorylation-dependent modulation of IKs at key sites such as Ser27 when experiencing β-adrenergic stimulation [11, 12]. Although recent cryo-electron microscopy (cryo-EM) structures [7, 13-15] have enhanced our understanding of KCNQ1 complexes, several mechanistic aspects of KCNQ1 modulation and dysfunction remain incompletely resolved.

A critical unresolved question is how the same small molecule can exert different effects depending on the auxiliary subunit of KCNQ1, such as mallotoxin (MTX). The natural compound MTX reflects this complexity by producing dual regulatory functions. It can increase currents through KCNQ1-KCNE1 while inhibiting those mediated by KCNQ1-KCNE3 [16, 17]. This difference suggests that subunit-dependent structural features and electrostatic environments affect ligand action, but the molecular mechanism responsible for the dual modulation of MTX remains insufficiently understood.

Furthermore, despite recent advances, the full structure of the KCNQ1 channel has not been completely resolved. The C-terminal domain of KCNQ1 connecting helix C (HC) and helix D (HD), the HC-HD linker (approximately residues 535-625), is thought to be flexible but functionally important, including for interaction with Yotiao (AKAP9). Disease-causing mutations within this region have been reported to disrupt Yotiao binding and cause long QT syndrome type 1 (LQT1) [18, 19], highlighting the importance of understanding the conformation and dynamics of this linker region. However, this region is frequently poorly resolved and missed in current cryo-EM atomic structures, encouraging computational strategies to reconstruct and validate plausible structural models.

In addition to structural gaps, characterizing the molecular basis of diseases is also essential. Familial dysfunction of KCNQ1 is a leading cause of LQT1 and is also linked to atrial fibrillation. In the VSD region, the disease-causing variants D242N [20] and R243H [21] impair channel function and are expected to perturb the stability of KCNQ1 channel complexes and the interaction that facilitates VSD-PD coupling. In particular, PIP_2, which is positioned at the interface between KCNQ1 and KCNE3, plays the central role in coupling and exert influence on auxiliary subunits such as KCNE3 on channel gating. Consequently, these two mutations (D242N and R243H) are expected to alter electrostatic environment and interfacial interactions, potentially altering hydrogen-bond interaction networks and lipid contacts. Moreover, direct molecule modulation of KCNQ1 is an important therapeutic objective. While an intrinsic activator, ML277, has been described [22, 23], several naturally derived compounds, including tanshinone IIA [24, 25], resveratrol [26], and quercetin [27], have also been found to influence KCNQ1 activity.

Finally, KCNQ1 is also susceptible to environmental factors like oxidative stress. Reactive oxygen species (ROS) can oxidize residues of KCNQ1, notably Cys214, weakening channel stability [28]. Extract screening of Medicine and Food Homology (MFH) resources have identified *Eucommia ulmoides* (*E. ulmoides*) as a leading antioxidant candidate, and its major constituents, quercetin and rutin, may excert a protective effect through direct interaction with redox-sensitive regions.

1.2. Development of the research topic

In recent years, cryo-EM methods have been used to decipher several structures of the KCNQ1 channel in various states, but the structure of some of its fragments remains largely unknown. One such fragment consists of intracellular helices C and D and the linker between them (HC–HD linker) (residues 535–625). The structure of the individual C and D helices is considered to be known, while only low-resolution electron density maps are available for the linker. However, it is known that this linker is necessary for interaction with the Yotiao scaffold protein, which, in turn, binds to protein kinase A (PKA) to modulate the phosphorylation of the KCNQ1 channel. Unsurprisingly, mutations in this linker disrupt the assembly of the KCNQ1/Yotiao/PKA complex, causing long QT syndrome type 1 (LQT1) (Li et al., 2019). The lack of high-resolution data on the structure of the linker, as well as its molecular model, is an obstacle to understanding the channel regulation processes that depend on binding to Yotiao.

More than two hundred mutations associated with various diseases have been described for the KCNQ1 subunit, and its dysfunction causes LQT1 syndrome, atrial fibrillation, and other life-threatening arrhythmias. The pathogenic mutations D242N and R243H in the KCNQ1 subunit are located in the region of its interaction with the KCNE1 (KCNE3) subunits and the phospholipid PIP2 (Fig. 1). However, the molecular mechanisms by which these mutations disrupt the interactions of the main KCNQ1 subunit with the additional KCNE1 (KCNE3) subunits and the phospholipid PIP2 remain poorly understood.

Another cause of KCNQ1 channel dysfunction is oxidative stress. In particular, this may be associated with the oxidation of the Cys214 residue on the extracellular side of the S3 helix, which alters the kinetics of the channel and destabilizes the tetrameric assembly (Kerst et al., 2002; Bates et al., 2023). In this regard, it is noteworthy that the KCNQ1 channel is also modulated by some antioxidants (Redford & Abbott, 2020), but the molecular mechanism of this effect remains unknown. It can be assumed that the binding of antioxidants in close proximity to the Cys214 residue could prevent its oxidation and thus contribute to the preservation of channel function.

As already mentioned, the molecular mechanisms of activity of many natural biologically active compounds with respect to the KCNQ1 channel remain poorly understood. According to some reports, such natural compounds activate the KCNQ1 channel (Yan et al., 2023), but their binding sites remain unknown. At the same time, these compounds are active components of many plant extracts (such as extracts of *E. ulmoides*, *C. officinalis*, etc.), known for their antioxidant capacity.

Therefore, this dissertation employs an integrated workflow combining electrostatic profiling, structure-guided modeling, molecular docking, and all-atom molecular dynamics (MD) simulations, complemented by biochemical assays to examine the functional modulation of KCNQ1 from different perspectives. The study progresses from explaining the KCNE-dependent pharmacology of MTX to reconstructing the unresolved HC-HD linker and quantifying mutation-driven perturbations within the KCNQ1-KCNE3-PIP2 complex. Furthermore, it characterizes the binding interactions of bioactive activators and is extended to environmental antioxidant protection by probing quercetin and rutin as protectants against ROS. These findings may provide a comprehensive framework for understanding KCNQ1 pathophysiology and guiding the development of therapeutics for ionic channelopathies.

1.3. Aims and objectives of the study

The aim of this study is to elucidate the molecular structure of the KCNQ1 channel and its complexes with KCNE family subunits, as well as the structural regulations induced by various bioactive compounds (including antioxidants) and pathogenic mutations.

To achieve this goal, the following objectives were set:

1. Investigate the molecular basis of the dual effects of MTX on KCNQ1-KCNE1 and KCNQ1-KCNE3 complexes using molecular modeling.
2. Construct a structural model of the HC-HD linker in the C-terminal domain of KCNQ1 channel using advanced molecular modeling approaches based on previously published cryo-EM electron density maps.
3. Study the effects of certain KCNQ1 channel mutations (D242N and R243H) associated with LQT1 syndrome on the structural stability and dynamics of the KCNQ1-KCNE3 complex using all-atom molecular dynamics simulations.
4. Identify potential binding sites for natural KCNQ1 channel activators, including tanshinone IIA, resveratrol and quercetin.
5. Quantitatively assess antioxidant capacity in nine plant extracts, identification of the most active extract, and exploring of potential binding mechanisms for their bioactive compounds (specifically rutin and quercetin) to the KCNQ1 channel, to investigate their potential protective functions against oxidative stress.

1.4. Scientific novelty

Using molecular modeling approaches, several features of the structure of the KCNQ1 channel and its complexes with KCNE family subunits were analyzed, as well as the structural rearrangements induced by a number of biologically active compounds and pathogenic mutations. The molecular basis of the bidirectional modulation of the KCNQ1/KCNE1 and KCNQ1/KCNE3 channels by mallotoxin was identified. Based on previously published low-resolution data, a structural model of the HC-HD linker of the C-terminal domain of KCNQ1 was proposed. Using the pathogenic mutations D242N and R243H in the KCNQ1 subunit as examples, the effects of amino acid substitutions on changes in the compactness of the channel molecule, as well as on changes in the free-energy landscape, were examined. In addition, changes in interactions with PIP2 molecules were investigated. A systematic experimental comparison of the antioxidant capacity of nine plant extracts was performed, and the *E. ulmoides* extract was identified as the most active. Putative binding sites for natural activators of the KCNQ1 channel (quercetin, tanshinone IIA, and resveratrol) were identified. For rutin and quercetin, which are components of the *E. ulmoides* extract, a molecular mechanism of antioxidant action with respect to the KCNQ1 channel was proposed.

1.5. Theoretical and practical significance of the work

The developed model of the flexible HC-HD linker provides a basis for studying the structure of the KCNQ1/Yotiao/PKA complex and the phosphorylation of residues in the N-terminal domain of the KCNQ1 channel. Analysis of conformational and dynamic changes caused by the pathogenic mutations D242N and R243H deepens our understanding of KCNQ1 channel function and makes it possible to outline new therapeutic approaches for LQT1. Using natural bioactive substances as examples, it is shown that their binding sites may be located both on the extracellular surface of the KCNQ1 channel molecule and on the surface facing the membrane. The diversity of binding sites helps to explain both the activating and the antioxidant effects of quercetin on the KCNQ1 channel. Experimental investigation of plant extracts demonstrates their high potential as a source of natural compounds active toward the KCNQ1 channel. The approaches proposed in this work for identifying binding sites of low-molecular-weight compounds to KCNQ1 facilitate the development of new selective modulators of this channel for the treatment of LQT1 and atrial fibrillation.

1.6. Methodology

Biophysics: molecular modeling was used to refine experimentally determined structures of KCNQ1 and its complexes, to calculate electrostatic potential, to perform molecular docking of ligands, to perform fitting of atoms into cryo-EM density map, to perform molecular dynamics simulation; Total Phenolic Content (TPC) measurements, Ferric Reducing Antioxidant Power (FRAP) Assay and Lipid Peroxidation Assay (MDA Quantification) were used to characterize antioxidative properties of plant extracts.

1.7. Provisions put forward for the defense

1. Calculating the electrostatic potential distribution near protein surfaces clarifies the binding sites of charged ligands and reveals their regulatory effects. The inhibitory effect of mallotoxin on the KCNQ1-KCNE3 complex results from the binding of its negatively charged molecule within a region of high positive electrostatic potential in the channel pore, whereas the stabilizing effect on the open state of the KCNQ1-KCNE1 complex results from binding in analogous regions at the periphery of the complex’s transmembrane domain. When calculating electrostatic potential, it is essential to consider negatively charged PIP_2 molecules bound to KCNQ1 subunits in both complexes.

2. Analysis of low-resolution electron density maps combined with molecular modeling methods makes it possible to obtain models of flexible fragments of protein structures. In the interface region between the HC and HD coiled-coil domains of KCNQ1, a circular swap-domain within the tetramer is present, in which helices from neighbouring subunits form a “supercoil” (coiled-coil) configuration.

The helical structure of the linker itself explains the flexibility of the HC-HD junction and provides new opportunities for studying the Yotiao-mediated macromolecular complex. The pathogenic mutations D242N and R243H in the KCNQ1 subunit destabilize the KCNQ1-KCNE3 complex in ways by increasing the conformational flexibility of the voltage-sensing domain, with the R243H mutation causing a more substantial structural perturbation.

3. The integration of experimental approaches and molecular modeling techniques helps explore the biological activity of plant extracts. The binding sites of key antioxidant components from *E. ulmoides* (rutin, and quercetin), are located in close proximity to the redox-sensitive Cys214 residue of the KCNQ1 channel, which supports a structure-based hypothesis for potential antioxidant protection of this site under oxidative-stress conditions. Furthermore, quercetin, tanshinone IIA, and resveratrol activate the KCNQ1 channel by binding to a conserved site formed by the helical linker S4-S5 and the helices S5 and S6 of the pore domain.

1.8 Degree of reliability and validation

The reliability of the results and conclusions presented in this dissertation is confirmed by the use of modern methods of computational biophysics and biochemistry, the publication of key results in peer-reviewed scientific journals, and their presentation and discussion at international scientific conferences.

The main results of the dissertation are published in four scientific articles in peer-reviewed journals indexed in international (Web of Science, Scopus) and national (Russian Science Citation Index - RSCI) databases. These publications are included in the list of journals recommended by the Dissertation Council of Lomonosov Moscow State University in the specialty 1.5.2. Biophysics.

The results of the dissertation were presented for expert discussion and review at nine international scientific conferences and forums. The most significant of these results were presented at scientific events in Moscow: at forums held with the support of the Education Department of the Chinese Embassy in Russia, including the Vorobyovy Gory International Forum for Young Students and Scientists (2023, 2024) and the All-Russian Scientific Forum of Chinese Students (2023); at the International Conference “BIOMEMBRANES 2024” organized by the Moscow Institute of Physics and Technology. Additional results were presented and discussed at a number of conferences held at the Moscow State University-PPI University in Shenzhen (China): the Lomonosov International Scientific Conference (2022, 2023); 3rd International Conference “Modern Trends and Achievements in Life Sciences” (2023); 2nd International Conference and School on Nanobiotechnology (2022); 1st International Student Conference on Biology (2021).

2. Literature Review

2.1 The KCNQ Family and KCNQ1 Channel Architecture

2.1.1 Overview of the KCNQ Family

The KCNQ family consist of five voltage-dependent potassium channel subunits, frequently designated as Kv7.1 to Kv7.5 or KCNQ1 to KCNQ5. KCNQ channels possess a conserved trans-membrane organization and adopt tetrameric arrangement with four subunits, either homomeric or heteromeric, constituting a central ion-conduction pore. Each subunit comprises six transmembrane helices (S1 to S6) that can be grouped into two functional modules: the voltage-sensing domain (VSD, S1 to S4) and the pore domain (PD, S5 and S6 together with the intervening pore loop). The VSD reacts to changes in membrane potential, with the S4 helix serving as the principal voltage-sensing function through a series of positively charged residues. The PD forms the selective potassium permeation pathway, including the selectivity filter situated within the pore loop between S5 and S6 (Figure 1).

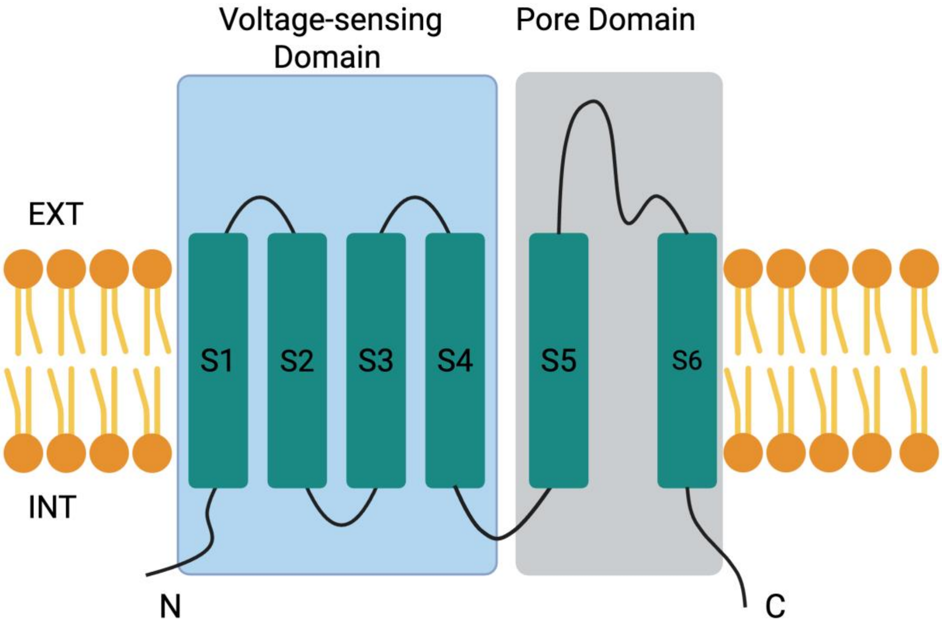

Figure 1. Schematic representation of a single KCNQ channel subunit. The schematic illustrates the arrangement of a single KCNQ subunit within the cell membrane, which separates the extracellular (EXT) and intracellular (INT) environments. The subunit polypeptide chain consists of six transmembrane helices (labeled S1-S6), with both the amino (N) and carboxyl (C) termini located in the intracellular space. These helices are organized into two principal domains: the Voltage-Sensing Domain (VSD), comprising helices S1-S4, and the Pore Domain (PD), comprising helices S5 and S6. The extracellular loop between S5 and S6 forms the P-loop, a critical component of the ion selectivity filter.

KCNQ channels function as key regulators of cellular excitability, having substantial physiological influence in various cell types. Their main function is to control the flow of potassium ions to move out of the cell, which helps maintain the resting membrane potential stability and is modulated in depolarizing impulses. This activity is vital for regulating neuronal excitability and for ensuring the timely repolarization of cardiomyocytes [1]. In cardiac tissue, KCNQ1 co-assembles together with KCNE1 to generate the slow delayed rectifier current (IKs), which is required for the repolarization phase of the action potential, as illustrated in Figure 2. Impairment of I_{Ks} can prolong the repolarization interval, which increases the risk of arrhythmias.

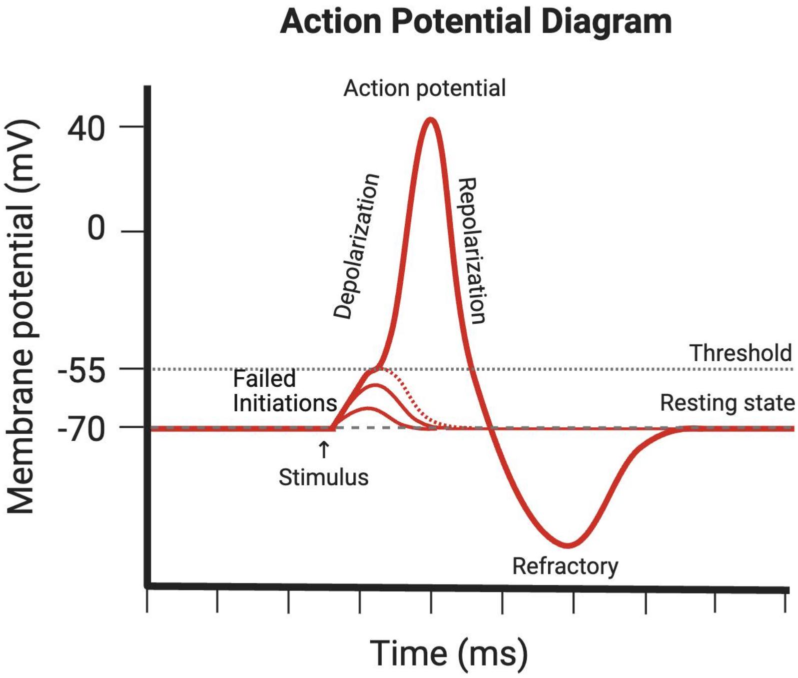

Figure 2. Schematic of a cardiac action potential. Potassium efflux through repolarizing currents, including IKs carried by KCNQ1-KCNE1 complexes, contributes to action potential repolarization.

These five subtypes (KCNQ1-KCNQ5) display different tissue localization, which, in turn, determines their subtype-specific physiological roles and the disease traits in the event of dysfunction. For instance, KCNQ2 and KCNQ3 are mainly found in the nervous system, where they co-assemble to form the heterotetrameric M-channels, acting as slow-activating regulators of neuronal excitability [29]. The M-current can suppress neuronal firing, thereby limiting hyperexcitability, e.g., epileptic seizures. In comparison, KCNQ1 is enriched in the heart, where it is crucial for the repolarization phase of the cardiac action potential, and is present in inner ear and the epithelial tissues. KCNQ4 plays a critical role in auditory function [30], while KCNQ5 is expressed in both the central nervous system and smooth muscle. This tissue specificity highlights the diverse channelopathies arising from genetic mutations in KCNQ genes, as summarized in Table 1. These hereditary disorders display as pathologies like cardiac arrhythmias, epilepsy, or deafness, depending on the related subtype.

Table 1. Tissue distribution and disorders associated with KCNQ subtypes

KCNQ Subtype	**Expression Distribution**	**Associated Disorders**
KCNQ1	Cochlea, Heart, Pancreas, Kidney	Type 1 long QT syndrome, Jervell and Lange-Nielsen syndrome, Atrial fibrillation [1, 3, 31]
KCNQ2	Cerebellum, Hippocampus, Medulla, Cortex	Benign familial neonatal seizures, Early onset epileptic encephalopathy, Intellectual disability [32, 33]
KCNQ3	Cerebellum, Hippocampus, Medulla, Cortex	Benign familial neonatal seizures, Early onset epileptic encephalopathy, Autism spectrum disorder [29]
KCNQ4	Cochlea, Trigeminal ganglia, Vestibular system	Autosomal dominant deafness (DFNA2), Noise-induced or age-related deafness [30]
KCNQ5	Retinal pigment epithelium, Hippocampus, Cortex, Skeletal muscle	Epileptic encephalopathies, Epilepsy, Intellectual disability [33, 34]

Considering their physiological importance, the impairment of these functions by genetic mutations results in a group of hereditary diseases referred as channelopathies. Clinically, these conditions present as a variety of pathological outcomes, such as cardiac arrhythmias, epilepsy, or hearing loss, depending on which subtype is involved, as outlined in Table 1. Owing to their substantial clinical relevance, these channels are widely regarded as strategic targets for the development of new pharmacological therapies. The identification of KCNQ channel activators, notably including the anticonvulsant retigabine, has supported their value as drug targets. Current efforts aim at exploring the potential of targeting these channels across a broader range of indications, including major depressive disorder [35] and hypertension [36].

2.1.2 KCNQ1 Architecture and Functional Domains

Transmembrane Domains: Voltage-sensing and pore domains

The KCNQ1 potassium channel is essential for normal cardiac rhythm. Its gating mechanism relies on the coordinated action of its transmembrane regions, specifically including the VSD and the PD. Particularly, PIP_2 acts as a critical cofactor that modulates electromechanical (E-M) coupling between VSD and PD, through an indirect, voltage-dependent mechanism. The movement of the VSD does not trigger the pore opening by the S4-S5 linker in a simple mechanical pull. Rather, the primary role of VSD is to control the accessibility of PIP_2 binding site located at the interface between the VSD and PD [14]. Under the condition of hyperpolarized potentials, the VSD adopts a down state that sterically prevents PIP_2 from binding, while at the condition of depolarization, the VSD transitions to the up state, thereby exposing the binding site to the environment and facilitating PIP_2 binding.

This PIP_2 engagement is the key step that translates voltage-sensor movement into pore dilation. The interaction of PIP_2 with residues in the S4-S5 linker and the C-terminus of S6 sets off sequential conformational changes that propagate to the pore-opening transition. This process leads to the bending of the S6 helices, increasing the pore radius for potassium flux. This E-M coupling is thus indirect and allosterically governed by PIP_2. MD simulations and structural models have further improved the understanding of the specific interacting residues involved in this crucial VSD-PD interface. Furthermore, the complexity of this system is heightened by the co-assembly of KCNQ1 with single-transmembrane KCNE subunits, including the canonical KCNE1-KCNE5 and the more recently identified KCNE6 [37] (Figure 3). These auxiliary proteins are integral modulators in the gating process. KCNE1, for example, shifts the kinetics and voltage-dependence of activation via modulation of the VSD-pore coupling, while KCNE3 can hold the VSD in its activated state, leading to a constitutively open channel. Accordingly, the transmembrane domains of KCNQ1 do not functionally independent but rather as an integrated unit. The VSD acts as a voltage-sensitive gate for a PIP_2-dependent activation signal, and the pore responds to this signal to control ion flow. Such KCNE-mediated modulation enables highly regulated channel activity, which is essential for its various physiological roles.

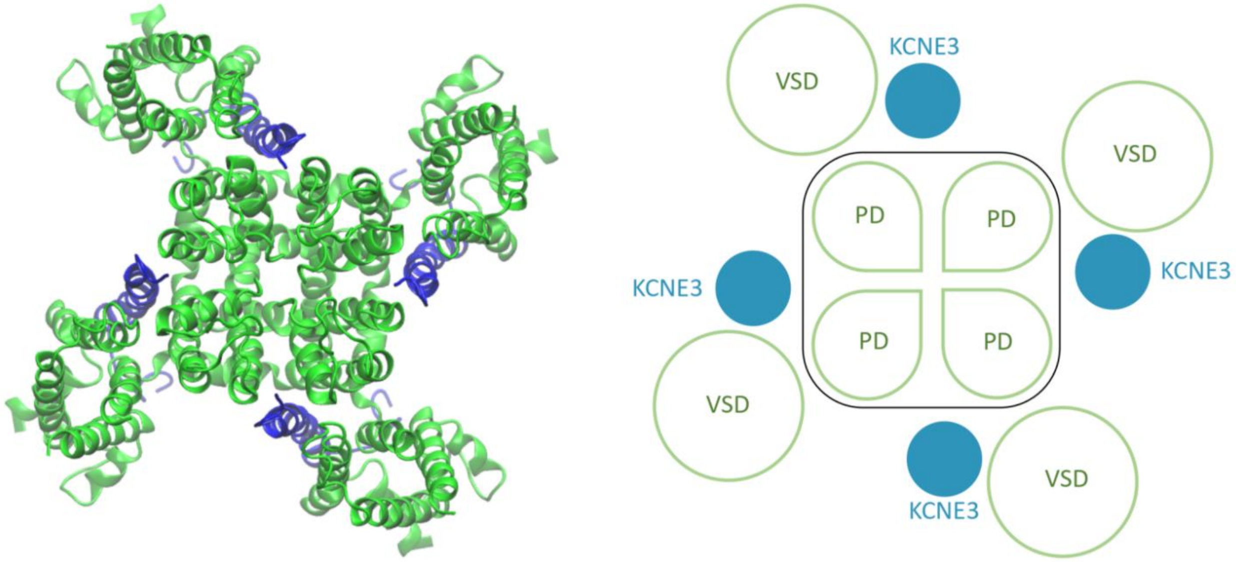

Figure 3. Cryo-EM structure of transmembrane domain of the KCNQ1-KCNE3 heteromeric channel (PDB ID 6V01) (extracellular view): The main KCNQ1 subunit (shown in green) with additional KCNE3 subunits (shown in blue) (left: molecular visualization in ribbon view; right: schematic representation). VSD = voltage-sensing domain; PD = pore domain (the selective filter is located at the center of the pore domain tetramer and not labeled).

The Intracellular C-Terminal Domain

While the transmembrane regions determine ion permeation and response to voltage change, the large intracellular C-terminal domain of KCNQ1 is a distinguishing feature of the Kv7 subfamily. This extensive domain acts as a regulatory platform that modulates channel assembly, trafficking, and is a critical site for channel modulation by various cellular factors. Understanding the structure-function relationships within this domain is important for understanding both physiological gating, normal channel function and pathological mechanisms in cardiac channelopathies.

Structural Architecture of the KCNQ1 C-terminal Domain

The KCNQ1 C-terminal domain is featured by four main alpha-helical segments termed Helix A (HA, residues ~372–429), Helix B (HB, residues ~460–500), Helix C (HC, residues ~537–563), and Helix D (HD, residues ~588–625), connected by linker regions of variable lengths and conformational flexibility [9, 38]. This domain has two functionally distinct regions: the proximal portion (comprising HA and HB) is the principle site for CaM binding and is essential for correct functional expression and folding, while the C-terminal distal half (including HC and HD) guides tetramerization via tandem coiled-coil motifs and facilitates trafficking to the plasma membrane [9, 10]. The distal half employs an assembly mechanism where the first coiled-coil complex forms dimeric intermediates that then self-associate into paired-dimer assemblies, while the outer helical bundle forms a parallel tetrameric coiled-coil structure with these structures acting in a coordinated manner to stabilize the tetrameric assembly of the channel [9].

Significantly, a major structural knowledge gap regarding the distal C-terminal distal half, where the HC-HD linker remains poorly defined in cryo-EM studies. Of particular interest is the HC-HD linker (residues ~564-587), which has long posed challenges for high-resolution structure determination due to its intrinsic flexibility. This region features essential motifs for regulatory interactions and provides a structural platform for the scaffolding protein Yotiao and macromolecular complex assembly. The definitive structural configuration of this linker and its dynamic properties represent a significant, unresolved issue in our understanding of KCNQ1 regulation. As a result, investigating the conformational information of this domain using advanced structural and computational approaches remains a critical research objective. Early computational predictions suggested the four-helix arrangement [39], with follow-up biochemical studies and recent cryo-EM investigations refining our understanding of domain boundaries and tertiary structure [10, 13, 38].

Multifunctional Regulatory Platform

The KCNQ1 C-terminal domain functions as a multifunctional platform that integrates various regulatory modulators responsible for channel activity. A vital interaction occurs with CaM, which acts as an obligate subunit of KCNQ1, remain bound constitutively to IQ motifs within the proximal C-terminal segment [10]. This interaction during early channel biogenesis, is essential for proper folding, assembly, and surface delivery. Besides, the C-terminal domain also presents significant interaction interfaces for KCNE accessory subunits, which strongly modify channel properties. These interactions occur via multiple contact points across the KCNQ1 C-terminal domain [40, 41]. Furthermore, the distal C-terminal domain is key for the KCNQ1 responses to sympathetic stimulation. The HC-HD connecting linker region also serves as an binding site for the A-kinase anchoring protein Yotiao (AKAP9), which coordinates a macromolecular signaling complex [11]. Furthermore, the C-terminal domain is linked to the channel sensitivity to PIP_2, a crucial lipid cofactor for KCNQ1. PIP_2

binding has been found to induce substantial conformational rearrangements that involve the C-terminal domain and its associated CaM, thereby influencing channel activation [14].

Despite considerable advances in our understanding of KCNQ1 structure, a comprehensive dynamic picture of the C-terminal domain has yet to be achieved. The intrinsic flexibility of the linker regions, particularly the functionally critical HC-HD linker, has contributed to these segments being insufficiently resolved in static structural models. In many cryo-EM studies, portions of the C-terminal domain have been omitted during reconstruction to optimize resolution of other core domains, leaving gaps in our structural understanding [7, 10, 13, 14]. For this reason, integrative structural modeling guided by existing cryo-EM density is required to develop structural hypotheses for the HC-HD linker and its role in assembling the Yotiao complex.

The C-terminal domain is a hotspot for disease-causing mutations associated to LQT1 and other cardiac channelopathies [42]. These mutations can compromise assembly and trafficking (e.g., R555C, R594Q), perturb regulatory interactions (e.g., G589D affecting Yotiao binding), or directly affect gating properties [31, 43]. Certain mutations in functionally vital regions, such as R366W near the CaM-binding Helix A and T587M near the tetramerization-involved HD, have been associated with severe arrhythmia outcomes in comparison to other C-terminal domain variants [44]. This difference in pathogenicity indicates the complex structure-function relationships within this domain and the need for detailed mechanistic characterization to develop targeted intervention approaches.

When KCNQ1 forms a complex with KCNE1, it constitutes the ion-conducting pore of the I_{Ks} current [45] which is a principal determinant in the repolarization phase of the ventricular action potential, a process essential for recovery of the electrical resting state of cardiac muscle cell after every heartbeat (as shown in Figure 2, the key phases of depolarization and repolarization). The integrated representation of this critical repolarization process on the surface electrocardiogram is the duration of the QT. Accordingly, dysfunction of the KCNQ1 channel leads to severe clinical consequences. Loss-of-function mutations in the KCNQ1, such as D242N and R243H, can cause LQT1, accounting for 30-35% of all congenital LQTS cases [46]. As displayed in Figure 4, the patho-physiological characteristic of LQT1 is a prolongation of the QT interval on the electrocardiogram. The underlying cause of this clinical observation is a reduction in the outward potassium current due to the impaired I_{Ks} channels, which directly leads to delayed ventricular repolarization.

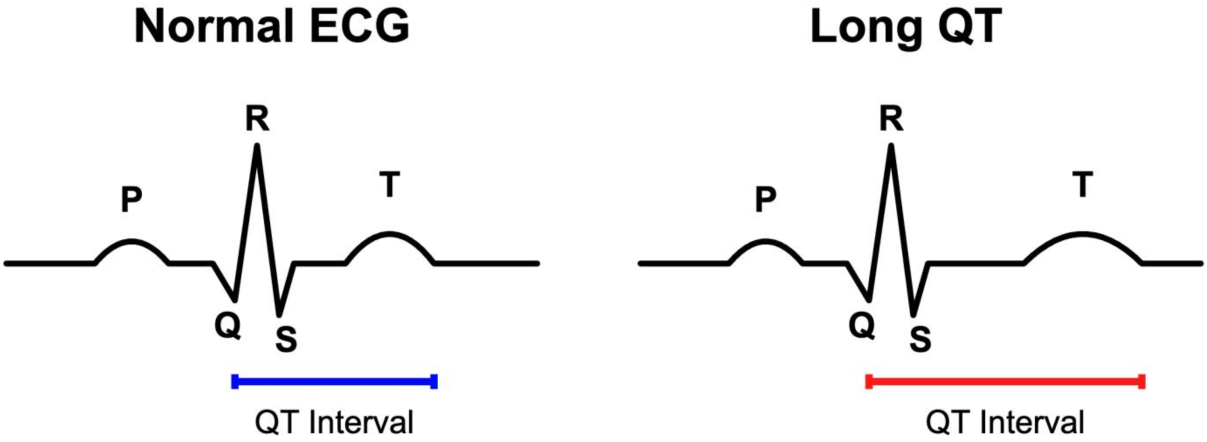

Figure 4. Comparison of Normal and Long QT Syndrome Electrocardiogram Patterns. The normal electrocardiogram shows a standard QT interval, while the Long QT pattern exhibits prolongation, increasing arrhythmia risk. Key waves (P, Q, R, S, T) are labeled for clarity.

Extended action potential duration raises likelihood to rapid ventricular rhythm disorders, causing syncopal events, seizures, or sudden cardiac death. In LQT1, these events are traditionally triggered by adrenergic stress, such as exercise or emotional distress, that overwhelms the compromised repolarization capacity and leads to electrical instability. This risk arises because beta-adrenergic stimulation normally enhances I_{Ks} via phosphorylation pathways, but mutations impair this adaptive response, reducing the channel ability to shorten action potentials during stress [47].

2.2 Regulatory Network of KCNQ1

2.2.1 Auxiliary KCNE Subunits

KCNQ1-KCNE1 complex

The association of KCNQ1 with KCNE1 in cardiomyocytes transforms channel function to generate the I_{Ks} essential for cardiac action potential repolarization [2, 48]. Subunit KCNE1, like other tissue-specific auxiliary subunits, distinctively modulates KCNQ1 gating, primarily by making the channel conduct current through the activated-open state, effectively suppressing the intermediate-open state [14, 49]. This selective modulation is crucial for the precise timing of cardiac repolarization. Evidence for this includes observations that co-expression of KCNE1 with KCNQ1 mutants that either eliminate the intermediate-open state (e.g., F351A) or disrupt activated-open state **electromechanical (**E-M) coupling (e.g., W248R) can result in significant suppression of ionic current, even with intact channel expression and VSD activation [50, 51]. KCNE1 mediates channel gating further by slowing activation kinetics, eliminating inactivation, right-shifting voltage dependence, and altering ion permeation properties [48].

This bias toward the activated-open state has significant physiological implications, particularly for cardiac repolarization timing and its disruption in arrhythmogenic disorders. Although direct structural data for KCNQ1-KCNE1 complexes remain limited, insights derived from KCNE3 interaction studies suggest KCNE1 likely occupies a binding cleft formed by three KCNQ1 subunits: S6 from one subunit, S5 and pore helix from a second, and S1 and S4 from a third subunit [13]. This strategic position would explain capacity of KCNE1 to influence both voltage sensing and pore gating simultaneously. The clinical significance of its regulatory role is evident in LQT1, where mutations that disrupt the activated-open state can severely compromise I_{Ks} function [6]. Consequently, therapeutic strategies aimed at enhancing the activated-open state represent a promising approach for treating KCNQ1-related cardiac arrhythmias.

KCNQ1-KCNE3 complex

KCNQ1 functions in both excitable cell types like cardiomyocytes and non-excitable cells such as epithelial cells of the gastrointestinal tract. The wide-ranging biophysical and functional properties of KCNQ1 largely stem from its association with the KCNE family of single transmembrane domain accessory proteins, notably KCNE3. KCNE3, alternatively named MiRP2 (MinK-related peptide 2), was first identified as a novel β-subunit using homology screening with KCNE1. This polypeptide of 103 residues with a molecular mass of approximately 12 kDa has about 35% sequence identity with other KCNE proteins across their transmembrane domains [52]. Structural investigations demonstrate that KCNE3 comprises an extracellular N-terminal surface-associated amphipathic helix (residues 10-30), a dynamic loop segment, an α-helical transmembrane domain (residues 57-82), a short helix near the membrane interface (residues 90-95), and a disordered C-terminus segment (residues 96-103) [13]. Notably, the transmembrane domain exhibits is mildly curved, with a bend near the C-terminal region, while residues Thr71, Ser74, and Gly78 are positioned along the concave face of this curved structure [53].

The interaction of KCNE3 with KCNQ1 modify the biophysical properties of the channel complex. While KCNQ1 alone acts as a voltage-dependent potassium channel, the KCNQ1-KCNE3 complex exhibits very fast activation kinetics with a approximately linear current-voltage relationship even at negative membrane potentials as well [52]. This mechanism is different from the KCNQ1-KCNE1 complex (I_{Ks}), which displays slow activation kinetics and strong voltage dependence. The mechanism underlying this difference involves KCNE3-mediated modification of the VSD of KCNQ1 [54]. Studies have demonstrated that KCNE3 facilitate the voltage dependence of the S4 segment movement to rather hyperpolarized potentials, effectively rendering the channel constitutively conductive in the physiological voltage range [54]. This effect is directly opposite to that of KCNE1, which stabilizes the S4 segment in the resting state and slows its transition to the active state.

Early structure-function work employing chimeric constructs of KCNE1 and KCNE3 have uncovered a three-amino-acid stretch within the transmembrane segment that is both required and sufficient to define the specificity of activation kinetics control by these two β-subunits [6]. Remarkably, the contrasting gating characteristics of KCNE1 and KCNE3 can be converted by a single point variant: T58V in KCNE1 or V72T in KCNE3 [55]. Recent progress in structural biology have shed light on the mechanism by which KCNE3 modulates KCNQ1 function, in which KCNE3 binds in the cleft at the PD and VSD interface of KCNQ1 [13]. This location supports direct modulation of KCNE3 to both VSD and PD of KCNQ1. High-resolution cryo-EM structures of the KCNQ1-KCNE3 complex in 4:4 stoichiometry provide direct structural support, demonstrating that KCNE3 holds S4 in the activated, upward conformation [13]. At the molecular level, electrostatic interactions play a crucial role in KCNE3-mediated modulation of KCNQ1. Two negatively charged residues in KCNE3 (D54 and D55) are vital for its effect on KCNQ1 channels, largely through electrostatic interaction with R228 in the S4 of KCNQ1. This interaction appears to stabilize S4 in its activated "up" state, an obligate step for channel opening.

The KCNQ1-KCNE3 complex performs key roles in epithelial tissues, particularly in the intestine, stomach, kidney, and respiratory airways. In these tissues, the complex enables potassium ion recycling processes, which is required for transepithelial chloride ion secretion [53]. The persistently open state of KCNQ1-KCNE3 channels makes them effective regulators of fluid and electrolyte balance in non-excitable tissues. KCNQ1-KCNE3 currents can be augmented by increasing intracellular cAMP levels [52], providing a mechanism for hormonal regulation of channel activity.

Impaired function of the KCNQ1-KCNE3 complex has been implicated in various disorders. KCNE3 has been linked to salt and fluid homeostasis disorders, including cystic fibrosis [53].

Moreover, mutations in KCNE3 have been found to cause cardiac arrhythmias and inner ear disorders such as Meniere disease and tinnitus [56, 57]. Since KCNQ1-KCNE3 channels play a crucial role in the secretion of water and salt in the colon, they represent a promising target for drugs aimed at treating secretory diarrhea [4].

A particularly interesting aspect of KCNQ1-KCNE3 regulation involves estrogen. Study has found that estrogen treatment disrupts the KCNE3-KCNQ1 channel complex, which appears to involve KCNE3 Ser82, possibly through a phosphorylation-dependent mechanism [58]. This finding may contribute to understanding the observed sex difference in cystic fibrosis survival, where females generally experience higher mortality rates with shorter lifespans compared to males. Ongoing research into this KCNQ1-KCNE3 complex continues explore its roles in health and disease, potentially leading to emerging therapeutic strategies for various conditions, such as cystic fibrosis and secretory diarrhea.

2.2.2 PIP$_2$ Regulation of Voltage Sensor-Pore Coupling

Unlike small-molecule activators like ML277, lipid cofactors such as PIP$_2$ provide physiologically relevant endogenous regulation of KCNQ1, connecting voltage sensing to pore dynamics in a voltage-dependent manner. PIP$_2$ functions as an essential cofactor in KCNQ1 channel activation [8, 33], bridging voltage sensing to pore opening. Without PIP$_2$, KCNQ1 adopts a decoupling conformation with mobile voltage sensors but a largely closed pore, highlighting its essential role in E-M coupling. As shown in Figure 5, chemical structure of PIP$_2$ features a polar headgroup (inositol) and hydrophobic fatty-acid chains, enabling its membrane-embedded interactions with the channel.

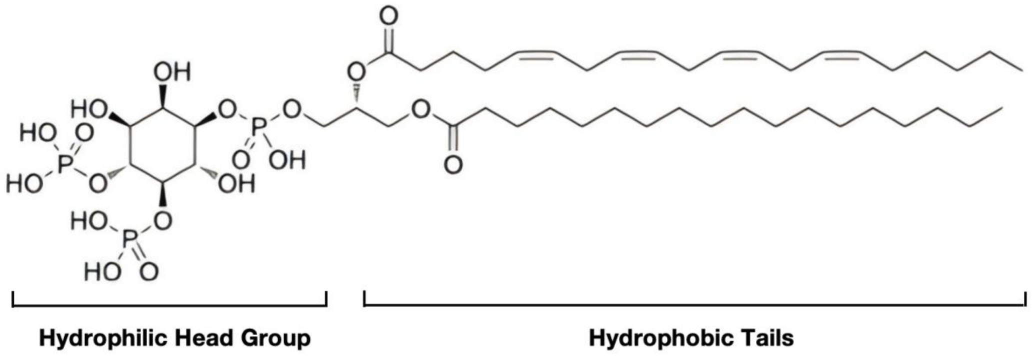

Figure 5. Chemical structure of phosphatidylinositol 4,5-bisphosphate (PIP$_2$). The hydrophilic head group and hydrophobic tails are highlighted, illustrating its role in membrane interactions and channel modulation.

Structural studies have identified the PIP_2 binding pocket to the coupling interface between the VSD and pore, where it forms interactions with numerous positions involving positively charged residues from the S0 helix, S2-S3 loop, and S4-S5 linker [13, 14]. The high-resolution cryo-EM data indicates that the 1,4,5-trisphosphated inositol headgroup of PIP_2 establishes well-defined interactions in this pocket, whereas its fatty acid chains display higher conformational flexibility.

PIP_2 binding induces extensive conformational rearrangements that propagate across the channel complex. The S6 and HA helices have been found to transition from a helix-loop-helix conformation to a continuous extended helix, while the C-terminal portion of S6 adopts a key bend at the conserved PAG motif [13]. These coordinated structural rearrangements are in line with a dilation the cytoplasmic pore entrance from approximately 1 Å to greater than 3.5 Å near Ser349, resulting in gate opening. Recent studies have revealed that VSD position directly regulates PIP_2 binding via a steric mechanism [7]. Under the hyperpolarized (down) state, S4 physically occludes the PIP_2 binding site, preventing PIP_2 interaction and maintaining channel closure. Thus, the voltage sensor acts predominantly as a gatekeeper for PIP_2 binding, with its influence on the channel gate being through a sequential cascade: voltage sensor movement → altered PIP_2 ligand affinity → altered pore opening [7]. This finding supports a updated gating paradigm for KCNQ1, establishing a regulatory sequence where voltage primarily controls PIP_2 accessibility rather than directly actuating the pore gate. Most recently, high-resolution structural and functional analysis by Cui et al. (2025) reports a two-binding-site model for PIP_2 regulation in KCNQ1 complexes [47]. In addition to the well-characterized PIP_2 site near the voltage sensor (Site 1), a second PIP_2-binding site (Site 2) located at the VSD-pore junction, mainly composed of the S4-S5 linker, S5, and the S6-HA region. Occupancy of Site 2 is associated with stabilization of the activated, straightened cytosolic helical conformation that accompanies pore dilation and the bent-to-straight transition. Importantly, KCNE1 and KCNE3 contribute differently to this Site 2 environment, leading to distinct apparent PIP_2 sensitivities of the channel complexes [47]. As shown in Figure 6, this gating model illustrates how VSD movement enables PIP_2 access, highlighting the indirect coupling mechanism. Clinically, PIP_2 dysregulation contributes to LQT1 phenotypes, as mutations near binding sites impair coupling. Therapeutic strategies targeting PIP_2 analogs could enhance channel function in deficient states, complementing activators like ML277.

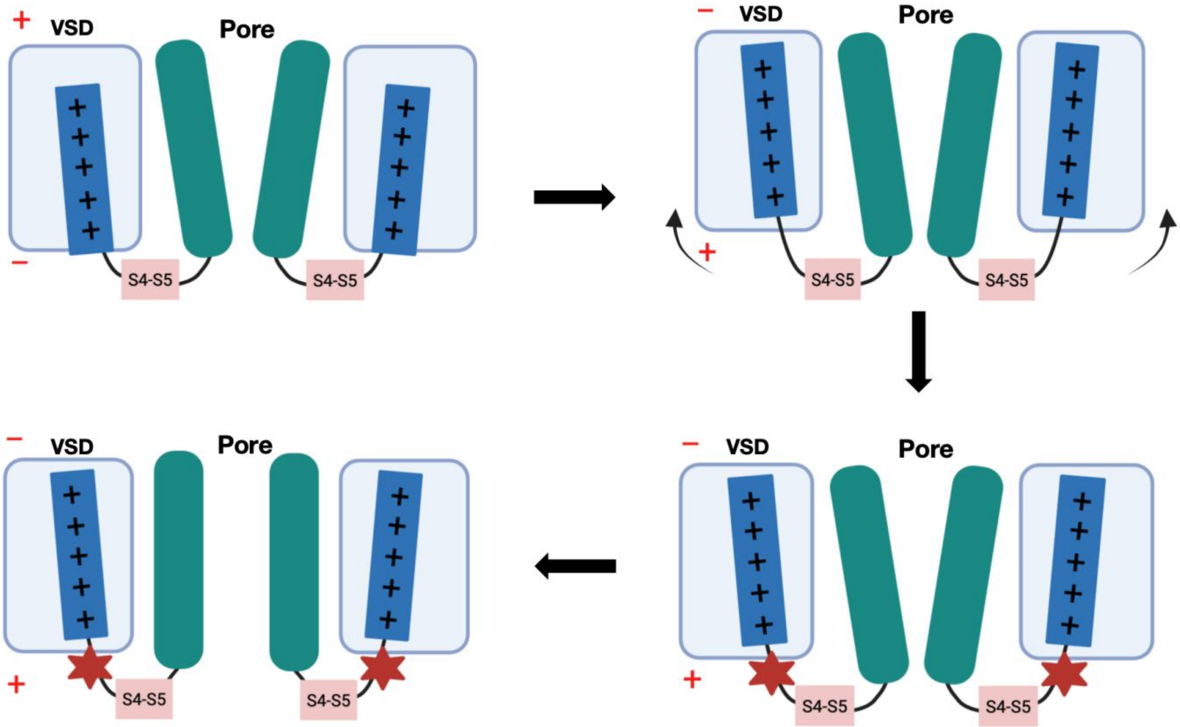

Figure 6. Model of KCNQ1 gating mechanism. The pore domain is colored dark green, the voltage sensor is gray, the S4 helix is blue, the S4-S5 linker is pink, and PIP_2 is displayed with red five-pointed star. The voltage sensor regulates the binding of PIP_2 by occluding the binding site in the down conformation. When membrane depolarization occurs, the voltage sensor moves to the up conformation, which then allows PIP_2 to bind to the channel and open the pore.

2.2.3 Calmodulin-Mediated Regulation of Channel Activation

Calmodulin (CaM) serves as both a structural component and functional regulator of KCNQ1 channels. It acts as an obligate subunit of KCNQ1, contributing to channel assembly and surface localization. The KCNQ1-CaM interaction involves two distinct modes revealed through structural studies. The primary contact incorporates the HA-HB helices of KCNQ1 into a pocket formed by N- and C-lobes of CaM [59]. More significantly, a second interface, which is specific to KCNQ family channels, forms between third EF of CaM hand and the conserved nine-amino-acid S2-S3 loop of the voltage sensor [10]. This latter interaction provides a molecular basis for channel-specific regulatory functions of CaM and establishes a potential secondary pathway for coupling voltage sensing to pore gating.

CaM also functions as a regulator of channel gating, alleviating inactivation in a Ca^{2+}-dependent fashion [60]. By interacting with both the voltage sensors and the HA-HB helices, CaM could provide a noncanonical coupling pathway between voltage sensors and the pore of KCNQ1, apart from the S4-S5 linker. The discovery that PIP_2 binding causes ~180° rotation of CaM while releasing its interaction with the voltage sensor demonstrates the integrated nature of KCNQ1 regulation [13]. This substantial conformational rearrangement suggests that CaM actively participates in the channel opening mechanism rather than serving merely as a passive structural element. The physiological significance of CaM modulation is revealed by the identification of CaM mutations associated with cardiac arrhythmias. The CaM-N98S mutation, linked to prolonged QT intervals and sudden infant death, disrupts the interface between EF3 hand of CaM and the KCNQ1 S2-S3 loop, shifting voltage-dependent activation [61]. This provides direct evidence that perturbations in CaM-KCNQ1 interactions can precipitate clinically relevant channel dysfunction.

2.2.4 Yotiao Scaffolding and Phosphorylation in the I_{Ks} Complex

While lipid cofactors like PIP_2 establish baseline electromechanical (E-M) coupling in KCNQ1, scaffolding proteins such as Yotiao drive dynamic post-translational modifications (PTMs) that enable prompt responses to physiological stimuli including β-adrenergic signaling. The activity of KCNQ1 is regulated by PTMs, noticeably including phosphorylation. Specificity within these signaling pathways is frequently driven by spatial compartmentalization, a mechanism whereby enzymes and their substrates are co-localized by scaffolding proteins. Yotiao, the AKAP9-encoded A-kinase anchoring protein, is regarded as a core component of this regulatory mechanism for KCNQ1 [12, 18, 62].

Yotiao serves as an essential scaffolding protein through its direct physical interaction with the KCNQ1 channel subunit. The C-terminus of KCNQ1 contains a specific Yotiao-binding site [19]. This direct association is required for the subsequent recruitment of protein kinase A (PKA) to the KCNQ1 channel complex. By tethering PKA in immediate proximity to KCNQ1, Yotiao enhances the efficient phosphorylation of the channel. Specifically, Yotiao is responsible for coordinating the PKA-dependent phosphorylation of KCNQ1 at Ser27 and Ser92 [11, 45]. This spatially constrained signaling architecture ensures that KCNQ1 can be rapidly and selectively modulated in response to upstream signals, such as those initiated by β-adrenergic receptor activation [63].

The main functional consequence of Yotiao-anchored PKA phosphorylation of KCNQ1 is an augmentation of I_{Ks} channel activity [64]. The resultant increase in outward potassium current that shortens the cardiac action potential duration, an adaptive response that is critical during sympathetic stimulation to accommodate increased heart rates. Therefore, the interaction with Yotiao is fundamental for the canonical β-adrenergic receptor-mediated regulation of I_{Ks} in the heart. In addition to PKA, Yotiao also tethers protein phosphatase 1 (PP1) to the KCNQ1 channel complex. The integration of both a kinase (PKA) and a phosphatase (PP1) into a single macromolecular unit provides a mechanism for the precise and reversible control of phosphorylation status of KCNQ1 [65]. Figure 7 exhibits this complex, highlighting the scaffolding role of Yotiao in localized signaling with the I_{Ks} complex **(**KCNE1/KCNE3) and key phosphorylation sites (e.g., S27, S92).

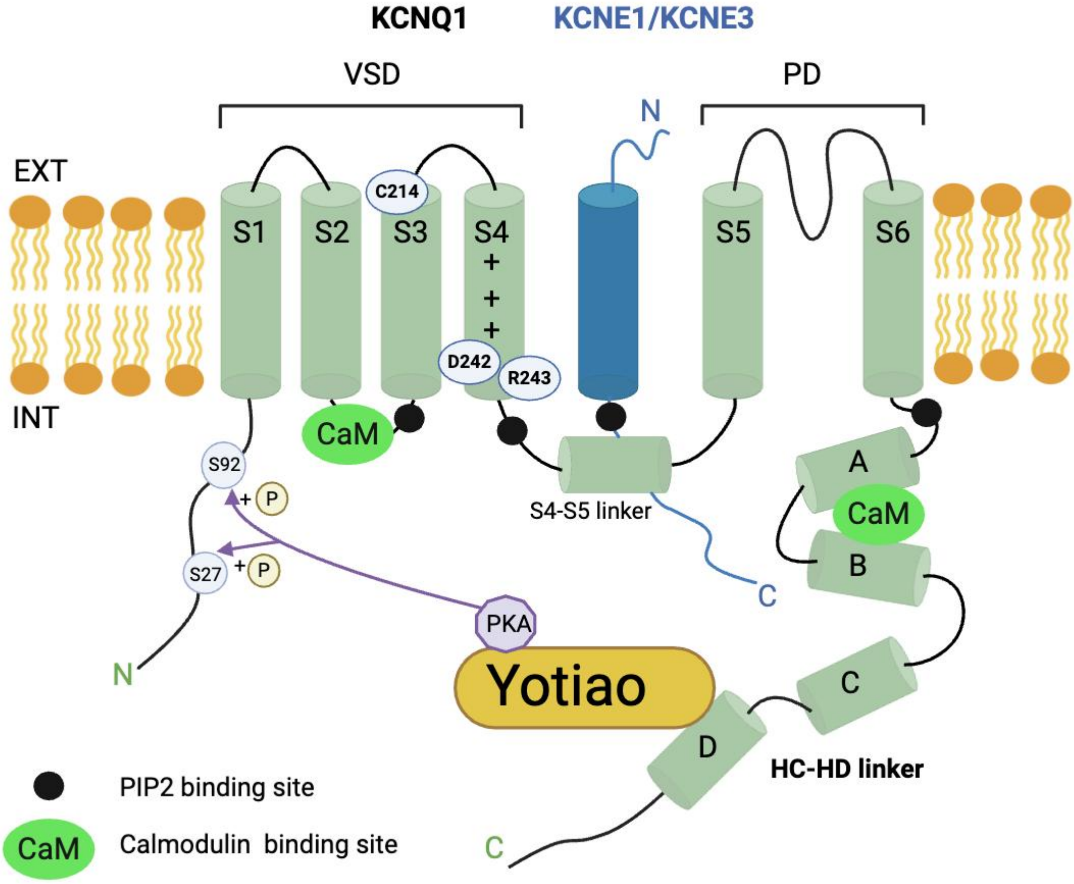

Figure 7. Schematic diagram of KCNQ1-KCNE1/KCNE3 complex and Yotiao-dependent phosphorylation. Key components including PKA, PP1, AC9, and phosphorylation sites (e.g., S27, S92) are shown, emphasizing the scaffolding role in localized signaling.

Such regulation is essential for adjusting both the strength and the operational timing of the I_{Ks} current. A localized signaling nanodomain formed by the KCNQ1-Yotiao complex is further demonstrated by the recruitment of adenylyl cyclase type 9 (AC9). AC9 has been shown to be closely associated with both Yotiao and the I_{Ks} ion channel within the cardiac tissue [12]. This complex, consisting of KCNQ1, Yotiao, PKA, and AC9, facilitates drives local cAMP production that specifically aim at the regulation of the I_{Ks} channel. Study using AC9 knockout mice method has shown that while the global adenylyl cyclase activity in cardiac tissue remained largely unaffected (less than 3% reduction), the specific pool of adenylyl cyclase activity tethered to Yotiao was completely lost [64]. This selective effect strongly reveals that AC9 is the dominant cAMP producer within this compartmentalized signaling environment, which is essential for localizing PKA activation and subsequent KCNQ1 phosphorylation, and for effectively coupling these modifications to upstream receptor pathways.

The KCNQ1-Yotiao signaling activity is influenced by physiological stimuli, such as exercise training. Wang et al. reported that in rats subjected to a 6-8 week period of voluntary exercise(wheel running), there was a substantial reduction in the protein expression levels of Yotiao within ventricular myocytes [66]. This exercise-induced reduction in Yotiao protein content was occurring alongside decreases in the protein levels of both KCNQ1 and KCNE1 subunits [66]. The lower levels of Yotiao are expected to lead to reduced PKA-mediated phosphorylation of KCNQ1, thereby compromising the I_{Ks} response to sympathetic stimulation. These alterations, inclusive of the reduction in Yotiao, contribute to the prolonged action potential duration at baseline observed in trained animals, a change that potentially enhance myocyte efficiency [66]. The structural and functional integrity of the KCNQ1-Yotiao interaction is of considerable importance for the maintenance of normal cardiac rhythm. Disruption of this interaction, or the presence of mutations in KCNQ1 that impair its PKA-mediated phosphorylation, can lead to the development of long QT syndrome [11].

A thorough understanding of the KCNQ1-Yotiao signaling pathways is therefore necessary, not only for elucidating fundamental principles of cardiac physiology but also for advancing our knowledge of the mechanisms underlying cardiac arrhythmias and for the development of next-generation, targeted therapeutic interventions.

2.2.5 Intrinsic Activator: ML277

ML277 is a small-molecule activator with exceptional specificity, potency (EC_{50} = 260 nM), and therapeutic potential for treating cardiac arrhythmias [23], primarily by strengthening the activated-open state E-M coupling [22]. Unlike various other potassium channel activators, ML277 selectively augments KCNQ1 function without affecting other cardiac ion channels or neuronal KCNQ isoforms, making it an ideal candidate for treating LQT1 with minimal off-target effects. This specificity for the activated-open state provides a valuable pharmacological tool; variant such as W248R, S338F abolish the ML277 potentiation [49]. Further docking studies reveal that ML277 binds at the S4-S5L/pore interface, engaging residues crucial for activated-open state E-M coupling [49]. Recent high-resolution structural studies have revealed that binding site of ML277 at the critical "elbow" interface formed by the S4-S5 linker, S5, and neighboring S5' and S6' helices [14]. As illustrated in Figure 8, the chemical structure of ML277 features a sulfonamide core with aromatic substituents that facilitate interactions at this interface, enabling targeted modulation of gating without widely perturbation of other channel components.

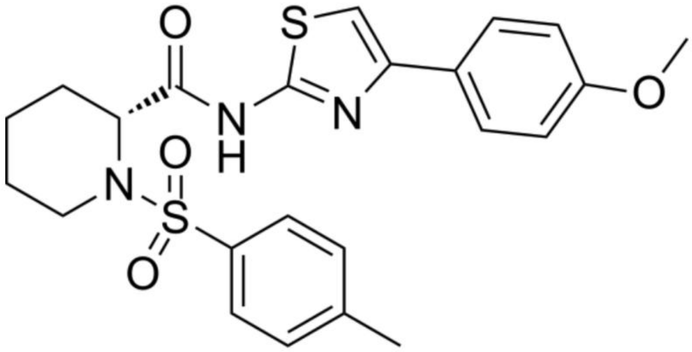

Figure 8. Chemical structure of ML277.

Additionally, the location of ML277 directly affects the activation gate of channel without perturbing the C-terminal domain, which may help explain the targeted effect of ML277 on gating mechanics. Functional analyses demonstrate that ML277 specifically potentiates the activated-open state current while preserving intermediate-open state kinetics, significantly extending both activation (563 to 952 ms) and deactivation (103 to 207 ms) time constants of the activated-open component [14]. This selective stabilization of the activated-open state explains the notably effect of ML277 on voltage dependence, making a subtle right-shift in the G-V relation rather than the left-shift typically observed with channel activators. The action mechanism of ML277 represents an advance in ion channel pharmacology by demonstrating that selective enhancement of specific gating transitions offers a more precise approach to therapeutic modulation than conventional pore blockers or non-specific activators.

2.2.6 Complex-Dependent Dual Modulation by Mallotoxin

Mallotoxin (MTX, also widely known as rottlerin), a polyphenol-rich natural compound from *Mallotus* species, has a long history in traditional medicine for treating conditions like seizures [67]. Originally sourced from "kamala" of *Mallotus philippinensis* and *Mallotus oppositifolius*. Its historical therapeutic use has driven comprehensive pharmacological studies, revealing its significant activity as a modulator of various ion channels [17, 67-69]. As shown in Figure 9, the chemical structure of MTX illustrates its polyphenolic structure characterized by multiple hydroxyl groups**.**

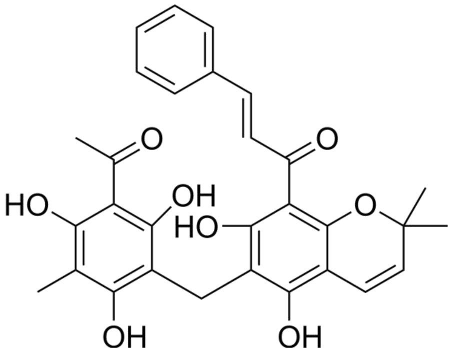

Figure 9. Chemical structure of mallotoxin (MTX).

The main focus of MTX research has been its complex interactions with KCNQ potassium channels. Notably, it exhibits a subunit-dependent dual effect on KCNQ1 channels. MTX enhances KCNQ1-KCNE1 complexes (EC_{50} ~ 4.9 μM) [16], an action linked to a proposed S4 binding site and influenced by the chemical structure of MTX [16, 17, 70]. Conversely, co-assembly with KCNE3 makes KCNQ1 sensitive to inhibition by MTX, highlighting the vital role of auxiliary subunits in its modulatory effects [17]. Aside from KCNQ1, MTX also potently activates neuronal KCNQ2/3 channels (EC_{50} ~11.5 μM at -60 mV), where it demonstrates synergistic anticonvulsant effects when combined with isovaleric acid and retigabine [67]. The activating characteristics of MTX can extend to KCNQ4 and KCNQ5 channels as well [16, 67]. Moreover, it also strongly stimulates BK channels, which are large-conductance potassium channels responsive to both calcium and voltage. This stimulation leads to a significant negative shift in their voltage-dependent activation [71]. However, the presence of auxiliary γ subunits markedly reduces this modulatory effect [68]. While mainly recognized for its ion channel activities, MTX also demonstrates other significant biological effects.

For instance, MTX is recognized for its capacity to strongly promote autophagy, which aids in clearing pathogenic tau within neuronal cells, a process linked to AMPK activation and mTORC1 inhibition [72].

The therapeutic prospect of MTX is mainly attributable to its ion channel modulatory capacity. Its activation of KCNQ2/3 channels, especially the cooperative effects, presents promising strategy for epilepsy treatment. The activation of KCNQ1-KCNE1 complex suggests potential in cardiac repolarization disorders like congenital LQTS, while BK channel activation could be beneficial for conditions involving neuronal or smooth muscle hyperexcitability [71]. The induction of the autophagic pathway further broadens its potential application to neurodegenerative diseases like Alzheimer [72].

2.3 KCNQ1 Dysfunction: From Pathogenic Mutations to Oxidative Stress

This section examines how disruptions, such as pathogenic mutations and oxidative stress, lead to KCNQ1 dysfunction, beginning with mutations that impair channel gating and coupling, setting the stage for environmental factors like ROS.

2.3.1 Pathogenic Mutations in KCNQ1: D242N and R243H

Physiologically, the duration of the human cardiac action potential typically ranges from 250 to 350 ms, a critical interval primarily determined by the I_{Ks} current. Recent studies revealed that patients with loss-of-function mutations in the KCNQ1 gene that reduce the I_{Ks} can develop inherited channelopathies, such as LQTS, which is a heart disorder condition characterized by a prolonged Q-T time interval that can be identified on the electrocardiogram [73, 74]. The delayed repolarization raises the risk of sudden cardiac death mostly caused by exercise or leading to ventricular arrhythmia [75]. Mutations in KCNQ1 causing LQTS are regarded as LQT1 and those in KCNE1 as LQTS5. Mutations in KCNQ1 are the most common cause of LQTS, accounting for approximately 30-35% of all congenital cases. More than 300 mutations in KCNQ1 pertinent to LQTS have been mapped. The KCNQ1 channel has been regarded as potential target therapeutics for LQTS. Moreover, pathological data shows that patients with LQTS have a higher risk of diabetes due to the activity of KCNQ1 in insulin secretion, which are in consistent with the numerous genome-wide association (GWAS) investigations identifying KCNQ1 as a susceptibility locus for type 2 of diabetes [76-78].

While KCNQ1 forms the cardiac I_{Ks} with KCNE1, its interaction with KCNE3 defines a distinct channel complex. The KCNQ1-KCNE3 channel is primarily expressed in non-excitable cells, including epithelial cells of the stomach [5], small intestine [52], colon [79], kidney [80] and airways [81], facilitating water transport, intestinal sodium absorption, gastric acid and intestinal cAMP-dependent chloride secretion. The cryo-EM structure of KCNQ1-KCNE3 in a ratio of 4:4 stoichiometry was recently identified, serving as structural basis for our study [13]. The mechanisms by which KCNE protein mediate KCNQ1 gating behavior has long been a key question in ion channel studies. KCNQ1-KCNE3 channels are largely voltage-independent with a nearly linear relationship with membrane potentials under physiological conditions and insensitive to pH [54, 82]. Additionally, KCNE3 was identified as playing a vital role in maintaining KCNQ1 channel in a constitutively open by stabilizing the S4 of VSD in KCNQ1 [52], which is also supported by a recent cryo-EM structure of the KCNQ1-KCNE3-CaM complex that KCNE3 directly interacts with the bottom of S4 [13]. Importantly, residues D242 and R243 within the KCNQ1 S4 voltage-sensing segment are key determinants of the interaction with the KCNE3 subunit. Structurally, residues D242 and R243 are located at the critical interface with KCNE3 [13], suggesting their functional importance for complex assembly. Additionally, cryo-EM structural analysis reveals a direct main-chain interaction between KCNQ1-R243 and KCNE3, suggesting a structural role for R243 in stabilizing the S4 conformation required for functional modulation by KCNE3 [83].

The KCNQ1 channel activity is not only modulated by membrane potential difference but also by PIP_2 molecules, a significant phospholipid component of cell membranes [8, 84, 85]. Specifically, when the cell membrane depolarizes, the positively charged S4 segment of KCNQ1 moves outward in response to the change of membrane's electric field, triggering the exposure of binding site for PIP_2. Afterwards, PIP_2 binding to this site stimulates VSD-PD coupling, leading to the pore opening [7]. Thus, the KCNQ1-KCNE3 channel in complex with PIP_2 represents a promising therapeutic target for treating life-threatening disorders like colonic secretory diarrhea.

KCNQ1 activity is modulated not only by voltage but also by PIP_2, which bridges VSD movement to PD opening upon depolarization. Mutations disrupting this interface, such as those in S4, can impair PIP_2 binding and VSD-PD coupling, causing dysfunction in both cardiac and epithelial contexts. Considering that D242 and R243 are located in the S4 segment, close to both the KCNE3 interacting surface and the PIP_2 binding site, mutations at these positions can have significant consequences. The D242N mutation has been determined to be associated with LQTS [20], a serious cardiac condition characterized by abnormal heart rhythms and an increased risk of sudden cardiac death. Experimental data have demonstrated that the D242N mutation impairs the VSD-PD coupling when the channel is in the activated open state [86]. Similarly, the R243H mutation has been found to be associated with deafness and LQT [87]. Studies have revealed that the binding affinity for PIP_2 is reduced in KCNQ1 with R243H mutation [21].

The introduction of new residues by these mutations (Asp -> Asn; Arg -> His), which possess different charge and size characteristics, can potentially impact the conformation of the protein and thus influence its function at this critical regulatory interface. Therefore, we used MD simulations to explore the structural and dynamic effects of the D242N and R243H mutations on the cryo-EM structure of the KCNQ1-KCNE3-PIP_2 complex. This structure and the specific location of D242 and R243 are highlighted in Figure 10, illustrating their proximity to key regulatory interfaces.

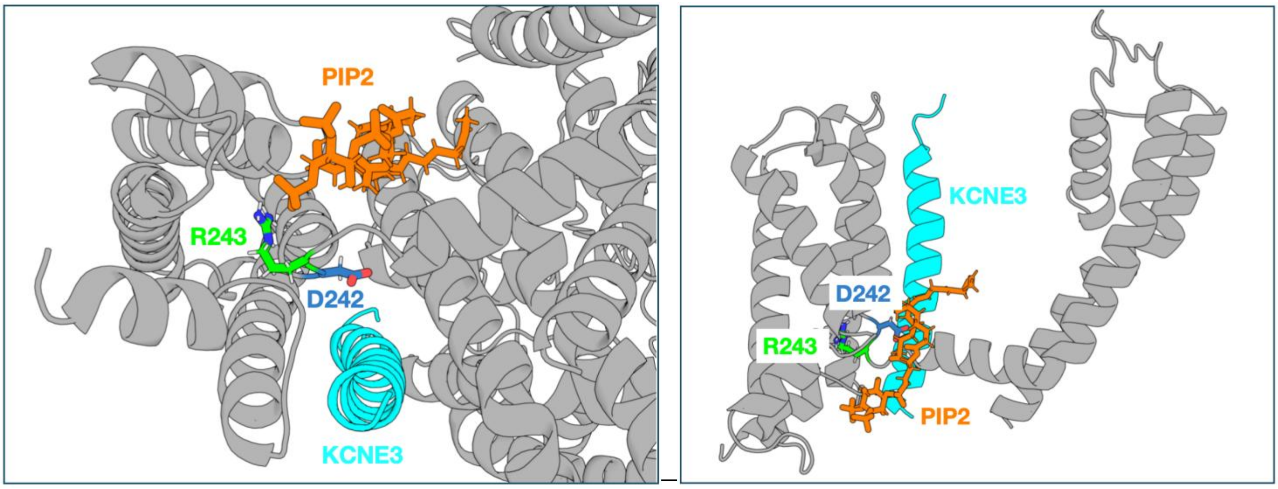

Figure 10. Structural models of the KCNQ1-KCNE3-PIP_2 interface. (A) A cytoplasmic view of the tetrameric KCNQ1 channel complex. (B) For clarity, a side view of a single KCNQ1 subunit is shown. Both views illustrate the close spatial arrangement of D242 (blue) and R243 (green) on the S4 helix relative to the KCNE3 subunit (cyan) and PIP_2 (orange). Structural representation of the D242 and R243 residues in the KCNQ1 channel.

2.3.2 Oxidative Modification of KCNQ Channels

The Kv7 (KCNQ) family of voltage-gated potassium channels is essential in controlling membrane excitability across multiple tissue types. A vital and increasingly recognized mode of regulation for these channels is oxidative reggulation by ROS, which can impact their function and contribute to both physiological redox signaling and pathological contexts.

Oxidative Stress

Oxidative stress arises from exposure to ROS overproduction, which belong to a subset of free radicals and related molecules, may alter the intracellular redox state. Free radicals are characterized by one or more unpaired electrons that display a marked tendency for electron transfer through electron-transfer processes. These species exhibit strong chemical reactivity, with lifetime on the microsecond scale typically less than 10^{-6} seconds in biological systems. The most of major physiological relevance ROS include superoxide ($[O^{2-}]$), hydrogen peroxide ($[H_2O_2]$), and hydroxyl radicals ($[\bullet OH]$) [88]. The generation of superoxide, initiated through single-electron reduction of molecular oxygen, is facilitated by various cellular constituents, including thiol complexes, glucose, and nucleotides, particularly in the presence of transition metals such as copper or iron [89].

In cellular systems, the principal endogenous sources of ROS are mitochondria during aerobic respiration, where respiratory chain leak forms$[O_2\bullet^-]$. ROS have both signaling and damaging roles. When present at low levels, they act as signaling molecules modulating processes like proliferation, differentiation, and apoptosis. However, aberrant increase, commonly driven by external stress factors, inflammation, or impaired mitochondrial function, causes biomolecular injury, including lipids, proteins, and DNA. Key exogenous factors, including ionizing radiation exposure, atmospheric contaminants, heavy metal exposure, and organic solvents like benzene, primarily contribute to intracellular ROS burden. The consequences of oxidative modifications of cellular macromolecules, including lipids, proteins, and nucleic acid, can lead to extensive cellular dysfunction (as shown in Figure 11).

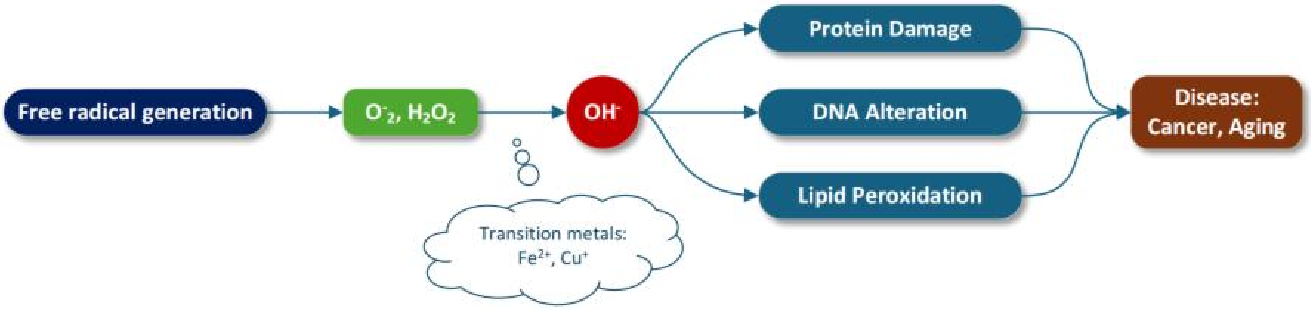

Figure 11. Free radicals and their damaging consequences. Protein damage, free radical generation (O_2, H_2O_2, $\bullet OH$), DNA alteration (leading to diseases like cancer and aging), lipid peroxidation, and the role of transition metals (Fe^{2+}, Cu^+).

As a relatively broad class within ROS, hydrogen peroxide is not a radical in the strict sense, but its ability to pass through cellular membranes readily enabling long-range diffusion prior to decomposion generating strongly reactive hydroxyl radicals, thus acting as a vital mediator of both oxidative damage intercellular and intracellular levels.

The relationship between oxidative stress and the disease development is two-way association where oxidative stress can act as both a driving force and a result of disease-associated processes in various states, such as cancers, degenerative neurological disorders, and metabolic syndromes. One of the main challenges in exploring oxidative stress is the establishment of reliable biomarkers, since directly assessment of ROS level is challenging due to their instability. Therefore, research typically focuses more on relatively stable secondary oxidation products and their breakdown products as indirect indicators.

Biological systems have developed sophisticated antioxidant defense systems including both enzyme-based and non-enzymatic compounds. The enzymatic system includes superoxide dismutation enzyme, which accelerates the conversion of superoxide into peroxide, while catalase together with glutathione peroxidase subsequently enables the decomposition of hydrogen peroxide to water and molecular oxygen [90]. This frontline antioxidant defense is additionally reinforced by peroxiredoxin family proteins and glutathione reductase, which involve in hydrogen peroxide removal. The non-enzymatic component include plasma proteins such as albumin, ferritin, and ceruloplasmin, function via chelation of transition metals. Additionally, metallothioneins enhance protective protection through their plentiful thiol groups.

Antioxidants from the diet serve as important supplements to endogenous defense systems, including carotenoids, vitamins C and E and polyphenolic compounds [91]. Particularly, flavonoid ,subclass of polyphenols abundant in fruits, vegetables, and medicinal plants, exhibit particular antioxidant properties through multiple mechanisms: direct ROS scavenging activity, inhibition of oxidative enzymes, modulation of redox-dependent transcriptional factors (notably Nuclear factor erythroid 2-related factor 2), enhancement of endogenous antioxidant expression, and stabilization of cellular structures. By increasing endogenous antioxidant level and maintaining the structural integrity of cellular components, flavonoids display comprehensive potential in protection against oxidative stress, with emerging relevance for KCNQ modulation in oxidative pathologies.

The interaction between endogenous and exogenous antioxidant systems is crucial in maintenance of cellular redox homeostasis, representing a critical mechanism for preventing oxidative stress-induced pathologies.

Oxidative Regulation of Neuronal KCNQ2-KCNQ5 Channels

In the nervous system, Kv7.2-Kv7.5 channels are key regulators of neuronal electrical excitability, mainly by forming the M-current [29]. Among these, Kv7.2, Kv7.4, and Kv7.5, along with heteromeric Kv7.2/7.3 channels, exhibit strong susceptibility to ROS. Oxidation-mediated modification of these specific Kv7 channels by ROS represents a major mode of regulation influencing cellular adaptability and is associated with a range of physiological and pathological states, including neurodegenerative conditions [92, 93].

The specific structural features of Kv7.2, Kv7.4, and Kv7.5 channels determine their susceptibility to ROS-driven modification. A critical segment for this redox relativity profile is the intracellular S2-S3 linker, which contains a distinctive cluster of three cysteine residues (Cys156, Cys157, and Cys158 in Kv7.2). These evolutionary conserved residues, conserved across Kv7.2, Kv7.4, and Kv7.5, form an oxidation-sensitive pocket [94]. Oxidants preferentially interact with the thiol group of cysteine residues, potentially leading to the generation of reversible protein disulfides. Moreover, this S2-S3 linker is recognized as a site to interact with regulatory proteins, including CaM. Structural evidence has recently suggested plausible interaction between this redox-sensitive linker and the Ca^{2+}-binding loop in CaM [32], supporting linkage between Ca^{2+} and redox signaling in channel modulation.

When exposed to oxidizing agents like hydrogen peroxide (H_2O_2), Kv7.2, Kv7.4, and Kv7.5 channels show distinct functional responses [94]. A prominent effect is a strong activity augmentation: H_2O_2 application leads to a substantial increase in steady-state currents in these channels, including heteromeric Kv7.2/Kv7.3 channels [94].

Interestingly, while Kv7.3 also possesses this crucial triple-cysteine pocket located its S2-S3 linker, its resistance to oxidative modification is largely owing to its exceptionally high basal open probability. Since H_2O_2 excerts its effect by increasing channel open probability, and Kv7.3 channels are already operating close to their maximum capacity under resting conditions, oxidative modification cannot be further upregulated their activity. This functional ceiling, instead of absence of the structural target, explains oxidation insensitivity of Kv7.3 [94].

Additionally, oxidative modification also alters the functional gating properties of these sensitive Kv7 channels, typically causing a leftward shift in their voltage dependence of activation, accelerating activation kinetics, and slowing deactivation [94]. Importantly, these oxidative effects are reversible in a redox-dependent manner. Applying a reducing agent such as dithiothreitol can completely reverse the H_2O_2-induced changes [94]. This reversibility indicates that reductant systems within cells, such as those involving glutathione or thioredoxin, likely play a role in dynamically regulating channel function in a living cell [95-97].

The way ROS modulate these Kv7 channels is not merely a simple chemical modification. It involves complex regulatory mechanisms, involving interactions with CaM. The EF hand of CaM, particularly the EF3 hand, has been recognized as essential player. For instance, preventing Ca^{2+} binding specifically to the EF3 hand eliminates the oxidation-induced enhancement of Kv7.4 currents [98]. Additionally, oxidation of the cysteine residues in the S2-S3 loop of these Kv7 channels leads to a persistent inhibition mediated by the EF3 hand of CaM, a process required for this signaling pathway [98].

The oxidative modification of Kv7.2-Kv7.5 channels has significant functional consequences on cell physiology, especially in neuronal cells. KCNQ1 could be similarly redox-regulated, considering the conserved cysteine residues across the KCNQ family. The enhancement of M-current (mediated by these Kv7 channels) due to oxidation leads to hyperpolarization of the membrane potential and a substantial decrease in action potential firing frequency in neurons like rat sympathetic neurons [94]. This implies a new regulatory mechanism for M-channel regulation that could contribute to protective reduction of neuronal excitability during conditions of oxidative stress. Indeed, the generation of ROS and subsequent oxidative modification and augmentation of M-currents in neurons are thought to protect neurons against oxidative stress-related degeneration.

Oxidative Regulation of Cardiac KCNQ1 Channel

Oxidative stress critically promotes KCNQ1 dysfunction, as the modification of cysteinyl thiols by ROS compromises the structure-function relationships of the channel [28, 99, 100]. In the transmembrane region of KCNQ1, the five native cysteines (Cys122, Cys136, Cys180, Cys214, and

Cys331) serve as potential oxidant sites. Among these, Cys214 in the S3 segment appears especially important for maintaining stable channel function under oxidative conditions. Early investigations identified the cysteine Cys214, located in the S3 segment of KCNQ1, as a critical site for such interactions [28]. Kerst and colleagues used the thimerosal, a sulfhydryl-oxidizing agent, found that thimerosal forms a direct interaction at Cys214, resulting in modified gating properties of the channel [28]. Notably, in I_{Ks} reconstitution via KCNQ1-KCNE1 expression, addition of thimerosal resulted in an increase in this current, the effect was strongly reduced when Cys214 was mutated into Ala, demonstrating this Cys214 as a important site in functional modulation [28].

Recently, the structural roles of native cysteines within KCNQ1, including Cys214 (one of five in the transmembrane domain), has been examined [101]. The study employing a truncated KCNQ1 transmembrane domain construct (amino acids 100-370) explored this by labelling cysteine side chains (including Cys214) with the MTSL spin probe, which led to detectable changes in tetramer assembly [101]. This suggests that those modifications to Cys214, beyond affecting gating, could also impair the proper assembly or stability of the channel complex.

Therefore, Cys214 is a critical residue where modifications generated by ROS can alter KCNQ1 gating [28] and potentially affect its oligomeric structure [101]. Maintaining the native state of this residue is vital for normal KCNQ1 channel function and, consequently, for cardiac rhythm stability. This highlights the therapeutic promise of protecting Cys214 from modifications caused by ROS.

2.4 Computational Approaches in Ion Channel Research

2.4.1 Molecular Docking: Principles and Scoring Functions

Molecular docking is a widely used computational approach for drug discovery and structural biology [102]. It is used to predict the binding mode and binding affinity of a ligand interacting with the target protein. In the specific context of this thesis, molecular docking represents the core tool to suggest the plausible interaction modes between bioactive compounds from TCM (such as quercetin and rutin) and the KCNQ1 channel complex.

Docking methodologies are generally classified into rigid and flexible strategies. Rigid docking uses the geometric parameters of both ligand and receptor as fixed. While this approach significantly lowers computational cost, it historically can’t model induced fit phenomenon that is critical for protein-ligand recognition. For flexible docking, the standard adopted in this study, accounts for the torsional degrees of freedom of the ligand and, crucially, the residue side-chain flexibility in the binding pocket. This is especially vital for the VSD-PD interface of KCNQ1, where residue side chains must rotate to allow binding of large polyphenolic molecules. The docking process fundamentally relies on two core components: a search algorithm and a scoring function. The search algorithm performs systematic sampling of the conformational space of the ligand-receptor complex to identify potential binding modes. While early methods assumed the molecules as rigid bodies, modern algorithms like Genetic Algorithms and Monte Carlo methods effectively manage the high dimensionality of flexible ligand docking [103].

Genetic algorithms, in particular, have gained popularity for their improved robustness in global search. As illustrated in Figure 12, genetic algorithms implement the process of natural evolution by iteratively refining ligand poses through stochastic mutation and recombination steps. In this research, genetic algorithms are employed to ensure that the predicted binding modes of MTX represent globally favorable low energy solutions rather than bias of initial placement. As an alternative, Monte Carlo sampling using random sampling techniques to identify the binding free-energy landscape of the interactions of ligand-protein complex. Docking algorithms have recently adopted machine learning techniques to enhance computational efficiency and accuracy of binding mode prediction, which provide a scoring function that approximates the binding affinity based on various factors such as long-range electrostatics, hydrogen-bond networks, hydrophobic packing, and desolvation effects upon binding, evaluating the quality of the predicted poses.

In general, scoring functions can be classified as force field-based, empirical, or knowledge-based. Force field-based scoring of interaction energy compute the energy of ligand-protein interactions via physics-based equations [104]. These methods include terms for van der Waals interactions, electrostatic forces, and occasionally solvation effects. On the other hand, parameterized empirical scoring functions use a number of weighted energy terms obtained from experimental affinity measurements. Although these functions compute faster, they might not extrapolate reliably beyond the training system. Knowledge-based scoring functions use statistical analysis of known protein-ligand complexes to infer potential functions. For this study, a consensus scoring strategy of these scoring algorithm is essential to reliably rank the TCM candidates and select the top candidates for subsequent MD validation.

The genetic algorithm process in docking can be summarized as a flowchart, illustrating the biophysical optimization of ligand poses (See Figure 12)

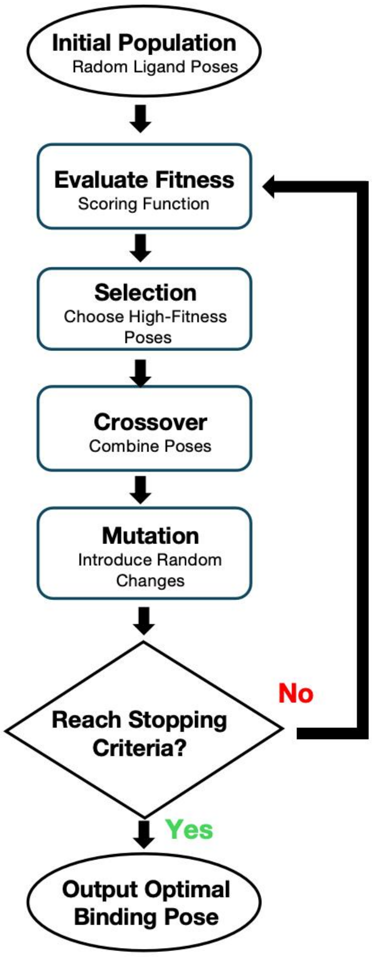

Figure 12. A flowchart of a genetic algorithm for determining the optimal binding pose of a ligand. The process is iterative, cycling through fitness evaluation, selection, crossover, and mutation until a stopping condition is satisfied.

As molecular docking is commonly employed in early drug discovery, it is especially used in the lead finding and optimization phases. For ion channel research, it provides a structural model for how small molecules modulate gating transitions. By identifying specific interaction sites (e.g., hydrogen bonds to residues in S4-S5 linker), docking offers atomic-resolution understanding that connect structure to the functional effects observed in electrophysiological experiments.

2.4.2 Molecular Dynamics Simulations: Force Fields and Sampling Approaches

Molecular dynamics (MD) simulations have developed into a crucial tool in the field of biological systems, enabling insights into the structure, dynamics, and function of biomolecules at the atomic level [105]. While static structures from cryo-EM data provide a necessary starting point, they often miss the kinetically relevant motions to describe the functional transitions of ion channels. MD simulations address this limitation by introducing the dimension of time, enabling for direct observation of dynamic processes such as pore opening and voltage-sensor movement.

MD simulations involve the time integration of Newtonian equations of motion for a set of interacting particles. Their subsequent time series of positions and velocities can be obtained by calculating the interatomic forces on each atom. By generating simulation trajectories at atomic detail that demonstrate the temporal progression of atomic positions and velocities, this procedure supports a in-depth analysis of the conformational behavior of biomolecules. For membrane proteins like KCNQ1, this method is necessary for modeling the protein in an explicit lipid bilayer context mimicking native lipid bilayer environment, resolving specific lipid-protein contacts that are often inaccessible to direct experimental observation**.**

Mathematical functions and parameters are used in established biomolecular force fields (e.g., AMBER, CHARMM, and OPLS) to approximate atom-to-atom interactions such as bond stretching, angle bending, torsional rotations, and non-bonded interactions like electrostatics and van der Waals forces. The predictive performance of these simulations depends on the potential energy function (*U*), which is formulated as:

$$U = \sum_{\text{bonds}} k_b (r - r_0)^2 + \sum_{\text{angles}} k_\theta (\theta - \theta_0)^2 + \sum_{\text{dihedrals}} k_\phi (1 + \cos(n\phi - \delta)) + \sum_{\text{non-bonded}} \left(\frac{q_i q_j}{r_{ij}} + 4\epsilon_{ij} \left[\left(\frac{\sigma_{ij}}{r_{ij}} \right)^{12} - \left(\frac{\sigma_{ij}}{r_{ij}} \right)^{6} \right] \right) \tag{1}$$

This comprehensive expression comprises bonded terms (bond stretching, angle bending, and dihedral torsions) and non-bonded terms (long-range electrostatics and short-range van der Waals interactions). In the context of this thesis, the non-bonded terms are especially critical for capturing the ion permeation pathway of KCNQ1, ensuring that the electrostatic environment underlying the ion selectivity and permeation is reliably described. To improve their description of biomolecular interactions, these force fields need continual refinement guided by experimental data and quantum mechanical calculations. Such refinements further improve quantitative agreement with experimental observation for ion-channel complexes, such as KCNQ1-KCNE1/KCNE3, embedded in an explicit phospholipid bilayer.

The feasible simulation durations and model sizes of MD simulations have increased significantly due to advances in computational infrastructure and algorithms. In particular, simulation efficiency has been greatly enhanced by the development of GPU-accelerated MD codes, such as stand software packages like GROMACS and AMBER. Furthermore, custom-designed hardware like Anton, specifically for MD simulations, has increased accessible trajectory lengths from nanoseconds to milliseconds [106]. With the aid of this ability, slower biological events like complex formation, major conformational transitions, folding dynamics can be probed computationally. These technological advancements are vital for narrowing the gap between simulation timescales and biologically relevant timescales [107]. Numerical integration often uses the Verlet algorithm for biophysical accuracy:

$$\mathrm{r}(t+\Delta t) = 2\mathrm{r}(t) - \mathrm{r}(t-\Delta t) + \frac{\mathrm{F}(t)}{m}(\Delta t)^2 \tag{2}$$

This symplectic integrator improves long-time energy stability in MD runs, enabling characterization of slow processes like KCNQ conformational changes. For velocity updates, the velocity-Verlet variant extends in the following way:

$$\mathrm{v}(t+\Delta t) = \mathrm{v}(t) + \frac{1}{2m}[\mathrm{F}(t) + \mathrm{F}(t+\Delta t)]\Delta t \tag{3}$$

To deal with sampling efficiency constraints, enhanced sampling approaches have been developed. Methods like replica exchange molecular dynamics (REMD), metadynamics, and umbrella sampling can access rare events and reconstruct free energy [108]. Typically, REMD includes multiple simulations at different temperatures to improve exploration of conformational space. In contrast, metadynamics adds a history-dependent bias to the potential energy surface in order to accelerate state transitions [109], with the bias potential formulated as:

$$V(s,t) = \sum_{t'<t} w \exp\left(-\frac{\left(s-s(t')\right)^2}{2\sigma^2}\right) \tag{4}$$

where *s* denotes the collective variable, *w* specifies the Gaussian hill height, and *σ* sets the Gaussian width, facilitating investigation of energy barriers across KCNQ gating transitions.

Umbrella sampling conducts multiple biased simulations to estimate free energy differences along a chosen reaction coordinate. These techniques have proven useful in probing complex phenomena like ligand binding and unbinding, conformational rearrangements, and the thermodynamics profiles of biomolecular events.

In recent years, combing MD simulations and experimental data in a hybrid framework has become crucial. For this thesis, the computational models are not treated as stand-alone entities but are continuously validated against patch-clamp results and cryo-EM structures [110]. This integrative strategy uses the strengths of both computational prediction and experimental verification to provide a comprehensive understanding of the structure-function relationship of KCNQ1.

As force fields and sampling methods evolve, MD simulations play an increasingly significant role in elucidating biomolecular mechanisms. Future efforts will focus on the simulation of larger macromolecular assemblies and longer timescales, narrowing the gap from molecular-level interactions to systems biology. These developments will further deepen our understanding of biological systems at unprecedented levels of detail, directly guilding the rational design of therapeutic treatments for channelopathies.

2.5 Methodological Principles for Assessing Antioxidant Capacity

2.5.1 Principles of Total Phenolic Content Assessment

Determination of total phenolic content (TPC) is a common assay in studies when evaluating the antioxidant properties of plant extracts. Phenolic compounds are known contributors to antioxidant activity as a result of their capacity to act as reductants, donate electrons or hydrogen atoms, and chelat metal ions [111, 112]. Hence, TPC measurements provide an indicator of this class of potential antioxidants [113-115].

The Folin–Ciocalteu (F-C) colorimetric assay is the most widely used method for TPC estimation, where phenolics reduce phosphomolybdic or phosphotungstic complexes in basic conditions [116]. This reductive reaction generates blue products, considered to be reduced heteropolyacid complexes, whose spectral absorbance intensity is proportional to the amount of reducing substances [116]. In general, the method usually consist of a preliminary extraction of polyphenolic constituents from the plant source employing solvents such as methanol or aqueous ethanol. The extract is then reacted with the Folin-Ciocalteu reagent, subsequently introduced alkaline solution, most often sodium carbonate, to increase the pH and enhance the oxidation-reduction reaction. Following an incubation to allow color to develop, the absorbance of the blue solution is measured by UV-Vis spectrophotometry, usually at a absorption maximum around 760-765 nm. Quantification is achieved by comparing the sample absorbance derived by interpolation from a calibration curve generated using a reference compound, most often gallic acid. Results are typically presented as mass equivalents of the standard (e.g., mg of gallic acid equivalents per gram of material) [112, 114-116].

A major limitation of the F-C assay is its vulnerability to interfering effects, as the reagent is not selective to phenolic compounds; it can also be reduced by various non-phenolic reductants commonly found in plant extracts. These include agents including ascorbic acid, certain amino acids like tyrosine and tryptophan, proteins, and reducing sugars [116]. Consequently, this assay provides a measure reflecting the total reducing ability of the sample under the specific assay conditions, meaning the resulting value is an approximate estimate rather than an absolute quantification of phenolic content.

Despite this non-specificity, the F-C method is broadly used because it is simple, rapid, inexpensive, and highly reproducible. It provides a useful and practical ways for screening and comparing the relative abundance of phenolic antioxidants and total reducing capacity among different plant samples.

2.5.2 Ferric Reducing Antioxidant Power Assay

The Ferric Reducing Antioxidant Power (FRAP) assay provides a complementary method to evaluate total antioxidant capacity, focusing on electron-transfer mechanisms. The FRAP assay represents a widely adopted methodology for quantifying total antioxidant capacity, which evaluates antioxidant potential based on the ferric iron (Fe^{3+}) reduction to its ferrous state (Fe^{2+}) [117]. Originally proposed for the assessment of antioxidant status in plasma [117], its application has since been used across various sample types [118]. The underlying basis is the electron-donating capacity of the antioxidant species present in the sample. This assay is carried out at an acidic pH of 3.6, conditions selected to preserve iron solubility and facilitate the requisite redox reaction. Under acidic conditions, antioxidants function as reductants, donating electrons to transform the ferric-tripyridyltriazine complex (Fe^{3+}-TPTZ) into its ferrous form (Fe^{2+}-TPTZ) [117, 119]. This reduction yields a colored blue ferrous complex, the formation of which is quantified by the absorbance measurement, typically at 593 nm. The intensity of the absorbance measured is directly proportional to the total reducing power of the sample.

The procedure generally consist of mixing the sample extract with a freshly made FRAP working solution. This reagent is composed of TPTZ, $FeCl_3$, and an acetate-buffered medium, which maintain the necessary acidic pH. Following a defined incubation time allowing for the redox reaction to occur. The absorbance is determined using a spectrophotometer. Quantification is obtained by comparing the absorbance signal of the sample with a standard curve, usually established using ferrous sulfate ($FeSO_4 \cdot 7H_2O$) standards at known concentrations . Outcomes are typically presented as FRAP values, corresponding to the molar amount of Fe^{2+} that produces an similar absorbance intensity [117, 118].

After its original development for plasma assessment [117], the FRAP methodology has been extensively used with methodological adjustments, for assessing antioxidant potential in a wide range of biological samples, including foods and plant extracts. Its use has been reported in the assessment of dietary polyphenols and various types of tea [118], common vegetables [120], and different small fruits [121], thereby providing a practical method for comparative assessment of reducing capacities across different sample sources. Modifications to the protocol, particularly the prolonging of the reaction time relative to the conventional four minutes, have been proposed to enable a more complete measurement accounting for antioxidants characterized by slower reaction rates, including specific polyphenolic species [122].

Notable advantages supporting widespread adoption of the FRAP assay include its simple workflow, rapid analysis, cost-efficiency, and excellent reproducibility, attributes conducive to high-throughput screening applications. The assay provides a direct quantification of a total reducing potential of the sample, reflecting its electron-donating capacity.

However, the FRAP assay measures ferric ion reducing capacity, a condition which may not correlate directly with free radical scavenging activity determined via alternative methodologies such as ABTS or DPPH. Moreover, the assay works under non-physiological low-pH conditions (pH 3.6), revealing that the observed antioxidant responses may not accurately correspond to in vivo performance. Significantly, the standard FRAP protocol demonstrates low sensitivity to thiol-containing antioxidants, including the biologically relevant glutathione, and is insensitive to detect antioxidants functioning via hydrogen atom transfer (HAT) mechanisms [119]. Considerable variations in reaction rates among different antioxidant compounds can also occur, potentially resulting in an underestimation slower-reacting antioxidant under the standard, comparatively short incubation time.

2.5.3 Lipid Peroxidation Inhibition Assays and Mechanisms

Peroxidative lipid damage, specifically the oxidative decomposition of polyunsaturated fatty acids (PUFAs), represents a key aspect of cellular damage induced by oxidative stress and implicated in aging and a range of diseases [123-125]. This process follows initiation, chain propagation mediated by lipid peroxyl radicals (LOO•), and termination steps, affected by factors like unsaturation and catalytic metals [125-127]. It causes cellular damage, including the generation of cytotoxic aldehydes like the aldehydic marker malondialdehyde (MDA), highlighting the importance of examing antioxidant interventions that limit peroxidation reaction [128].

Antioxidants inhibit lipid peroxidation predominantly via preventative mechanisms, such as scavenging ROS precursors or chelating pro-oxidant metal ions, or via chain-breaking activity, typically involving hydrogen transfer to LOO• intermediates to discrupt the propagation loop [123]. The effectiveness of chain-breaking antioxidants is determined by the stabilization of the resulting antioxidant radical product [129]. These mechanisms provide the foundation for experimentally evaluating antioxidant potential.

In vitro assessment of lipid peroxidation inhibition generally involves initiating oxidation in a lipid system and comparing the reaction kinetics under the antioxidant treatment versus control one. Methodologies differ substantially with respect to lipid substrates(from simple fatty acids to complex membrane model), oxidizing triggers, metal ions as an example, and the selected chemical markers quantified, which include conjugated diene formation, early-stage hydroperoxide, or secondary oxidation products like those assayed by the TBARS method [125, 127, 129].

Guided by these general principles, assessing the antioxidant properties of substances, such as TCM extracts, frequently involves assessing their capacity to reduce lipid peroxidation within physiologically pertinent environments like blood plasma. A common and useful strategy applies the Fenton reaction (utilizing H_2O_2 and Fe^{2+}, typically from $FeSO_4$) to generate oxidative stress under ex vivo conditions [127, 129]. This system effectively generates highly reactive hydroxyl radicals (•OH), potent initiators of the lipid peroxidation chain reaction, thereby mimicking certain diseases conditions involving metal-ion-driven oxidative damage [123, 127]. Quantifying the accumulation of thiobarbituric acid reactive substances (TBARS), which mainly represents MDA, a secondary byproduct of PUFA oxidation, which serves as frequently adopted but non-specific indicator for quantifying the magnitude of lipid peroxidation. The inclusion of effective controls is necessary in this method. Comparing the TBARS levels in plasma subjected to the Fenton reaction under standardized incubation conditions (e.g., 37 °C for a defined period) against baseline levels (plasma alone) and immediate post-reagent addition measurements confirms the efficacy of prooxidant treatment and establishes the window for observing potential inhibitory effects derived from the test compounds (TCM extracts in this study). This specific methodological technique enables systematic screening and comparison of compounds, which contain protective diverse agents against induced oxidative lipid damage in a complex biological environment.

Interpreting data from such in vitro studies depends on considering their intrinsic limitations. The observed antioxidant activity is strongly influenced by specific assay settings (substrate, initiator, concentration, physical state), and simplified experimental models cannot fully reproduce in vivo biological complexity. Consequently, using several complementary assays are needed for a comprehensive evaluation, and a detailed understanding of assay mechanisms is required for interpreting findings to potential physiological relevance.

2.6 Natural Compounds for KCNQ1 Modulation and Antioxidant Protection

2.6.1 Selection of Candidate Sources from the Medicine and Food Homology List

To screen for new natural modulators of KCNQ1 with strong translational potential, this study selected materials classified from Medicine and Food Homology (MFH) list. This classification denotes a historically documented safety profile appropriate for long-term consumption as food, which is a critical prerequisite for chronic diseases management.

In 2020, the MFH list was updated to include nine additional TCM species [130]. These nine species were selected as the initial screening collection for this study to determine their antioxidant capacity and potential effects on channel function. The candidate library includes *Dendrobium officinale (D. officinale)*, *Ganoderma lucidum (G. lucidum)*, *Gastrodia elata (G. elata)*, *Cornus officinalis (C.officinalis)*, *E. ulmoides*, *Cistanche deserticola (C. deserticola)*, *Astragalus membranaceus (A.membranaceus)*, *Panax quinquefolius (P.quinquefolius)*, and *Codonopsis pilosula (C.pilosula)*. While these species have diverse traditional indications ranging from immune regulation to neuroprotection, modern phytochemical analyses have identified that they share a common feature: a high abundance of redox-active small molecules, such as polysaccharides, flavonoids, and phenols (summarized in Table 2).

Table 2. The nine selected TCM candidates and their major bioactive constituents

Latin Name	**Abbreviation**	**Common Name**	**Major Bioactive Class**	**Key Bioactivities**
Dendrobium officinale	*D. officinale*	Shihu	Polysaccharides	Antioxidant, anti-tumor/ cytoprotective [131]
Ganoderma lucidum	*G. lucidum*	Reishi Mushroom	Polysaccharides	Immunomodulation [132], radical scavenging [133]
Gastrodia elata	*G. elata*	Tianma	Phenolic compounds	Neuroprotection, anticonvulsant [134-136]
Cornus officinalis	*C. officinalis*	Asiatic Dogwood	Iridoid glycosides	Hypoglycemic [137], antioxidant [138]
Eucommia ulmoides	*E. ulmoides*	Du Zhong	Flavonoids, Lignans	Antihypertensive, antioxidant [139-141]
Cistanche deserticola	*C. deserticola*	Desert-broomrape	Phenylethanoid glycosides	Fatigue resistance [142], antioxidant [143]
Astragalus membranaceus	*A. membranaceus*	Mongolian Milkvetch	Polysaccharides	Immunomodulation [144, 145], cardioprotection [146]
Panax quinquefolius	*P. quinquefolius*	American Ginseng	Saponins (Ginsenosides)	Glucose regulation [147], cardioprotection [148]
Codonopsis pilosula	*C. pilosula*	Dangshen	Polysaccharides	Anti-fatigue, antioxidant [149]

Within the screened set of candidates, *E. ulmoides* was identified as a candidate of particular interest to this investigation. Although *E. ulmoides* have been traditionally used for strengthening musculoskeletal and endocrine functions, modern pharmacological studies have highlighted its vital role in the cardiovascular system, particularly with respect to blood pressure regulation and oxidative stress mitigation [150]. The therapeutic effects of *E. ulmoides* leaves is mainly attributed to their high levels of secondary metabolites. Phytochemical analyses has revealed that the leaves are notably rich in chlorogenic acid as well as flavonoid constituents, with rutin and quercetin as prominent examples

[151, 152]. Previous work have demonstrated that water extracts of *E. ulmoides* leaves can effectively reduce membrane lipid peroxidation and scavenge radical species [139], properties that are important for protecting membrane-integrated proteins like KCNQ1 from oxidation-induced damage. Moreover, the specific flavonoids present in *E. ulmoides* (rutin and quercetin) have similar structural features, characterized by multiple hydroxyl groups and aromatic rings, that make them suitable candidates for both direct antioxidant action and ligand-protein interactions. Therefore, *E. ulmoides* was selected as the lead candidate for the further mechanistic study.

2.6.2 Bioactive Compounds from MFH Candidates

Antioxidants Element from *E. ulmoides*: Rutin and Quercetin

E. ulmoides is widely viewed as a valuable medicinal herb in TCM practice. Modern scientific research has provided growing evidence supporting its therapeutic efficacy of *E. ulmoides*, commonly attributing to its richness in content of bioactive molecules, particularly flavonoids [141]. Among its constituents, quercetin and rutin have drawn broad attention given their potent antioxidant properties [153, 154]. Oxidative stress, resulting from an imbalance between the generation of ROS and the capacity of biological systems to neutralize these reactive intermediates, is involved in the development of various chronic and degenerative pathologies. Natural derived antioxidants, particularly those obtained from MFH sources like *E. ulmoides*, have gained increasing interest as potential agents to prevent or reduce damage associated with oxidative stress.

Quercetin, a flavonol aglycone, and rutin, its rutinoside derivative, are the major flavonoid constituents in *E. ulmoides* leaves, with rutin at a concentration of 0.0644 mg/g and quercetin at 0.0302 mg/g (dry weight) [152]. Furthermore, in enriched flavonoid fractions from the leaves, rutin and quercetin account for 27.14±1.14% and 2.32±0.24% of the purified extract, respectively [140]. These two molecules, due to their abundance and potent antioxidant properties, are regarded as the principal contributors to the antioxidant activity of *E. ulmoides*.

Chemical Nature of Rutin and Quercetin

Quercetin (3,3',4',5,7-pentahydroxyflavone) is a well-known dietary flavonol distinguished by its polyphenolic structure, which is key to its antioxidant activity. Rutin (quercetin-3-O-rutinoside or rutoside), is generated when the disaccharide rutinose is attached to the 3-hydroxyl group of quercetin

[154]. This glycosylation alter the physicochemical properties of the molecule, such as aqueous solubility and bioavailability.

Numerous studies have verified the presence of both quercetin and rutin across multiple anatomical parts of *E. ulmoides* [140, 152]. Peng et al. [141] compiled evidence on the biological properties of extracts from the bark, leaf, staminate flower, and seed, highlighting the presence of key bioactive compounds, including flavonoids. Quantitative analyses, typically using High-Performance Liquid Chromatography (HPLC), have been performed to assess their concentrations. For instance, Zhou et al. [152] provided a comparative analysis of chemical components in the barks and leaves, identifying quercetin among other constituents. Later studies, such as those by Wu et al. [140] and Hou et al. [155], specifically highlighted that *E. ulmoides* leaves are particularly enrich in both rutin and quercetin, contributing significantly to their total antioxidant capacity. The comprehensive determination of seven polyphenols, including rutin and quercetin, in the leaves, barks, and fruits of *E. ulmoides* further indicates their widespread distribution within the plant [155]. As shown in Figure 13, the chemical structures illustrate their molecular similarities and differences.

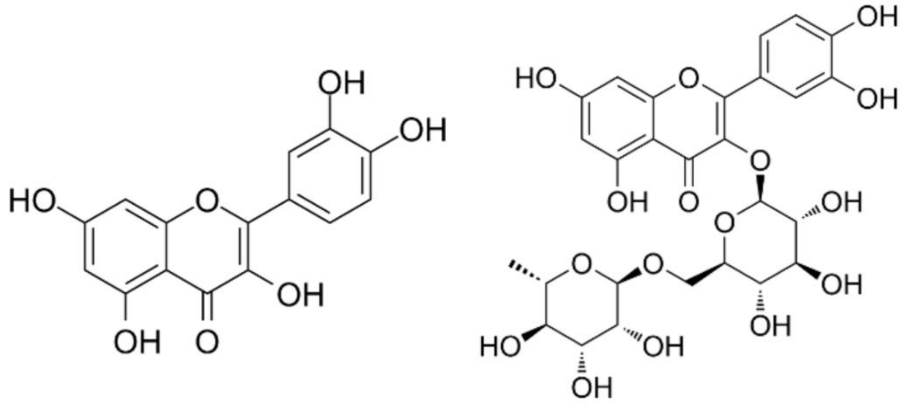

Quercetin **Rutin**

Figure 13. Chemical structure of quercetin and rutin. The molecular structures highlight the glycosylation in rutin that differentiates it from quercetin.

Antioxidant Mechanisms of Quercetin and Rutin

The antioxidant prowess of quercetin and rutin reflects multiple mechanisms, facilitating efficient defense against oxidative stress.

Quercetin's antioxidant activity has been widely studied. As described by Xu et al. [153], its strong antioxidant effects include direct scavenging of ROS, thereby reducing damage to cellular macromolecules like DNA, proteins, and lipids. In additional to direct scavenging, quercetin can affect endogenous antioxidant systems by boosting the levels or activity of glutathione along with major antioxidant enzymes [156]. It also modulates diverse signal transduction pathways associated with cellular responses to oxidative stress. Furthermore, the capacity of quercetin to chelate transition metal ions, such as iron and copper, prevents their engagement in Fenton reactions that give rise to highly reactive hydroxyl radicals [157].

The interaction of quercetin with biological membranes is another crucial aspect of its antioxidant function. It was reported that quercetin preferentially inserts into lipid bilayers, as demonstrated with DOPC liposomes [158]. Furthermore, it tends to localizes at the membrane-water interface, with its chromophore situated within the polar head group region [159]. This strategic orientation is vital for its ability to quench ROS. The nature of quercetin interaction is also sensitive to the specific lipid environment. Study showed that quercetin demonstrates a strong affinity for more fluid, liquid-disordered membrane domains, integrating into these areas with minimal structural perturbation [160]. In contrast, quercetin can elicit notable structural disturbances within more ordered, cholesterol- and sphingolipid-rich liquid-ordered domains [160], indicating its potential to modulate the organization of these specialized membrane areas.

Furthermore, once embedded in the membrane, quercetin can engage in synergistic antioxidant processes. Investigation has identified its ability to assemble non-covalent complexes with other lipophilic antioxidants, such as vitamin E, within the bilayer [158]. These interactions are considered to prompt cooperative antioxidant effects. The consequences of these molecular interactions are detectable in both model membrane and cellular systems [158, 160, 161]. In cellular contexts, its accumulation in cell membranes of human skin fibroblasts correlates with discernible ultrastructural changes within these membranous compartments [159].

Rutin

Rutin, the 3-O-rutinoside of quercetin, represents another essential antioxidant flavonoid found abundantly in *E. ulmoides*, with highest level in leaves. While sharing the core flavonol structure with quercetin, the attachment of the bulky disaccharide, rutinose, affects its physicochemical profile thus influencing its mode of antioxidant action and interactions in biological systems. This glycosylation usually improves water solubility relative to its aglycone, which may affect its distribution across biological compartments and its interactions with cellular macromolecules [162].

The antioxidant capacity of rutin has been broadly supported by numerous in vitro and in vivo studies [154, 162-164]. Like quercetin, rutin is capable of directly scavenging a range of ROS, thereby protecting cellular structures against oxidative damage. This scavenging ability is commonly due to the presence of phenolic hydroxyl groups, which capable of donating hydrogen atoms or electrons to terminate radical chain reactions. Studies evaluating extracts from *E. ulmoides* containing high rutin levels have demonstrated its significant contribution to the total antioxidant potential, typically measured via assays such as DPPH and ABTS radical scavenging [143]. Furthermore, evidence implies that enzymatic modifications, such as the formation of poly(rutin), could strengthen its its antioxidant properties [165].

Rutin interacts with membranes, critical sites for lipid peroxidation, in a manner different from quercetin largely due to the steric influence of the bulky rutinose group [166]. For instance, it has been shown to inhibit lipid peroxidation in biological samples such as rat brain and liver homogenates [163], suggesting it can effectively address oxidative threats at or near membrane surfaces.

2.6.3 Natural Activators for KCNQ1: Quercetin, Tanshinone IIA and Resveratrol

Following the antioxidant roles of quercetin and rutin, this subsection explores naturally derived compounds that directly activate KCNQ1, yielding dual benefits in channel modulation and oxidative in cardiovascular health protection. Quercetin is of particular relevance to the present study, as it is both a major constituent of *E. ulmoides* and an reported KCNQ1 modulator. Additionally, tanshinone IIA and resveratrol are reviewed here as established reference activators, supplying a mechanistic rationale for the comparative analysis of ligand-binding interactions.

Quercetin, a flavonoid widely distributed in fruits and vegetables such as apples, onions, berries, and capers, exhibits a unique pharmacological property as a voltage-dependent activator of multiple KCNQ channels. Electrophysiological characterization shows that quercetin strongly activates KCNQ1-KCNE1 heteromeric channels, leading to a marked negative shift in the voltage dependence of activation and increased current amplitude at physiologically relevant potentials [27]. This modulation applies to KCNQ2/3 and KCNQ4 channels, but does not include KCNQ5, revealing selective interaction with specific structural elements within the KCNQ channel family [167]. Apart from influencing KCNQ channels, quercetin demonstrates complex effects on other ion channels, including activation of L-type Ca^{2+} channels in smooth muscle cells of rat tail artery [167] and modulation of K+ channels on the basolateral side of rat distal colon epithelium [168]. The broad modulatory effect of quercetin on ion channels implies potential therapeutic applications, combined with its antioxidant properties, making it a promising therapeutic candidate for treatment of complex cardiovascular disorders.

Tanshinone IIA, derived from the dried root of *Salvia miltiorrhiza* (Danshen), exhibits selective activation of KCNQ1/KCNE1 channels. Electrophysiological studies show that its boosts I_{Ks} currents without altering normal gating kinetics [25]. In addition to its direct ion channel modulation, tanshinone IIA blocks harmful cardiac restructuring by suppressing pro-fibrotic signaling pathways, as demonstrated in preclinical models of cardiac hypertrophy. Moreover, it stimulates the Nrf2/HO-1 pathway for antioxidant defense, providing complementary protection to the heart from oxidative stress [169]. Recent studies also found potential of tanshinone IIA in treating arrhythmias through potassium channel modulation, specifically by enhancing I_{Ks} currents, though vital evidence remains preliminary [170]. Furthermore, tanshinone IIA regulates the expression of cardiac microRNA-1t to lower the risk of arrhythmogenesis [171] and modulates pacemaker function by HCN channel modulation [172]. TCM studies support synergistic effects when interacting with other natural channel modulators [173].

Resveratrol, another phytocompound, derived from sources such as grapes, berries, and peanuts, is identified as activator for KCNQ1 channel, contributing to its cardiovascular protective effects [26, 174]. While perhaps more extensively characterized for other signaling pathways, its interaction with KCNQ1/KCNE1 channels, potentially involving modulatory effects on channel gating or current density [26]. Apart from its enhancing effects on KCNQ1-mediated currents, its salutary cardiovascular actions are exceptionally strong. More researches show that it can activate SIRT1-dependent pathways important for cellular health, stress resistance, and extended lifespan, but also enhancing mitochondrial performance and growth, owning to heart protection [26, 174]. In addition to KCNQ1, it also plays modulatory role in other vital ion channels. For instance, it can regulate ATP-sensitive potassium (KATP) channels and inhibit activity of L-type calcium channels, which revealing its vasorelaxant and anti-arrhythmic potential [174]. As shown in Figure 14, the chemical structures of tanshinone IIA and resveratrol highlight their molecular features as KCNQ1 activators.

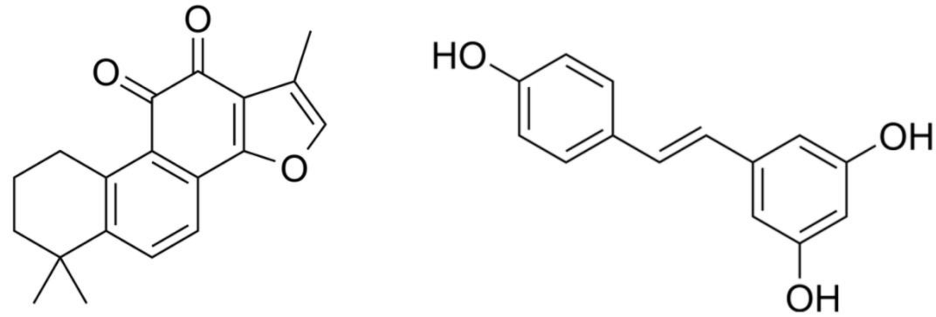

Tanshinone IIA **Resveratrol**

Figure 14. (A) Chemical structure of Tanshinone IIA and (B) Resveratrol

3. Materials and Methods

3.1 Materials

3.1.1 Reagents and Plant Materials

To ensure the pharmacological consistency and reproducibility of the study, strict quality control measures were applied to all raw materials. All dried TCM plant materials, with the exception of *E. ulmoides*, were purchased from certified pharmacies of Beijing Tong Ren Tang (Shenzhen, China), a supplier renowned for its standardization of herbal products. *E. ulmoides* was procured from a certified commercial supplier (Ali Health, Alibaba Group, China). The specific plant parts used in this study included dry preparations of *D. officinale* stems and *A. membranaceus* roots, *G. lucidum* fruiting bodies, *G. elata* rhizomes, *C. officinalis* berries, *E. ulmoides* leaves, and the roots of *C. deserticola*, *P. quinquefolius* and *C. pilosula*. To ensure reproducibility and quality control, all powders were sourced from the same production batches. Chemical reagents employed in the biochemical assays were of analytical grade and prepared fresh to avoid degradation. These included deionized water, Folin-Ciocalteu reagent (Sigma-Aldrich, St. Louis, MO, USA), sodium carbonate (Na_2CO_3), chlorogenic acid standard, ferric chloride hexahydrate ($FeCl_3 \cdot 6H_2O$), acetate buffer (pH 3.6), 2,4,6-tripyridyl-s-triazine (TPTZ) solution (10 mM TPTZ dissolved in 40 mM HCl), hydrogen peroxide (H_2O_2), ferrous sulfate ($FeSO_4$), and thiobarbituric acid (TBA).

3.1.2 Software, Servers, and Databases

Computational modeling and simulations were performed using a comprehensive suite of software and web servers. Structure preparation and modeling were performed using Maestro (v13.4.132, Schrödinger, LLC, New York, NY, USA), and the initial *ab initio* prediction of unresolved regions of KCNQ1 was built using AlphaFold2-multimer (v2.3) [175] via the ColabFold web server [176]. Visualization and density map fitting were carried out using UCSF ChimeraX (v1.5rc) [177], PyMOL (version 2.5, Schrödinger, LLC) [178] and VMD 1.9.4 [179]. System construction for MD was facilitated by the CHARMM-GUI Membrane Builder server (https://www.charmm-gui.org/) [180], which allowed for the generation of biologically accurate lipid bilayers. Molecular docking preparation was performed using AutoDock Tools 1.5.7 [181], and docking calculations were conducted using

AutoDock Vina 1.1.2 (Scripps Research, La Jolla, CA, USA) [182]. MD simulations were carried out using GROMACS 2018.4 [183]. Post-simulation analysis and visualization were implemented using LigPlot+ v.1.0 (European Bioinformatics Institute, Hinxton, UK) [184], CCBuilder [185], and GraphPad Prism v. 8.1 (GraphPad Software Inc., San Diego, CA, USA).

Structural data for the proteins were obtained from the RCSB Protein Data Bank (PDB), including the cryo-EM structures of human KCNQ1 (PDB ID: 7XNK; Resolution: 2.6 Å), the human KCNQ1-KCNE3-CaM complex with PIP_2 (PDB ID: 6V01; Resolution: 3.9 Å), and the KCNQ1-CaM complex (PDB ID: 6UZZ; Resolution: 3.1 Å). Additionally, the cryo-EM density map used for linker modeling was accessed via the Electron Microscopy Data Bank (EMD-20966). Furthermore, the 3D chemical structures of ligands, including Tanshinone IIA (CID: 164676), Resveratrol (CID: 445154), ML277 (CID: 53347902), Mallotoxin (MTX; CID: 5281847), Rutin (CID: 5280805), and Quercetin (CID: 5280343), were retrieved from the PubChem database (https://pubchem.ncbi.nlm.nih.gov/) [186].

3.2 Methods

3.2.1 Structural Modeling of KCNQ1 Complexes

To provide a comprehensive framework for the computational analyses, the overall workflow employed in this study, ranging from system preparation to trajectory analysis, is illustrated in Figure 15.

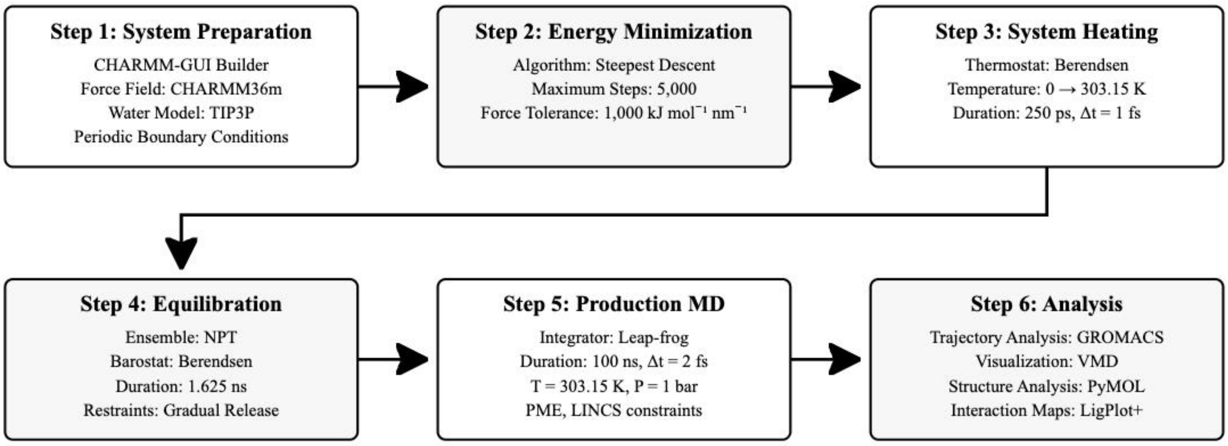

Figure 15. Molecular dynamics simulation workflow for protein-ligand complex analysis. The workflow consists of six main steps from system preparation to final analysis and visualization.

Homology Modeling of KCNQ1-KCNE1 Complex

To investigate the structural basis of MTX modulation (Results 4.1), a homology model of the human KCNQ1-KCNE1 complex was constructed. Given the absence of a full-length experimental structure for the KCNQ1-KCNE1 complex, the high-resolution cryo-EM structure of the KCNQ1-KCNE3 complex (PDB ID: 6V01) served as the template. Pairwise sequence alignment was extracted from multiple sequence alignment of KCNE family obtained from Pfam database ([187]) (https://www.ebi.ac.uk/interpro/entry/pfam/PF02060/) to map the target KCNE1 sequence onto the KCNE3 template. Although the sequence identity between KCNE1 and KCNE3 transmembrane domains is approximately 28%, the conserved helical topology and the similar binding interface on the KCNQ1 pore domain supported this template choice. The model was built using Maestro. The resulting model quality was assessed by Ramachandran plot analysis (ProCheck [188]) to ensure no steric clashes in backbone torsion angles and verification of hydrophobic packing within the transmembrane interface.

Cryo-EM Density-Guided Modeling of the HC-HD Linker

The unresolved HC-HD region (residues 535-625) was modeled using a hybrid approach (Results 4.2). An initial structural prediction was generated using AlphaFold2-multimer via ColabFold, which uses evolutionary information to predict protein folds with high accuracy. This model was carefully fitted into the experimental cryo-EM density map (EMD-20966) using UCSF ChimeraX. Discrepancies between the AlphaFold prediction and the density map were manually corrected. The HD was extended using CCBuilder to match the elongated density features. The final domain-swapped model was refined using local refinement protocols in UCSF ChimeraX to make density consistency and minimize steric clashes.

3.2.2 Molecular Interaction Studies: Docking and Simulation

Molecular Docking Protocols

Molecular docking was performed before system construction to generate the initial protein-ligand complexes. Molecular docking was performed using AutoDock Vina 1.1.2 with an exhaustiveness of 9. To investigate the binding mechanism of MTX within the KCNQ1-KCNE1 complex (Results 4.1), docking was performed targeting the transmembrane interface of the homology model constructed in Section 3.2.1. For the KCNQ1 activator studies (Results 4.4), the docking protocol was first validated by re-docking ML277 into its native pocket (PDB ID: 7XNK). The validation criterion was defined as the root mean square deviation (RMSD) between the heavy atoms of the re-docked pose and the co-crystallized ligand. An RMSD value of < 2 Å was considered an acceptable reproduction of the binding mode [189]. The grid box (30 × 30 × 30 Å) was placed on the ML277 binding site. Tanshinone IIA, resveratrol, and quercetin were subsequently docked into this validated ML277-binding pocket to predict their binding modes.

To explore the structural basis of the putative protective mechanism (Results 4.5), a separate targeted docking run was performed on the extracellular surface near residue Cys214. The grid box was defined to encompass the solvent-exposed region surrounding Cys214. Rutin and Quercetin were docked to explore the spatial feasibility of transient surface interactions which may capable of physically shielding this redox-sensitive residue from oxidative agents.

System Construction for MD Simulations

To mimic the native physiological environment, all simulation systems were constructed using the CHARMM-GUI Membrane Builder [180, 190]. For mutation studies (Results 4.3): The cryo-EM structure (PDB ID: 6V01) was truncated to retain KCNQ1 residues 104-356 and KCNE3 residues 53-92. Point mutations (D242N and R243H) were introduced using the PyMOL mutagenesis wizard, selecting rotamers with minimal steric clashes. The complex was embedded in a lipid bilayer composed of POPC: POPG: Cholesterol (90:5:5) to reproduce the cardiac membrane environment. For ligand activation studies (Results 4.4): The KCNQ1 structure (PDB ID: 7XNK) was truncated (residues 104-356), and docked complexes generated in the previous step were embedded in a POPC bilayer.

All systems were solvated with TIP3P water molecules [191] and neutralized with 0.15 M KCl. The simulation box dimensions were set to ensure a minimum distance of 12 Å between the protein and the box edge to prevent periodic image artifacts. The final configuration of the physiological simulation system is illustrated in Figure 16.

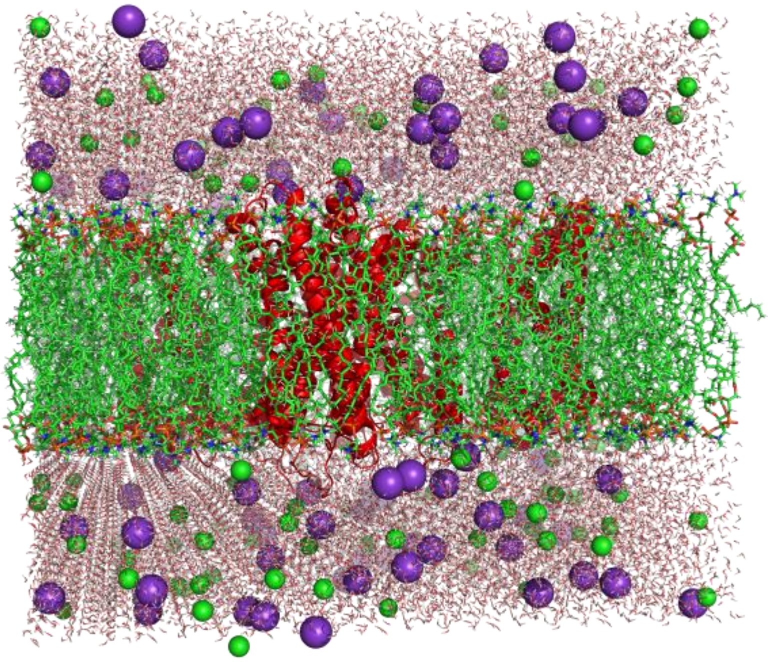

Figure 16. System for the molecular dynamics simulation. The snapshot illustrates the initial configuration of the KCNQ1-KCNE3-PIP_2 complex embedded in a hydrated lipid bilayer system. The complex is shown in the center (red representation) and is inserted into a membrane bilayer composed of POPC/POPG (green representation). The entire system is solvated with TIP3P water molecules (red and white molecules in the background) and contains potassium (purple spheres) and chloride (green spheres) ions to mimic a physiological concentration of 0.15 M KCl. The system was generated using the CHARMM-GUI server.

Molecular Dynamics Simulation Protocol

Simulations were performed using GROMACS 2018.4 with the CHARMM36m force field for proteins [192], CHARMM36 for lipids [193], and CGenFF for ligands [194]. Systems were processed by energy minimization (5000 steps, steepest descent) to remove steric clashes. Equilibration was performed in two phases: a 125 ps NVT (constant number of particles, volume, and temperature) ensemble heating step to 303.15 K using the Berendsen thermostat [195], followed by a 1 ns NPT (constant number of particles, pressure, and temperature) ensemble pressurization step to 1 bar. The temperature of 303.15 K was selected to ensure membrane bilayer phase stability while approximating physiological conditions. Positional restraints on the backbone were gradually released from 1000 to 0 $kJ \cdot mol^{-1} \cdot nm^{-2}$ during equilibration. Production runs of 100 ns were carried out for each system with a time step of 2 fs to ensure sampling consistency. While full channel gating transitions occur on microsecond to millisecond timescales, the initial 100 ns window is useful for establishing a locally relaxed bound-state configuration and capturing early induced-fit rearrangements of the binding pocket. Therefore, this study specifically focuses on characterizing the local conformational dynamics and side-chain rearrangements that set the stage for large-scale domain movements. This timescale effectively captures the early-stage conformational change and interaction stability of the ligand within the binding pocket relative to the initial docked pose, functioning as a necessary prerequisite for future microsecond-scale investigations. Temperature was maintained using the Nose-Hoover thermostat [196], and pressure using the Parrinello-Rahman barostat [197] with semi-isotropic coupling. Long-range electrostatics were calculated using the Particle Mesh Ewald (PME) method [198] with a cutoff of 1.2 nm for van der Waals interactions. Trajectories were saved at 10 ps intervals for subsequent analysis.

Trajectory and Structural Analysis

Structural stability and flexibility were assessed by calculating RMSD, RMSF (root mean square fluctuation), Rg, and SASA (solvent accessible surface area) using GROMACS tools. Principal Component Analysis (PCA) was performed on the backbone atoms of KCNQ1 Chain A to extract dominant motions, and the covariance matrix was diagonalized to obtain eigenvectors and eigenvalues. The first two principal components were projected to visualize the conformational space. Hydrogen bonds were defined by a donor-acceptor distance < 3.5 Å and angle > 120°. Ligand-protein contacts were visualized using LigPlot+. Additionally, electrostatic potential (ESP) maps were calculated using VMD's PMEpot plugin. Surfaces were colored from -5 kT/e (red) to +5 kT/e (blue) to analyze the charge distribution in the pore region, which is critical for understanding ion selectivity.

3.2.3 Preparation and Antioxidant Assessment of TCM Extracts

Preparation of Aqueous Extracts

To empirically validate the putative protective mechanism proposed in Results 4.5, a "screening-to-mechanism" experimental strategy was employed. This approach depends on the initial screening of candidate extracts for potent antioxidant capacity to identify the optimal species for subsequent molecular mechanistic investigation. Nine TCMs newly added to the official 2020 MFH list were selected for comparative evaluation of antioxidant capacity. To ensure the pharmacological relevance of the study, aqueous extracts were prepared to simulate the traditional administration of medicinal infusions and decoctions. The extraction protocol was adapted from established procedures [199]. Dry plant materials were ground into fine powder using a mortar and pestle. For each sample, 0.25 g of powder was suspended in 5 mL of deionized water and incubated in a shaking water bath at 80 °C for 30 min. The resulting infusion was cooled to room temperature and centrifuged at 4000 rpm for 10 min. The supernatant was filtered through a 0.45 μm Millipore filter (Merck KGaA, Germany). Filtrates were stored at 4 °C and analyzed within 24 hours to minimize degradation. To ensure reproducibility, all extractions were performed in triplicate.

Determination of Total Phenolic Content (TPC)

To establish the correlation between phenolic moieties and radical scavenging efficacy (Results 4.5.1), the quantification of total phenolic content served as the primary chemical screen. The total phenolic content was quantified using the Folin-Ciocalteu method [116]. The principle of this assay depends on the transfer of electrons from phenolic compounds to phosphomolybdic or phosphotungstic acid complexes in an alkaline medium, resulting in the formation of a blue chromophore. Briefly, 0.05 mL of the aqueous extract was mixed with 0.5 mL of 0.2 N Folin-Ciocalteu reagent. The mixture was vortexed for 1 min and incubated for 5 min at room temperature. Subsequently, 0.4 mL of 1 M sodium carbonate (Na_2CO_3) was added. The reaction mixture was incubated in the dark for 15 min to prevent photodegradation, after which the absorbance was measured at 765 nm using a Hitachi 556 spectrophotometer. A standard curve was constructed using chlorogenic acid (0-250 μg/mL, R^2 = 0.995), and results were expressed as μg chlorogenic acid equivalents per mL of extract.

Ferric Reducing Antioxidant Power (FRAP) Assay

The total antioxidant capacity was assessed using the FRAP assay [117], which measures the reduction of a ferric-tripyridyltriazine complex to its ferrous form. From a mechanistic perspective, this assay evaluates the electron-donating potential of the antioxidants. At low pH, the reduction of the colorless Fe^{3+}-TPTZ complex to the intense blue Fe^{2+}-TPTZ form is directly proportional to the reducing power of the sample. The FRAP working reagent was prepared by mixing 2.5 mL of ferric chloride ($FeCl_3 \cdot 6H_2O$) solution, 25 mL of acetate buffer (pH 3.6), and 2.5 mL of TPTZ solution (10 mM TPTZ in 40 mM HCl). For the assay, 25 μL of aqueous extract was mixed with 175 μL of distilled water and 1.5 mL of the FRAP reagent. The mixture was incubated at 37 °C for 10 min. The absorbance of the resulting blue-colored Fe^{2+}-TPTZ complex was measured at 593 nm. FRAP values were presented as μmol Fe^{2+} equivalents per liter of sample. To substantiate the chemical basis of this activity, a regression analysis was performed to correlate FRAP values with TPC data.

Lipid Peroxidation Assay (MDA Quantification)

While FRAP explores the chemical reducing potential, the biological functionality of KCNQ1 is intrinsically linked to the integrity of the lipid bilayer. Consequently, a lipid peroxidation model was selected to provide an complementary, biologically relevant evaluation of protection against oxidative damage (Results 4.5.3). Antioxidant activity against lipid peroxidation was evaluated by quantifying MDA via the thiobarbituric acid (TBA) reaction [199-201]. This assay is based on the condensation of two molecules of TBA with one molecule of MDA under high temperature and acidic conditions, producing a pink trimethine complex. Oxidative stress was induced in human blood plasma (Sigma-Aldrich, St. Louis, MO, USA) using Fenton reagents. As the plasma was procured from a certified commercial source without identifiable human data, institutional ethical approval was waived in accordance with standard research guidelines. The reaction mixture consisted of 100 µL plasma, 50 µL of test sample (or water for control), 15 µL of 0.88 M hydrogen peroxide (H_2O_2), and 15 µL of 1 mM ferrous sulfate ($FeSO_4$). The mixture was incubated at 37 °C for 1 h. Following incubation, TBA reagent was added to quantify thiobarbituric acid reactive substances (TBARS). Since TBARS largely reflect MDA but are not fully specific, absorbance at 532 nm was used as an operational indicator for lipid peroxidation in our assay conditions. Antioxidant activity was inversely proportional to the concentration of MDA formed, expressed as nmol MDA/mL plasma. This assay specifically evaluated the efficacy of the extracts in preserving membrane lipid integrity, a critical component of the indirect protective mechanism. Specifically, this assay was selected because KCNQ1 is an integral membrane protein; therefore, preserving the integrity of the lipid bilayer against peroxidation is critical for maintaining the channel's structural stability and gating kinetics.

3.2.4 Statistical Analysis

Experimental data (FRAP, TPC, MDA) are presented as median ± interquartile range (n=3). Differences were assessed using the Kruskal-Wallis test followed by Dunn's post-hoc test ($p < 0.05$) via GraphPad Prism 8.1. To assess the relationship between phenolic content and antioxidant capacity, correlation analysis was performed. For MD simulations, analyses were performed on the stable equilibrium phase of the trajectories. Structural stability and convergence were verified via time-dependent RMSD profiles.

4. Results and Discussion

4.1 Dual Regulatory Effects of Mallotoxin on the KCNQ1-KCNE Complex

4.1.1 Structural Insights and Electrostatic Characteristics

The homology model of the KCNQ1-KCNE1 complex was built using the high-resolution cryo-EM structure of KCNQ1-KCNE3 (PDB ID: 6V01) as a template. The model was supported by sequence similarity within the KCNE transmembrane helix and conserved membrane-embedded structure, as the transmembrane segment is a key determinant of KCNE positioning within the membrane. While the sequence identity of 28% (Figure 17A) is situated within the uncertain region of homology inference of homology modeling, the structural conservation of the voltage-gated ion channel superfamily serves as a more reliable determinant of the 3D fold than sequence similarity, particularly in the transmembrane core. Consequently, the model quality was assessed based on the preservation of the canonical transmembrane helical arrangement and hydrophobic packing, rather than merely relying on sequence alignment. This assessment was supplemented by Ramachandran plot analysis (PROCHECK) [188] for stereochemical quality. Importantly, the fraction of residues in disallowed regions did not increase relative to the cryo-EM template (11 residues; 0.54%), indicating that the KCNE3 to KCNE1 substitutions did not introduce additional backbone outliers during model building. Therefore, the model provides a reasonable structural basis for comparative analyses of KCNE-dependent electrostatic features.

ESP maps computed using the same visualization scale and solver settings revealed a significant difference between the two complexes: the KCNQ1-KCNE3 complex exhibited a distinct central region of positive ESP (blue isosurfaces in Figure 17C), absent in the KCNQ1-KCNE1 complex (Figure 17D). This ESP disparity is consistent with the charge difference between the corresponding KCNE residues (KCNE1 74-75: HS; KCNE3 87-88: KR), shown in Figure 17A, and is additionally determined by neighboring channel residues and the PIP_2 lipids. Notably, our modeling protocol incorporated two PIP_2 molecules per KCNQ1 subunit (eight per tetramer). While earlier models often considered a single canonical PIP_2 site, work published after completion of this study [47] support the presence of a second PIP_2-binding site per protomer in activated conformations. This later evidence provides independent support for our inclusion of two PIP_2 molecules per subunit when evaluating KCNE-dependent electrostatic landscapes, suggesting a KCNE-dependent electrostatic environment that may contribute to the distinct MTX responses observed for the two complexes.

A

```
        39         50        60        70      78
hKCNE1   DGKLEALYVLMVLGFFGFFTLGIMLSYIRSKKLEHSNDPF
hKCNE3   RDDNSYMYILFVMFLFAVTVGSLILGYTRSRKVDKRSDPY
        53     60        70        80          92
         : :   :*:*.*: :*.    .::*.* **:* :.  **:
```

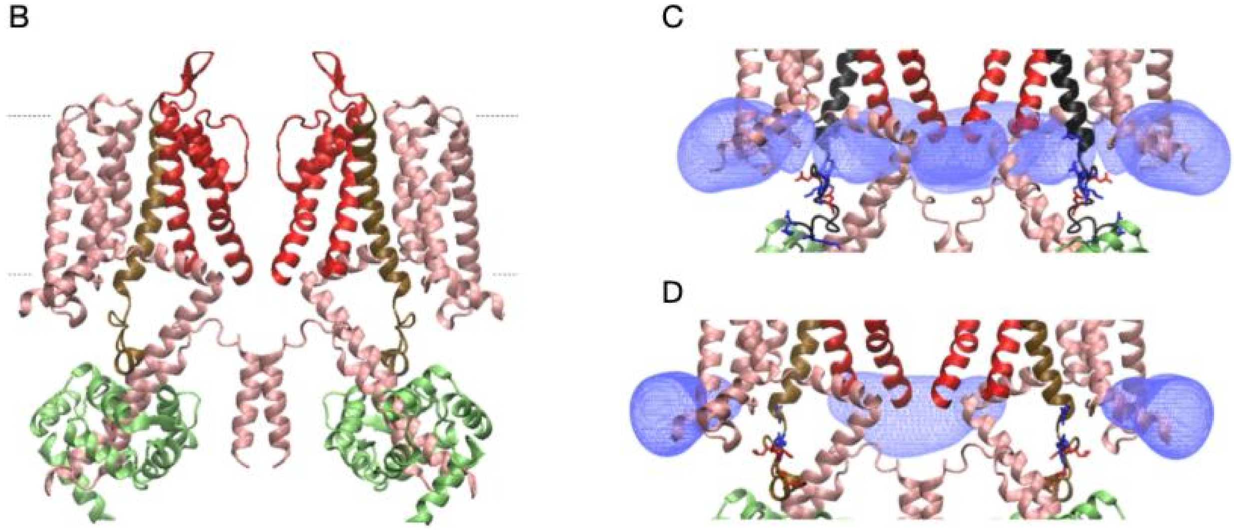

Figure 17. Human KCNE1-KCNE3 sequence alignment, structural models, and electrostatic potential maps of KCNQ1-KCNE1/3 complexes with two PIP_2 molecules per subunit (eight per tetramer) (side view, PIP_2 molecules not shown). Protein chains shown in ribbon presentation: KCNQ1 chains A and C shown in pink, chains B and D are shown in red, KCNE1/3 chains are shown in brown/black, CaM chains shown in green. Blue isosurfaces correspond to regions of high positive electrostatic potential generated by protein and PIP_2 molecules at an interface of the transmembrane and cytoplasmic domain. Charged residues of a KCNEx S2-S3 linker are shown in rod presentation (Arg/Lys in blue, Asp/Glu in red). (A) Fragment of sequence alignment (positively charged residues shown in blue, negatively charged in red). (B) General view of the KCNQ1-KCNE1 complex. (C) KCNQ1-KCNE3 complex (key positively and negatively charged residues shown with blue and red rods, respectively). (D) KCNQ1-KCNE1 complex

4.1.2 Molecular Mechanisms of Dual Modulation

Molecular docking studies explored the interaction mode of MTX with the KCNQ1-KCNE complexes. In the KCNQ1-KCNE1 complex, MTX was predicted to bind at a more peripheral site. This binding mode is compatible with an allosteric mechanism that may preferentially stabilize an open conformation, thereby increasing channel activity (shown in Figure 18A, C). Conversely, in the KCNQ1-KCNE3 complex, MTX was predicted to engage a central, positively charged region (primarily involving Arg360 residues in KCNQ1), consistent with a binding pose that occludes the pore and the experimentally observed inhibitory effect (Figure 18B, D). This suggests a dual modulatory mechanism driven by distinct electrostatic interactions.

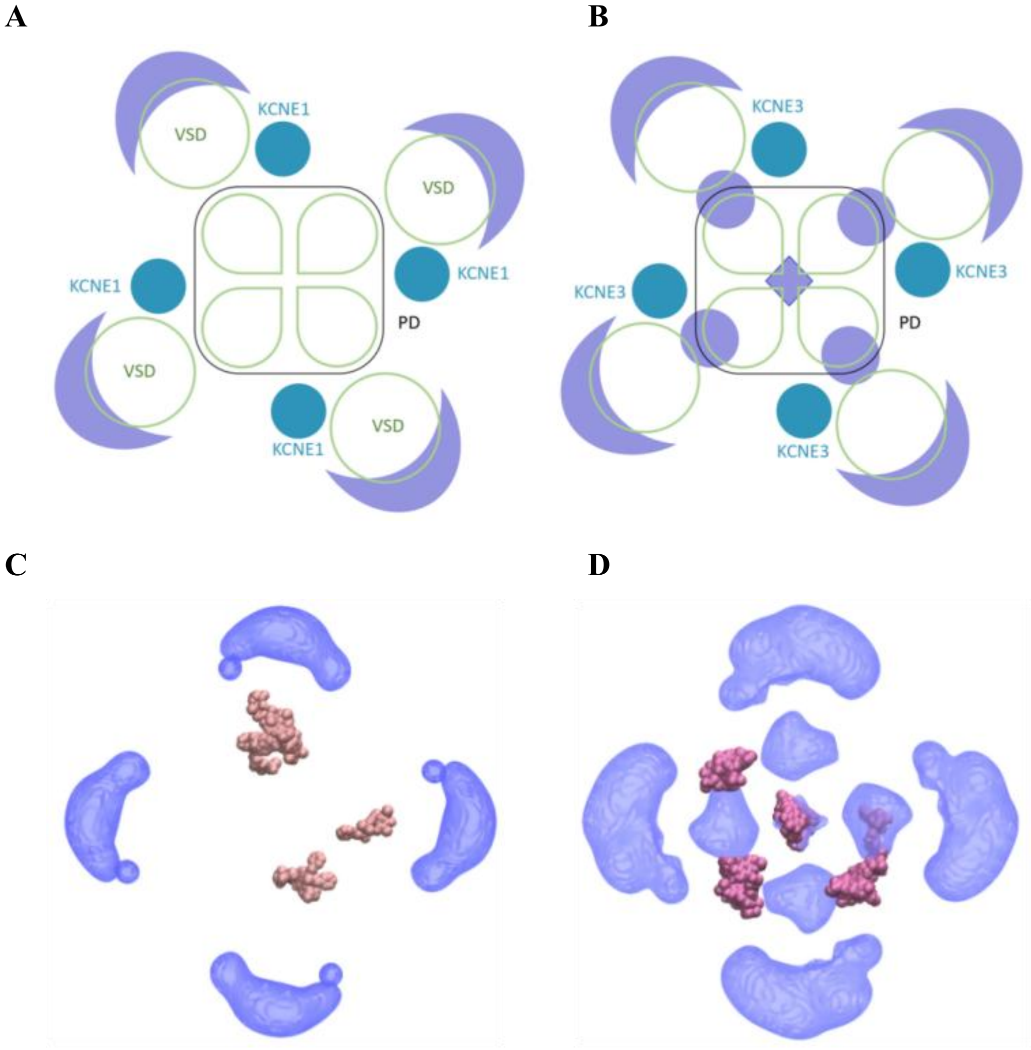

Figure 18. Docking results of MTX and electrostatic potential maps of KCNQ1-KCNE1 and KCNQ1-KCNE3 complexes with two PIP_2 molecules per subunit (eight per tetramer) (top view; PIP_2 molecules not shown). (A, B) Schematic representations of the complexes (A) KCNQ1/KCNE1 and (B) KCNQ1/KCNE3. KCNQ1 subunits are shown in green, while KCNE1 and KCNE3 subunits are shown in blue. Purple isosurfaces represent regions with high positive electrostatic potential located on the intracellular side of the transmembrane domain of the complexes. (C, D) Docking results of MTX and high-ESP regions of the KCNQ1/KCNEx complex (extracellular view). (C) Results for the KCNQ1/KCNE1 complex. All solutions are located at the periphery of the pore domain. (D) Results for the KCNQ1/KCNE3 complex. One of the docking solutions is located at the center of the pore domain, blocking ion current.

In silico modeling reveals differences between KCNQ1-KCNE1 and KCNQ1-KCNE3 complexes in their inner cavity electrostatic environments. These KCNE-dependent differences may reveal opposite functional outcomes of MTX: activation of KCNQ1-KCNE1 versus inhibition of KCNQ1-KCNE3, by changing the electrostatic environment and accessible poses within the inner cavity. Thus, the electrostatic landscape of the channel pore emerges as a key factor to explore MTX binding specificity.

Structural analysis identified a unique region of positive ESP within the central cavity of KCNQ1-KCNE3, which is absent in KCNQ1-KCNE1. This finding provides a plausible explanation for the mechanism of MTX-mediated inhibition on the KCNQ1-KCNE3 channel. This putative inhibitory mode is conceptually analogous to central-cavity occupancy observed for other pore-blocking ligands (e.g., linopirdine in KCNQ4; PDB ID: 7BYN) [30], where the ligand occupies a central binding site to block ion flux. The absence of the corresponding positive region in the KCNQ1-KCNE1 may help explain why MTX does not display similar inhibitory effects on this complex. The hypothesis is further supported by the structural difference at the "Site 2" interface described by Cui et al. [47], which was published after the completion of the present work and is incorporated here. They observed that KCNE3 contributes to a looser packing with lower PIP_2 affinity at this interface compared to the tighter, high-affinity interaction mediated by KCNE1. This looser structural arrangement in KCNQ1-KCNE3 likely creates a more accessible cavity space, thereby facilitating the entry of the anionic MTX molecule into the central pore-occluding position we identified. In contrast, the tighter packing and enhanced PIP_2 occupancy in KCNQ1-KCNE1 would sterically hinder central access, leading the ligand to adopt the peripheral activating site.

Molecular docking analyses have indicated an alternative mechanism underlying MTX enhancement of KCNQ1-KCNE1 channel activity. The predicted binding mode suggests that MTX interacts with specific residues in a pattern compatible with stabilization of an open channel conformation, potentially facilitating enhanced ion conductance. This observation is consistent with previous experimental findings that demonstrate increased KCNQ1-KCNE1 currents in the presence of MTX. As MTX binding is expected to be sensitive to the electrostatic landscape of the cavity, our models explicitly included PIP_2 molecules to better capture lipid-dependent electrostatic fields and steric constraints that may modulate MTX binding modes. Specifically, two PIP_2 molecules were included per KCNQ1 subunit (eight PIP_2 molecules per tetramer). PIP_2 incorporation represents a critical aspect of our modeling approach, as PIP_2 is known to be crucial for modulating the function of the KCNQ1 channel. While commonly used KCNQ1 cryo-EM structures typically resolve the canonical PIP_2 site, a second putative PIP_2 interaction site has been suggested in the literature [202, 203], which has been further supported by evidence in the electron density map of the structure (PDB

ID: 6V01) in this study. Accordingly, both sites were occupied in each subunit in our models, which enhances the physiological relevance of our findings. These negatively charged lipids affect the overall electrostatic landscape, potentially influencing MTX binding modes. The presence of PIP_2 may create additional electrostatic gradients that influence the binding affinity and specificity of MTX for different channel complexes, suggesting that protein-lipid interactions play a crucial role in determining the pharmacological properties of KCNQ1 channel modulators.

These results may have important implications for the therapeutic development targeting KCNQ1 channel complexes. By providing a structural basis for dual modulatory effects of MTX, our analysis may help guide the rational design of complex-specific modulators that preferentially target either the KCNE3-associated cavity region or the KCNE1-associated peripheral site. Such compounds could be engineered to selectively target either the inhibitory binding site in KCNQ1-KCNE3 or the activating site in KCNQ1-KCNE1, resulting in more specific therapeutic treatments for various channelopathies, such as LQT syndrome. However, several limitations of this study should be considered. Although the homology model of the KCNQ1-KCNE1 complex is derived from high-resolution cryo-EM data of KCNQ1-KCNE3, experimental validation of the predicted structures and binding modes would enhance the reliability of our findings. Furthermore, the dynamic nature of channel-MTX interactions, including potential conformational changes upon binding, requires further exploration through longer time-scale MD simulations to capture transient states and binding affinities.

The analysis of dual modulatory effects of MTX highlighted the importance of electrostatic features and auxiliary subunit identity in determining ligand-channel interactions. However, a comprehensive understanding of KCNQ1 regulation requires not only characterization of ligand binding sites but also elucidation of structurally unresolved regions that mediate critical regulatory functions. Among these, the HC-HD linker within the C-terminal domain remains poorly defined in available cryo-EM structures, despite its established importance for Yotiao binding and PKA-mediated phosphorylation. The following section addresses this structural gap through density-guided molecular modeling.

4.2 Structural Modeling of the KCNQ1 Helix C-Helix D Linker

Cryo-EM has substantially advanced the structural characterization of KCNQ1. However, the C-terminal HC-HD segment remains consistently unresolved in all available tetrameric structures. While a structure of the isolated HD was solved previously using X-ray crystallography [9], published structures of the full tetrameric KCNQ1 channel have failed to resolve the complete HC-HD region, largely due to the inherent flexibility of the connecting linker [7, 10, 13-15], as illustrated in Figure 19.

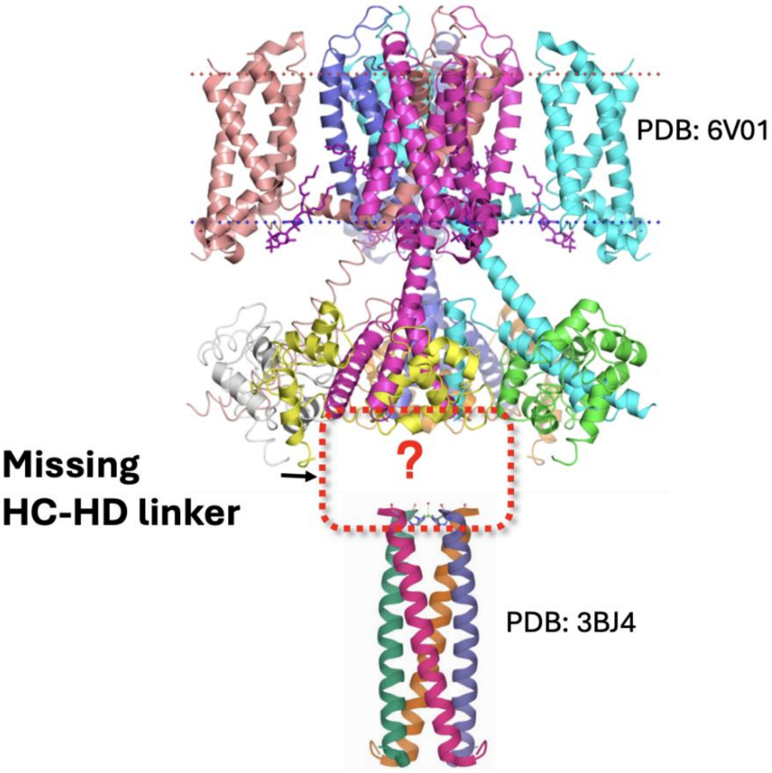

Figure 19. Structural gap in the KCNQ1 complex due to the unresolved HC-HD linker. The upper portion displays the Cryo-EM structure of the transmembrane domain and the proximal C-terminus (Helix C), derived from PDB: 6V01. The lower portion shows the X-ray crystal structure of the isolated distal C-terminal assembly domain (Helix D), derived from PDB: 3BJ4. The red dashed box highlights the unresolved HC-HD linker, a region characterized by high intrinsic flexibility that creates a structural discontinuity between the pore and tetramerization domains.

This structural incompleteness poses a significant limitation to fully understand KCNQ1 function and regulation, as the C-terminal domain has been involved in channel assembly, trafficking, and modulation by regulatory proteins. To resolve this critical structural unknown, this study used an integrated combination of high-resolution cryo-EM density data (EMD-20966) and density-guided molecular modelling. Using these complementary inputs, we constructed an atomic, density-consistent model including HC, the HC-HD linker, and the majority of HD. The resulting model extends the C-terminal domain beyond previously published atomic structures and supports evaluation of a domain-swapped topology as a plausible configuration. This domain-swapped architecture could provide a structural architecture for Yotiao-dependent macromolecular complex assembly in the distal C-terminal domain.

4.2.1 Initial Modeling Challenges and the Domain-Swapping Hypothesis

After fitting the initial structural model predicted by AlphaFold into the cryo-EM density map (EMD-20966), a critical discrepancy was observed. The predicted linker conformation (Figure 20A, red dashed box) lacked corresponding continuous density and appeared incompatible with the tetrameric assembly. These observations motivated exploration of alternative HC-HD topologies. Therefore, we propose a novel "domain-swapped" architecture hypothesis where the HC of one subunit bypasses its own HD and instead forms a connection to the HD of an adjacent subunit (Figure 20B, schematic with green and purple subunits). This type of domain swapping has not been reported in KCNQ1, but related structural arrangement have been discussed previously, and domain-swapped features have been described in other proteins (e.g., PDB IDs: 1I4M, 7DNS, 3HJ5; Figure 20C) [204, 205]. These motifs are often associated with increased oligomer stability and functional regulation, lending biological plausibility to our model.

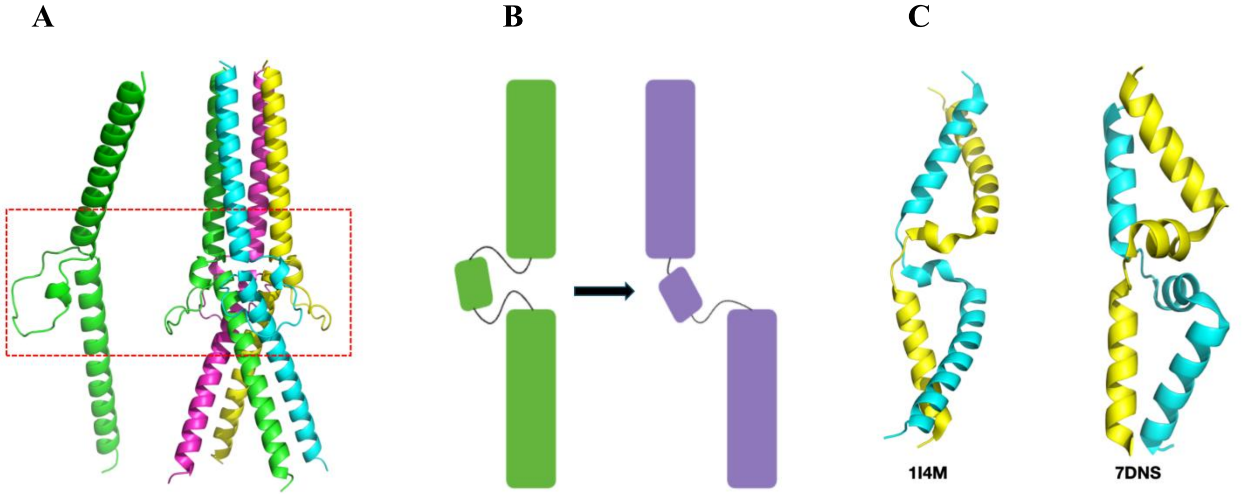

Figure 20. Initial modeling and hypothesis of a domain-swapped linker in KCNQ1. (A) The initial structural model of the HC-HD region as predicted by AlphaFold, displayed as both an individual monomer and the assembled tetramer. The red dashed box highlights the linker region within the tetrameric assembly, where the predicted conformation does not match the observed cryo-EM density, suggesting an alternative arrangement. (B) Schematic of the **proposed domain-swapped topology**. This model posits that Helix C (HC, green) **bypasses its intra-subunit connection** to Helix D (HD, green) and instead "swaps" to connect with the HD of an adjacent subunit (purple). (C) Examples of experimentally confirmed domain-swapped dimers from the Protein Data Bank (PDB IDs: 1I4M, 7DNS, 3HJ5). These known structures illustrate that domain swapping is a feasible and observed structural motif in other proteins, providing contextual support for our hypothesis.

4.2.2 Model Construction and Validation

Consequently, to construct a model that fits the density map, we made two key modifications. First, comparing with known HD structure, determined previously (PDB ID 3BJ4 [9]), our HD model is extended approximately two helical turns longer (residues 581-620 vs. 588-620), based on elongated, helical density characteristics. This extension correspondingly shortens the linker (residues 567-580) and leads to improved agreement with the electron density. Second, examination of the electron density map surrounding the HC-HD linker revealed a topology inconsistent with a canonical intra-subunit connection, encouraging the exploration of a domain-swapped arrangement. The most continuous density connectivity in this region was more indicative of inter-subunit rather than intra-subunit linkage. Specifically, this linker follows a pattern where the HC of one subunit is followed by the HD of the adjacent subunit, and this sequential offset continues cyclically around the channel. Notably, compared with a non-swapped connectivity model built and refined under the same fitting procedure and map visualization settings, the domain-swapped topology showed more continuous linker density and fewer obvious steric inconsistencies. Visual evaluation of density continuity and less steric clashes after refinement supported the plausibility of the swapped assignment. Accordingly, we propose a structural hypothesis featuring a prolonged HD domain connected via a domain-swapped linker (Figure 21A, B). Given the intrinsic flexibility of this region and the locally weaker density observed around the linker (suggesting lower local resolution), this assignment should be interpreted cautiously as a computational derived model. While consistent with the current density map, definitive confirmation of this domain-swapped topology requires orthogonal structural methods, particularly cross-linking mass spectrometry (XL-MS), to clearly map the inter-subunit connectivity.

This domain-swapped model offers a plausible structural interpretation consistent with the low-resolution regions of the cryo-EM density (EMD-20966) and reported biochemical annotations, including good consistency of residues 581-588 of HD with the available electron density map (EMD-20966; Figure 21C). According to the databases like dbPTM [206] and previous experimental investigations [207], residues S571 and S577 in the HC-HD linker can be phosphorylated. This biological modification requires that these residues be exposed to the aqueous cytoplasmic environment, which is consistent with our model where both residues are situated on the solvent-accessible surface (Figure 21C, bottom). This supports their potential accessibility to kinases. It is also possible that solvent exposure could facilitate interactions with cytosolic regulators; more importantly, solvent accessibility is essential for kinase access and phosphorylation, with potential downstream consequences for ion channel regulation. Furthermore, this solvent exposure may facilitate dynamic regulatory interactions with cytosolic binding partners, such as CaM, enhancing the relevance of this model to the KCNQ1 physiological function.

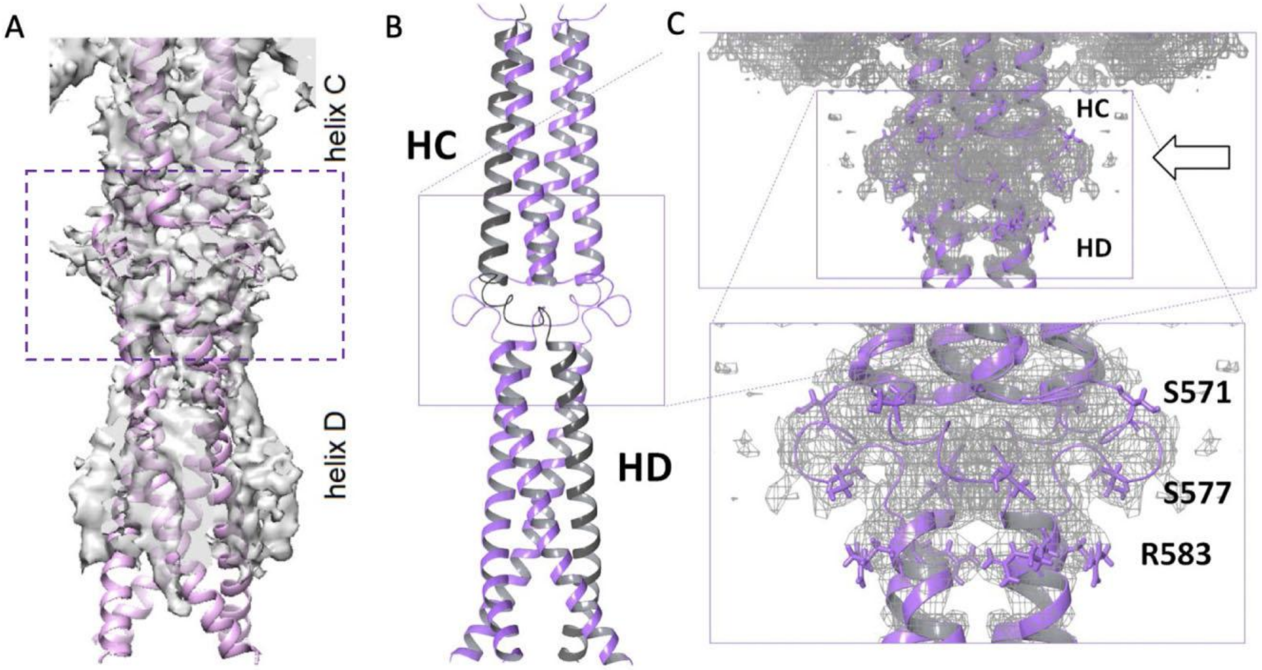

Figure 21. The refined domain-swapped model of the KCNQ1 HC-HD region. (A) The atomic model of helices C and D, fitted to the electron density map (EMD-20966) used in this study. The unstructured, domain-swapped linker is highlighted by a dashed rectangle. (B) A view of the model illustrating the clear domain swap, with one subunit highlighted in black for clarity. (C) Fitting the model into the electron density map (gray mesh) shows that the phosphorylation sites S571 and S577 are fully solvent-exposed to the solvent on the cytoplasmic surface.

It is important to emphasize that this domain-swapped architecture represents a computational structural hypothesis derived from current cryo-EM constraints. While it offers a plausible resolution to the density discontinuity, it serves primarily as a structural architecture to guide future functional validation, such as orthogonal structural methods (e.g., XL-MS or mutagenesis), to prove its biological significance. This is particularly relevant given that previous computational studies have established that the entire protein structure, not limited to the transmembrane pore, critically contributes to energy landscape of the channel and its subconductance states [208]. By resolving the atomic connectivity of the HC-HD linker, our model adds structural detail to complement these prior predictions, bridging a key gap in these structure-function relationships, thereby providing a more complete structural basis for understanding how distal C-terminal dynamics may propagate to influence pore gating.

With a structural model now proposed for the previously unresolved HC-HD linker, we next turned our attention to understanding how pathogenic mutations within the voltage-sensing domain affect KCNQ1 function. While the preceding sections focused on WT channel structure and its modulation by external factors, the next section addresses inherited variants that can cause KCNQ1 dysfunction in clinical cases.

4.3 Effects of Pathogenic Mutations on the KCNQ1-KCNE3-PIP$_2$ Complex

This section examines the molecular basis for LQT1-associated mutations: D242N and R243H. These specific variants were specifically selected due to their characterized association with severe cardiac phenotypes and their critical localization within the VSD S4. Both mutations may alter the local electrostatic environment at the cytoplasmic VSD interface, a region involved in coupling to the pore and in regulation by anionic lipids such as PIP$_2$. As displayed in Figure 10, these two mutations locate at the cytoplasmic end of the S4 voltage-sensing helix and the beginning of the S4-S5 linker. We postulated that the sites of D242 or R243 act as a critical coupling node for VSD-pore coupling and lipid regulation. Consequently, mutations that alter the charge and steric properties at this vital point are expected to perturb the conformational stability and local dynamics of the channel.

To investigate the atomic-level consequences of these pathogenic substitutions, we employed comprehensive all-atom MD simulations based on the high-resolution cryo-EM structure of the KCNQ1-KCNE3-PIP$_2$ complex (PDB ID: 6V01). Using this physiologically relevant system allows for assessment of how single-point mutations intrinsically perturb the conformational landscape of KCNQ1.

4.3.1 Analysis of Structural Stability and Flexibility

The RMSD values of Cα atoms were calculated for WT KCNQ1 (KCNQ1-WT) and mutant KCNQ1 (Figure 22A). This analysis revealed the structural stability and conformational changes of the proteins over the course of MD simulations. Cα RMSD of these complexes displayed similar behavior and reached a structural plateau relative to the initial cryo-EM conformation within the simulated timescale, in which the RMSD values of KCNQ1-WT, KCNQ1-D242N and KCNQ1-R243H were ~0.3 nm, ~0.31 nm and ~0.32 nm, respectively. While the global backbone deviations are comparable across systems, the R243H variant exhibits a subtle but consistent trend toward higher structural drift. However, global RMSD analysis may blur specific local perturbations. Mechanistically, the potential destabilization in R243H is more clearly revealed by residue-specific fluctuation analyses (see RMSF below), which suggest that the substitution of the bulky, positively charged Arginine side chain with the smaller, titratable Histidine imidazole ring disrupts critical local salt-bridge networks. This likely destabilizes the dense steric packing within the VSD, thereby introducing a higher degree of entropic freedom and structural fluidity compared to the WT channel.

The radius of gyration (Rg) analysis for the WT KCNQ1 and mutant KCNQ1 reveals distinct differences in their structural compactness (Figure 22B). The KCNQ1-WT and KCNQ1-D242N exhibit similar trends for Rg values and then maintain stable Rg values around 3.40 nm at 20 ns, suggesting maintained structural compactness and stability. In contrast, the KCNQ1-R243H variant shows observably higher Rg values, stabilizing around 3.45 nm after an initial adjustment period of approximately 30 ns, indicating a trend towards structural relaxation rather than global structural disruption. This increase in Rg likely reflects a loosening of the local packing within the VSD-PD interface. Thermodynamically, the increased mobility observed in R243H implies weakened coupling elasticity and less efficient transduction of voltage-sensor conformational changes into pore-gating transitions. This represents an early-stage conformational drift driven by the loss of the critical Arg243 interaction, which could impact voltage-sensing efficiency, although functional consequences require experimental confirmation. These findings reveal that the R243H mutation may be associated with the protein's overall structural compactness, potentially impacting its functional stability, while the D242N mutation maintains relatively similar compactness to the WT protein.

The SASA analysis for the KCNQ1 protein reveals distinct differences in surface exposure (Figure 22C). The WT KCNQ1 persistently maintains the lowest SASA values around 510-520 nm^2, showing a more compact and stable structure. In contrast, the KCNQ1-R243H shows the highest SASA values, stabilizing around 540-550 nm^2 after an initial increase, suggesting a less compact and more solvent-accessible structure. The KCNQ1-D242N variant exhibits intermediate SASA values around 520-530 nm^2, illustrating relatively moderate surface exposure. These results imply that the R243H mutation markedly increases the surface exposure of KCNQ1, potentially affecting its structural stability, while the D242N mutation results in moderate changes compared to the WT.

RMSF was calculated to gain insight into the effects of certain amino acid residues on both WT and mutant KCNQ1 complexes. Through RMSF analysis, we can explore the local flexibility and mobility of specific residues within the protein structure, providing an understanding of the dynamic behavior of the complex at the amino acid level. The RMSF analyses were performed on the backbone atoms of KCNQ1 chain A as a representative subunit (Figure 22D). Similar trends were observed in other subunits. Because KCNQ1 is a homotetramer with near four-fold symmetry in the starting structure, we additionally verified that the corresponding trends were comparable across chains A-D for the analysis reported here (RMSD/Rg/SASA and interaction statistics), supporting the use of one chain for clarity of presentation. The results revealed that the three structures show similar fluctuation patterns, in which greater fluctuations are found in KCNQ1-D242N between residues ranging from 180 to 244 (residues from 219 to 224 are missing in the initial cryo-EM resolved structure), revealing that the mutation D242N causes more internal dynamics in this region. WT KCNQ1 generally exhibits lower fluctuations, reflecting higher stability, compared to the mutant KCNQ1. Notable peaks are observed at residues near 289, as they are in the loop region on the extracellular side which is rather unstable. Apart from residues near 104 (N-terminal), 356 (C-terminal) and 289 (loop), most of the fluctuations result from the VSD and S4-S5 linker (residues from 104 to 258), while the RMSF value of the PD (residues from 259 to 356) remain relatively low, suggesting that the PD maintains a more stable conformation.

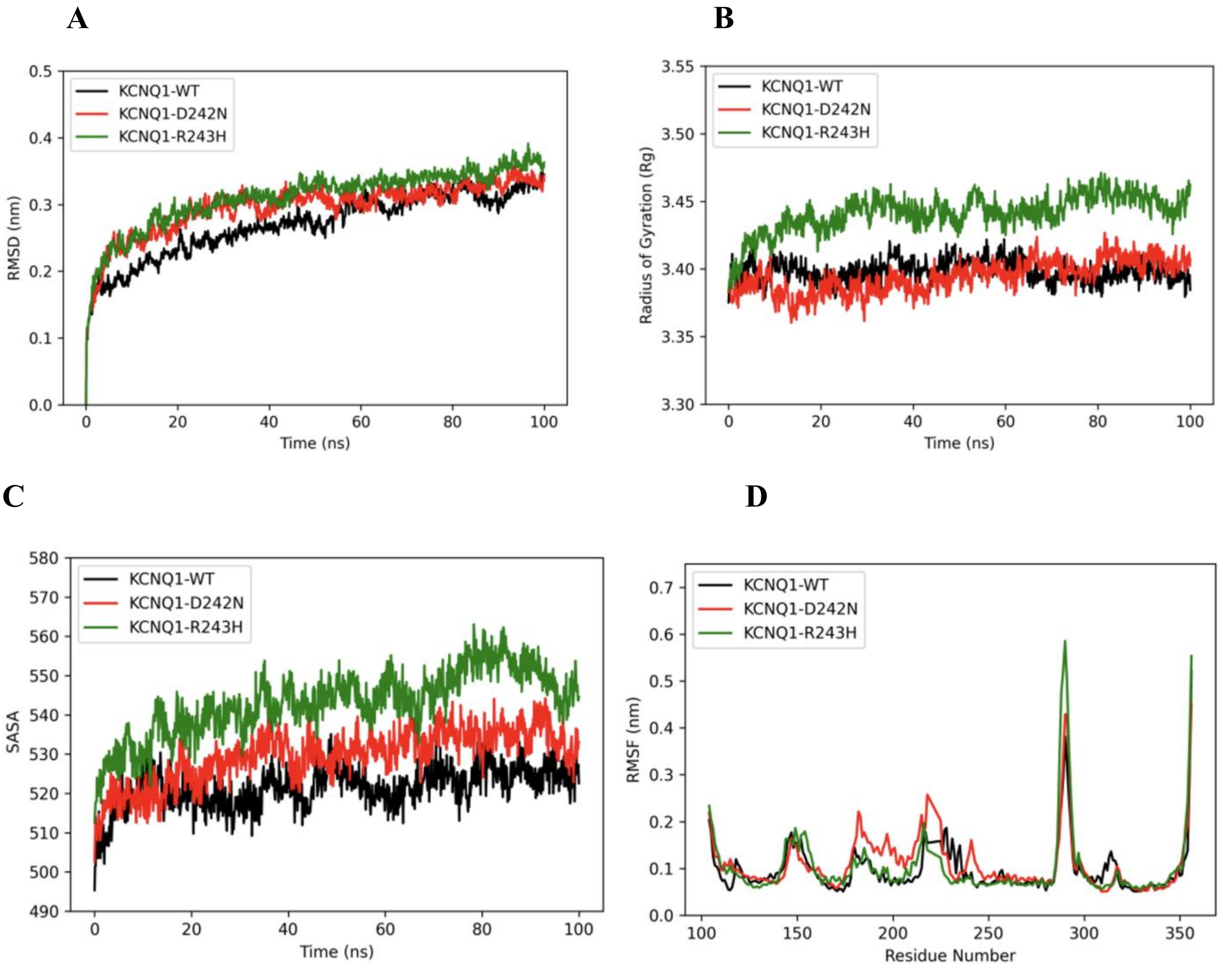

Figure 22. Comparative analysis of wild-type(WT) and mutant KCNQ1 structural dynamics and interactions. (A) Root Mean Square Deviation (RMSD) of Cα atoms of KCNQ1. (B) Radius of gyration (Rg) plot. (C) Solvent Accessible Surface Area (SASA) plot. (D) Root Mean Square Fluctuation (RMSF) plot of the backbone of KCNQ1 chain A.

4.3.2 Intermolecular Interaction Network: Hydrogen Bonds and PIP_2 Contacts

Hydrogen Bond Analysis of KCNQ1 Interactions with KCNE3 and PIP_2

Analysis of hydrogen bonds at the KCNQ1-KCNE3 interface (Figure 23A) demonstrates that WT KCNQ1-KCNE3 maintains consistently higher hydrogen bond numbers, consistent with a stable interface throughout the MD simulation. In contrast, both D242N and R243H mutations exhibit increased hydrogen bond fluctuations and variability, with R243H showing the greatest perturbation. Accordingly, these findings indicate that D242N and R243H mutations destabilize the KCNQ1-KCNE3 hydrogen bonding network, thereby compromising interface stability. This increased variability suggests that while the interface is not completely disrupted, the dynamic equilibrium of the hydrogen bonding network is significantly perturbed in the pathogenic variants.

The increased variability in hydrogen bonds for the mutants highlights their potential impact on the structural integrity and function of the protein. Figure 23B displays the dynamics of hydrogen bond formation between KCNQ1 and PIP$_2$. The KCNQ1-PIP$_2$-WT and KCNQ1-PIP$_2$-D242N complexes maintained a similar number of hydrogen bonds, about 44 bonds in the last 20 ns of simulation, when counting hydrogen bonds between KCNQ1 chain A and PIP$_2$ (representative subunit; comparable trends were observed across other chains). In contrast, the KCNQ1-PIP$_2$-R243H exhibited lower number of hydrogen bonds during this period. These findings highlight the different impact of the D242N and R243H mutations on the hydrogen bonding network within the KCNQ1-PIP$_2$ complex.

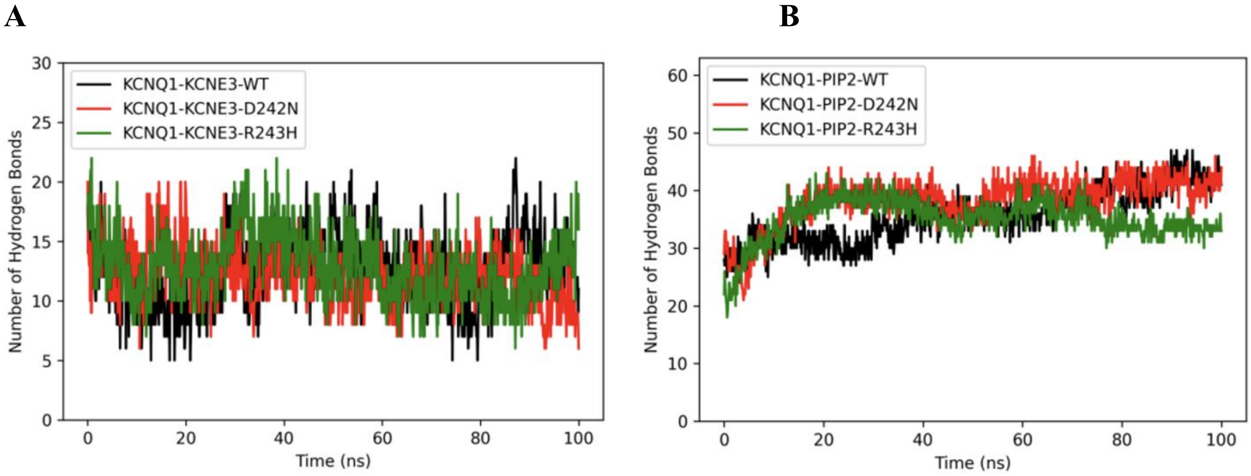

Figure 23. Hydrogen bonds analysis of wild-type(WT) and mutant KCNQ1 structural dynamics and interactions. (A) Hydrogen bonds formed between KCNQ1 and KCNE3. (B) Hydrogen bonds formed between KCNQ1 and PIP$_2$. Hydrogen bonds in (A) and (B) were identified using a donor-acceptor distance criterion of less than 3.5 Å and a donor-hydrogen-acceptor angle greater than 120°.

The hydrogen bond occupancies higher than 30% are summarized in Table 3. Importantly, cumulative occupancy values exceeded 100% for certain basic residues, reflecting their capacity to form multiple simultaneous hydrogen bonds with the polyanionic PIP$_2$ headgroup within a single simulation frame.

For WT KCNQ1-KCNE3, the interaction between KCNE3-TYR60-Side and KCNQ1-SER330-Side (shown in Figure 24) is consistently high across all chains, highlighting the key residue involved in upholding structural integrity. Interestingly, the detailed examination of the hydrogen bond occupancy (Table 3) reveals a complex perturbation pattern for the R243H mutant. While the global stability of the KCNQ1 subunit is compromised (as evidenced by increased RMSD in Section 4.3.1), this specific hydrogen bond exhibits unexpectedly higher occupancy in the R243H mutant (91%) compared to the WT (84%). This observation suggests a global local mismatch: although the mutation induces global destabilization (higher RMSD), it appears to constrain key interface residues within a locally rigidified hydrogen bond configuration that limits productive interfacial dynamics. This suggests that the pathogenicity of R243H may stem not just from structural loss-of-function, but from a loss of conformational entropy required for functional gating transitions. However, such abnormal local immobilization, alongside global destabilization, implies a loss of functional adaptability, potentially disrupting the flexible conformational transitions required for normal gating kinetics.

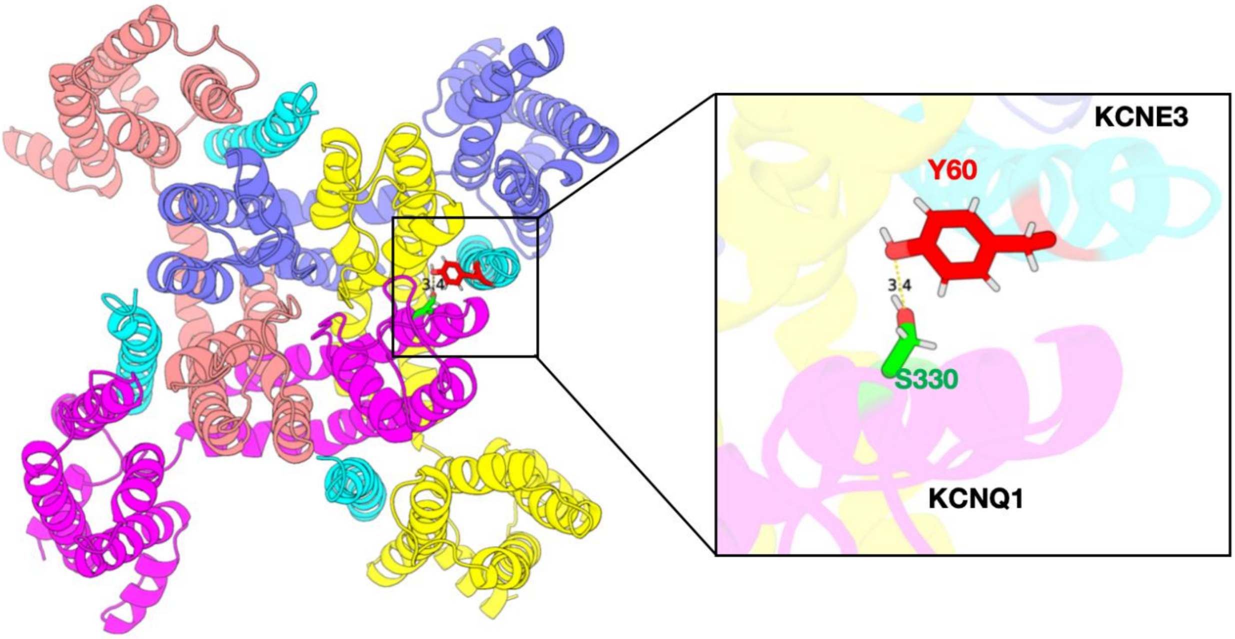

Figure 24. A stable hydrogen bond at the KCNQ1-KCNE3 interface identified through molecular dynamics simulations. The overall structure shows the KCNQ1 tetramer in a ribbon representation, with each subunit colored distinctly (blue, magenta, salmon, and yellow). The complexed KCNE3 accessory subunit is shown in cyan. (Inset) The magnified view details the specific interaction. Residues are shown in stick representation, with Serine 330 (S330) of KCNQ1 colored green and Tyrosine 60 (Y60) of KCNE3 colored red. The yellow dashed line indicates a stable hydrogen bond that was maintained throughout the simulation. The snapshot shown captures an interatomic distance of 3.4 Å.

Furthermore, the hydrogen bond occupancy analysis for KCNQ1 and PIP_2 in WT and variants (Table 3) reveals distinct intermolecular interaction profiles, which demonstrate different residue-level hydrogen-bonding preferences within the KCNQ1-PIP_2 complex. WT KCNQ1 shows high occupancy for KCNQ1-ARG181-Side with PIP_2, peaking at 188%. Hydrogen bond occupancy of ARG249-Side and LYS183-Side, also higher than 100%. This provides evidence for their active engagement in forming electrostatic interactions, specifically salt bridge interactions, with PIP_2. Consistent with the methodology described above, accumulative occupancies exceeding 100% were observed for key basic residues, reflecting their multi-contact interaction with the polyanionic PIP_2 headgroup. While a cryo-EM study identified that Arg249 interact with the negatively charged headgroup of PIP_2[14], in this study, this interaction was only observed in one of the analyzed chains. The discrepancy between each chain and PIP_2 may derive from the potentially dynamic nature of the KCNQ1-PIP_2 interactions, highlighting a potentially transient or metastable nature of these interactions.

Moreover, the D242N mutant exhibits even higher occupancy, notably 209% for ARG181-Side with PIP_2, indicating increased cumulative residue-PIP_2 hydrogen-bonding propensity in this trajectory. Conversely, the R243H mutant shows reduced and variable occupancy, with a maximum of 187% for ARG181-Side, suggesting a comparatively lower cumulative residue-PIP_2 hydrogen-bonding tendency than D242N.

Table 3. Hydrogen bond occupancy of wild-type and mutant KCNQ1-KCNE3-PIP_2 complex. Hydrogen bond occupancy data for the wild-type and mutant KCNQ1-KCNE3-PIP_2 complexes are presented below. Hydrogen bonds were identified using a donor-acceptor distance of <3.5 Å and a donor-hydrogen-acceptor angle of >120°. Occupancy exceed 100% implies that multiple hydrogen bonds occur simultaneously within the same frame. Only hydrogen bonds with an occupancy rate >30% are shown. Data from Chain A is selected as representative, and the overall interaction pattern was qualitatively similar across subunits.

Hydrogen Bond Occupancy Data			
Complex	**Donor**	**Acceptor**	**Occupancy (%)**
A. KCNQ1-KCNE3 Interface			
Wild-type	KCNE3-TYR60-Side	KCNQ1-SER330-Side	84
D242N	KCNE3-TYR60-Side	KCNQ1-SER330-Side	79
	KCNQ1-GLY119-Main	KCNE3-THR80-Main	31
R243H	KCNE3-TYR60-Side	KCNQ1-SER330-Side	91
	KCNE3-TYR79-Side	KCNQ1-ASP242-Side	30
B. KCNQ1-PIP_2 Interactions			
Wild-type	ARG181-Side	PIP_2	188
	ARG249-Side	PIP_2	183
	LYS183-Side	PIP_2	179
	LYS196-Side	PIP_2	84

	ARG116-Side	PIP_2	83
D242N	ARG181-Side	PIP_2	209
	ARG116-Side	PIP_2	160
	LYS183-Side	PIP_2	101
	TYR184-Side	PIP_2	88
	LYS196-Side	PIP_2	79
R243H	ARG181-Side	PIP_2	187
	LYS183-Side	PIP_2	182
	ARG192-Side	PIP_2	180
	ARG116-Side	PIP_2	174
	LYS196-Side	PIP_2	52
	ARG195-Side	PIP_2	50

Protein-PIP_2 Interactions

The last frames of 100 ns MD simulation were extracted to analyse the detailed interaction between KCNQ1 and PIP_2. The LigPlot diagrams describe the interactions between the KCNQ1 protein and the PIP_2 molecule (Figure 25), with a particular focus on hydrogen bonds and hydrophobic contacts.

As shown in Figure 25A for WT KCNQ1 and PIP_2, hydrogen bonds, represented by green dashed lines, involve key residues from one KCNQ1 subunit (identified as Chain E), including Arg181(E), Lys183(E), Arg195(E), Arg116(E), Lys196(E), and Arg249(E), with bond lengths spanning from 2.2 Å to 2.9 Å, implying strong electrostatic interactions. Additionally, hydrophobic interactions, denoted by red eyelash arcs, involve residues such as Pro197(E), Trp248(E), Gly245(E), and Arg249(E) from chain E, contributing significantly to the stabilization of the KCNQ1-PIP_2 complex.

Figure 25B illustrates the molecular interactions between KCNQ1-D242N and the PIP_2 molecule. Hydrogen bonds in this variant involve key residues from the adjacent chain E, such as Arg181(E), Lys183(E), Arg116(E), and Tyr111(E), with bond lengths ranging from 2.6 Å to 3.1 Å, indicating relatively strong electrostatic interactions but fewer bonds compared to WT. Hydrophobic interactions involve residues including Ile198(E), Pro197(E), Ile201(E), Trp248(E) and Arg249 from chain E.

Figure 25C diagram shows the molecular interactions between KCNQ1-R243H and the PIP_2 molecule. Key residues from chain E, such as Arg116(E), Arg181(E), Arg195(E), and Lys196(E), Lys183(E), and Arg249(E), form crucial hydrogen bonds with bond lengths ranging from 2.6Å to 3.0Å, emphasizing strong electrostatic interactions. Additionally, hydrophobic contacts involve residues like Pro197, Ile198, Arg239 and Trp248 which further stabilize the KCNQ1-PIP_2 complex. This intricate network of hydrogen bonds or electrostatic interactions and hydrophobic interactions underlines the importance of these residues in maintaining the KCNQ1-PIP_2 binding, with mutants showing altered interaction patterns that may contribute to channel dysfunction.

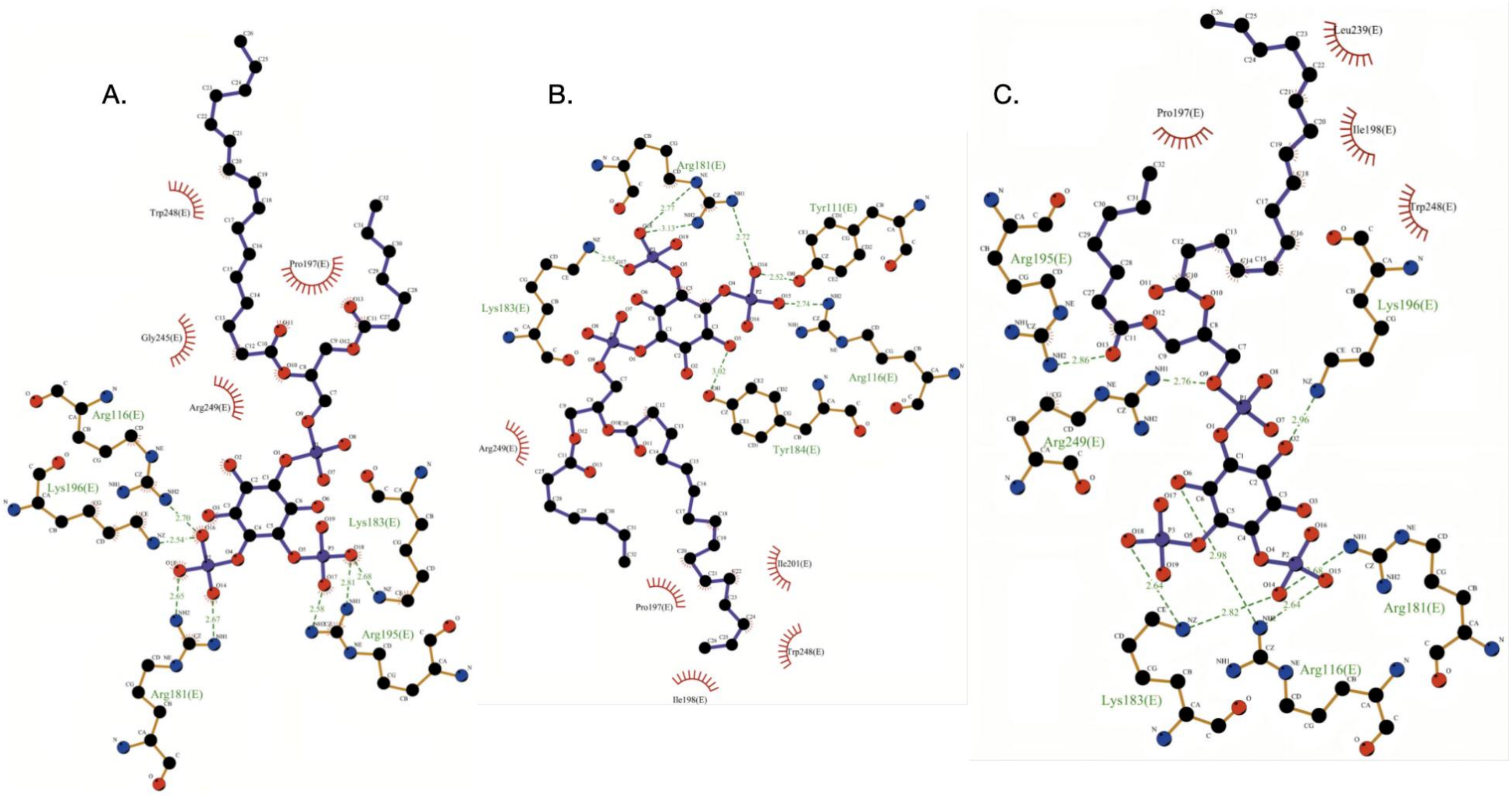

wt KCNQ1 KCNQ1-D242N KCNQ1-R243H

Figure 25. KCNQ1-PIP₂ and KCNQ1-KCNE3 interactions derived from the final frame of 100 ns MD simulations. (A-C) 2D representations of interactions between PIP₂ and (A) wild-type KCNQ1, (B) KCNQ1-D242N, and (C) KCNQ1-R243H, generated using Ligplot. Green dashed lines indicate hydrogen bonds, while red arcs represent hydrophobic contacts.

4.3.3 Conformational Dynamics: Principal Component Analysis and Free Energy Landscape

PCA Analysis

To determine the dominant conformational movements in KCNQ1 WT and mutant systems, we performed PCA on the MD trajectories. This approach showed that the several eigenvectors captured the majority of the most significant conformational changes. The first 50 principal components were calculated, and the first 20 components are selected to inspect their contribution to the whole fluctuation of complexes, shown on the right side of Figure 26 A-C. These plots indicate the variation in the conformational distribution of the KCNQ1 chain A, as represented by the dots in each panel. The magnitude of the corresponding eigenvalues exhibited a progressive decreasing tendency, eventually converging to constrained and more localized fluctuations. The PCA scatter plots (Figure 26) show the backbone dynamics of KCNQ1 chain A, which is chosen as a representative subunit of the tetrameric KCNQ1 channel. This analysis compares WT (shown in black), D242N (shown in red) and R243H (shown in green) variants by projecting trajectories onto the first two principal components (PC1 and PC2), which represents distinct conformational behaviors.

PCA for WT KCNQ1 (Panel A) showed that it takes up a tightly clustered subspace, suggesting stable internal motions with minimal structural deviations (PC1:24.92%, PC2:14.31%). In contrast, the D242N mutant (Panel B) exhibits broader dispersion, particularly along PC2 (PC1: 27.70%, PC2: 17.45%), indicating enhanced flexibility. The R243H mutant (Panel C) shows even greater spreading along both axes (PC1: 34.85%, PC2: 15.31%), signifying substantial mutation-induced conformational changes and increased atomic fluctuations. The combined PCA (Panel D) further emphasizes these differences, with mutants occupying larger subspaces compared to the WT.

A

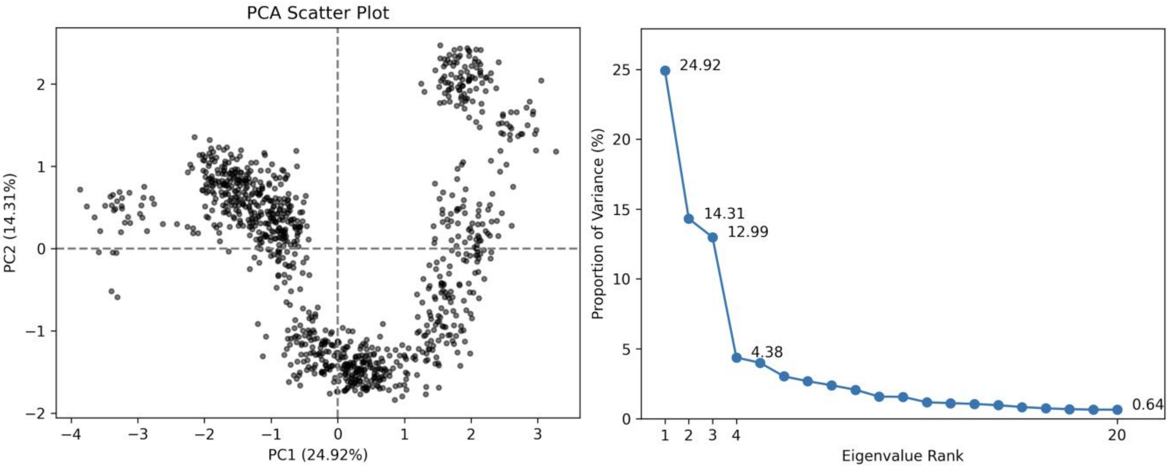

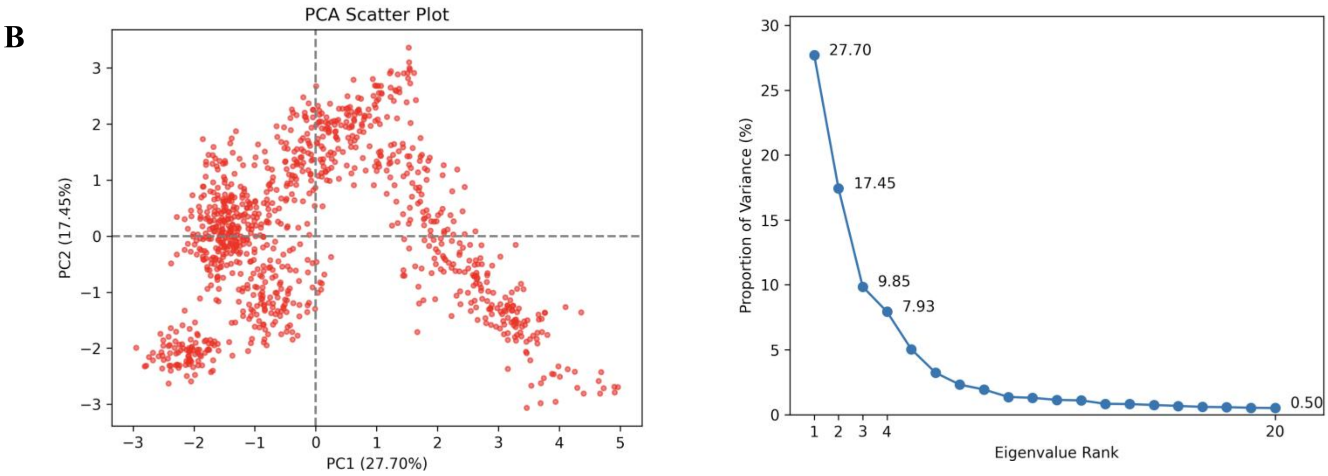

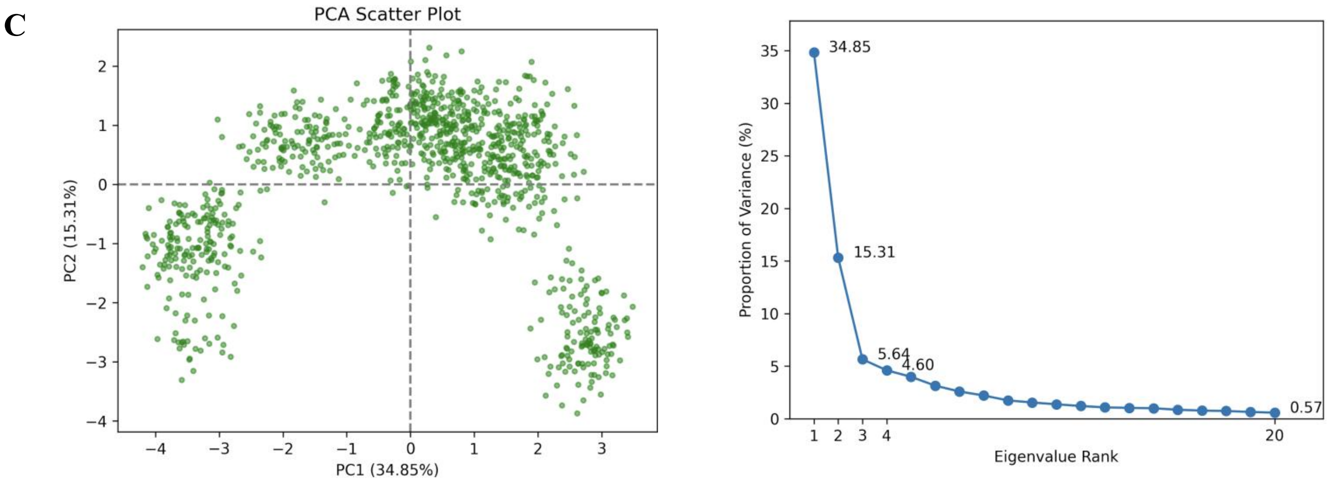

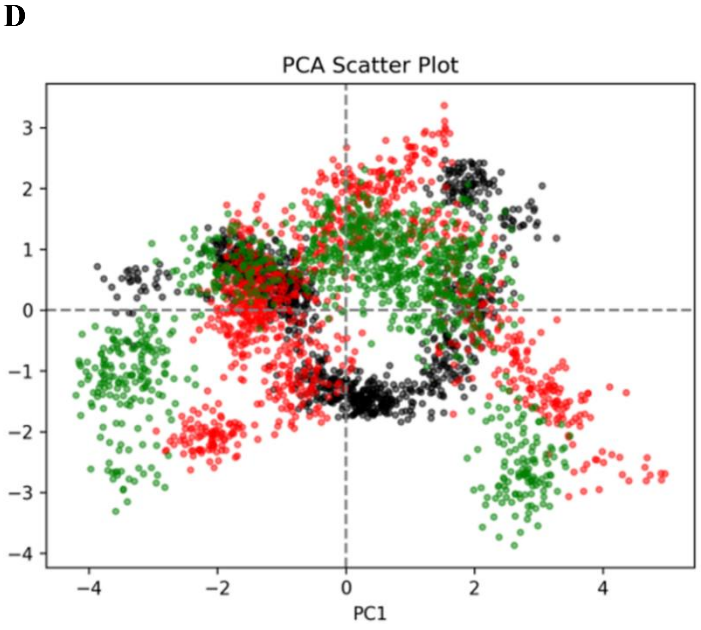

Figure 26 Principal component analysis (PCA) for wild-type and mutant KCNQ1. 2D plots represent the projection revealing conformational dynamics of KCNQ1 chain A backbone atoms along the first two eigenvectors (PC1 vs. PC2).
(A) Wild-type KCNQ1 shown in black,
(B) KCNQ1-D242N mutant shown in red,
(C) KCNQ1-R243H mutant shown in green,
(D) Combined PCA data for wild-type and both mutants. The percentage of principal motions represented by their corresponding eigenvectors are displayed on the right side of each plot for panels (A), (B), and (C).

FEP Analysis

The free energy landscapes (FELs) were generated from the probability density sampled within the simulation period using RMSD and Rg as collective variables. In these landscapes, dark blue regions represent the most frequently sampled conformational states, corresponding to local metastable minima within the simulation window, while yellow regions indicate maximum energy (unstable states). The WT KCNQ1 (Figure 27A) displays a broad yet well-defined conformational distribution with relatively low Rg values, suggesting that it maintains a compact and stable structure with multiple low-energy states.

In contrast, the D242N mutation result (Figure 27B) displays a more rugged FEL with quantifiable shifts in energy distribution, reflecting reduced stability and increased conformational heterogeneity, characterized by a lack of well-defined global minima and broader RMSD ranges. The R243H mutation (Figure 27C) caused more substantial effects on the conformational behavior, showing a highly rugged and scattered FEL with higher energy values and broader RMSD and Rg ranges, indicating reduced stability and greater conformational variability. This analysis shows that both mutations alter the size and position of the sampled essential space of KCNQ1, with the R243H mutation causing the most extensive instability.

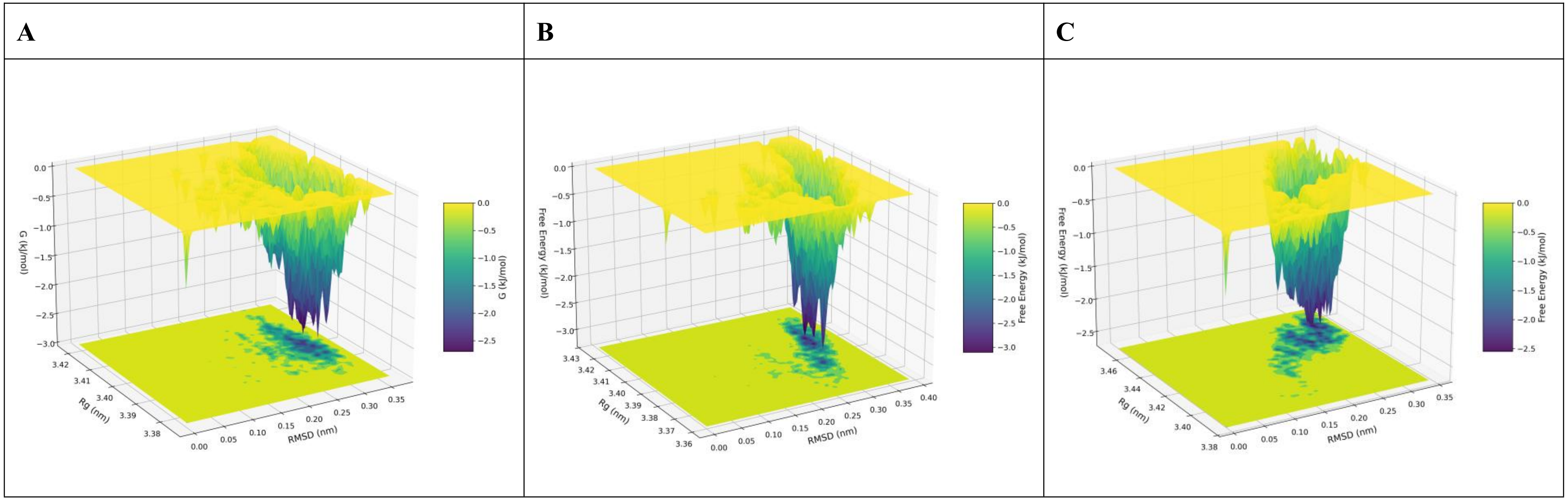

Figure 27. Free energy landscape (FEL) of KCNQ1 and its variants. The Gibbs free energy landscapes were derived from 100 ns molecular dynamics (MD) simulations based on root mean square deviation (RMSD) and radius of gyration (Rg). Panels show (A) wild-type KCNQ1, (B) the D242N mutant, and (C) the R243H mutant. Dark blue regions represent stable states with minimum energy, while yellow regions represent unstable states with maximum energy, respectively.

4.3.4 Integrative Discussion: Molecular Mechanisms of LQT1 Pathogenicity

The computational analyses presented in the present study provide a comprehensive structural basis for understanding how the D242N and R243H mutations translate into the loss-of-function phenotypes characteristic of LQT1 syndrome. By combining data from structural dynamics, energetic landscapes, and interaction networks, we can find distinct mechanistic pathways for each variant. These findings not only substantiate existing experimental data regarding VSD dysfunction but also provide novel atomic-level explanations for the different behaviors of these pathogenic variants.

The results indicate that the VSD-PIP_2 interface is sensitive to local charge density. The S4-S5 linker region acts as a sensor for the anionic lipid headgroups, a crucial interaction for coupling VSD movement to pore opening. Our data reveals that the D242N mutation, by neutralizing a negative charge, indirectly enhances the binding affinity of proximal basic residues to PIP_2. This is quantitatively supported by the hydrogen bond analysis (Table 3), which shows a redistribution of occupancy where proximal residues like Arg116 and Arg181 interact more tightly with the lipid headgroup. While enhanced binding might intuitively suggest structural stability, in the dynamic context of channel gating, this likely represents a pathological overly stabilized state. Physiological gating requires the S4 helix to move upward during depolarization, an activity that depends on the transient breaking and reforming of interactions. The excessive electrostatic attraction implies an electrostatically locked state, where the VSD is energetically trapped in a resting conformation by PIP_2, thus increasing the energy barrier required for activation. This aligns with electrophysiological studies showing that charge-neutralizing mutations in the S4 segment often lead to significant rightward shifts in voltage dependence.

In contrast, R243H leads to structural disintegration and increased interdomain flexibility, which may weakens VSD-pore coupling. By removing a critical positive attractor charge (Arginine), the mutation significantly weakens the local electrostatic field that normally recruits PIP_2 to the VSD interface. This weakening of interfacial electrostatic stabilization explains the dramatic increase in the Rg (Figure 22B) and SASA (Figure 22C) observed in our simulations. More critically, this local destabilization propagates to induce long-distance allosteric consequences. The RMSF analysis (Figure 22D) revealed that structural fluctuations were not confined to the mutation site but propagated throughout the entire S4-S5 linker (residues 104-258). This increased thermal fluctuations is particularly detrimental to channel function. The S4-S5 linker functions as a mechanical lever, and must maintain mechanical integrity to effectively translate VSD displacement into gating of the pore. The loosening state of this linker observed in the R243H mutant effectively uncouples these two domains. Consequently, even if the voltage sensor moves in response to membrane depolarization, the force may not be effectively transmitted to open the pore, resulting in a comparatively silent or non-conducting channel phenotype which is often be seen in severe LQT1 cases.

Furthermore, the FEL analysis clarifies global-local mismatch in the thermodynamic basis of these dysfunctions. As visualized in the PCA projections (Figure 26) and FEL contour maps (Figure 27), the mutant landscapes are characterized by a flattening of the energy basins and the emergence of multiple shallow, metastable minima compared to the compact basin of the WT. This indicates that the mutations lower the network connectivity of protein. Specifically for R243H, we observed a paradox where global analysis (RMSD, Figure 22**A**) indicate disorder, but specific interface residues (e.g., KCNE3-Tyr60 and KCNQ1-Ser330, Figure 23**A**) are trapped in high-occupancy hydrogen bonds. This phenomenon suggests a rugged free-energy landscape with locally over-stabilized contacts, where the protein cannot simultaneously satisfy its global folding requirements and its local interaction needs. This duality highlights that pathogenicity is not merely a result of protein unfolding, but rather a sophisticated perturbation of the dynamic ensemble, where the channel is trapped in non-productive intermediate states that are not accessible to the WT protein.

In conclusion, these results identify the sites of D242 and R243 as a critical structural hub within the KCNQ1 complex. Its integrity is essential for maintaining the subtle balance between VSD mobility, lipid recruitment and subunit assembly. The distinct molecular behaviors of D242N (electrostatic locking) and R243H (structural decoupling) highlight the complexity of genotype-phenotype associations in LQT1. These structural insights have significant implications for more precise medicine and drug discovery. Therapeutic strategies for D242N might require negative allosteric modulators or lipid-analog compounds that can compete with PIP_2 to loosen the electrostatic lock, thereby lowering the activation barrier. In contrast, R243H would likely benefit from interfacial stabilizers that bind to the VSD-pore interface to compensate for the lost Arg243 anchor, restoring the structural integrity of the force transmission pathway.

4.4 Structural Basis of KCNQ1 Activation: Docking at the Activator Pocket

This section explores the structural determinants underlying KCNQ1 activation by natural compounds, focusing on ligand occupancy of the ML277 activator pocket. Docking approach is first validated by reconstructing the ML277 binding pose, and then applied to tanshinone IIA, resveratrol, and quercetin. MD simulations are subsequently used to assess the dynamic persistence of the docked complexes and to characterize the interaction network supporting stable binding under thermal fluctuations.

4.4.1 Validation of the Docking Protocol

Molecular docking is a useful *in silico* approach for investigating the binding site and binding affinity of receptor-ligand complexes. Before docking the ligands of interest, the protocol was validated by re-docking ML277. ML277 is the native KCNQ1 activator, and its binding pose has been resolved in a KCNQ1-ML277 cryo-EM structure (PDB ID: 7XNK). ML277 was re-docked into the truncated KCNQ1 model to confirm whether the predicted pose reproduces the experimentally observed binding mode. The docking grid box was set to encompass the whole ML277 pocket. The box also covered adjacent candidate sites within the inter-subunit cavity formed by three KCNQ1 subunits, ensuring enough sampling space of the relevant binding region. The docking result showed that ML277 was docked in the original binding site of the KCNQ1 with a docking score of -9.2 kcal/mol. Additionally, the RMSD value between native ML277 and the best binding pose of docked-ML277 is 1.50 Å (Figure 28). As an RMSD value less than a threshold of 2 Å is generally considered an acceptable solution [209], the docking result of ML277 supports the suitability of the workflow for reproducing the known ML277 binding pose. This re-docking process confirms that the force field parameters and search algorithm can recover a reported pocket in this KCNQ1 model.

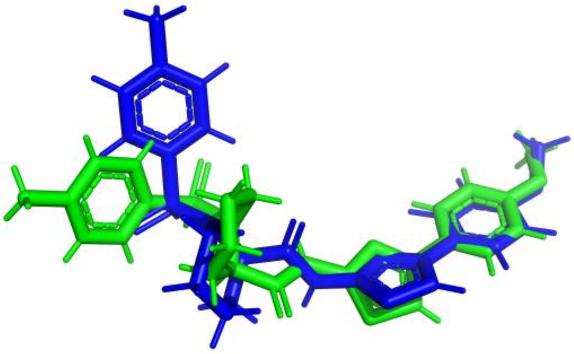

Figure 28. Cryo-EM resolved and re-docked ML277 structures in KCNQ1 binding site. **The calculated RMSD value for heavy atoms is** 1.49 Å. The co-crystallized ML277 from 7XNK.pdb is colored green, while the best binding pose of the re-docked ML277 structure is colored blue.

4.4.2 Prediction of Binding Modes via Molecular Docking

The most favorable binding poses of tanshinone IIA, resveratrol and quercetin were ranked first according to the docking scores. As indicated in Figure 29A, tanshinone IIA, resveratrol and quercetin can fit into the same binding site as ML277. Specifically, the binding modes of the tested ligands exhibited similar orientations. While docking scores provide a qualitative ranking, the structural complementarity is of greater mechanistic relevance. The predicted binding energies were: ML277 (-9.1 kcal/mol), tanshinone IIA (-8.8 kcal/mol), quercetin (-7.5 kcal/mol) and resveratrol (-7.1 kcal/mol). Given the intrinsic uncertainty of docking scores, the small difference between quercetin and resveratrol is not interpreted as a meaningful separation in binding strength. The score of these binding poses ranges from -8.8 to -8.1 kcal/mol for tanshinone IIA, -7.1 to -6.2 kcal/mol for resveratrol and -7.5 to -6.4 kcal/mol for quercetin. The docking results suggest that tanshinone IIA, resveratrol and quercetin can interact with KCNQ1 and form plausible complexes. However, because docking scores are approximate and the receptor is treated as rigid, the stability and pose persistence require further verification by MD simulation.

Molecular docking approach has been successfully applied in exploring the binding pose of ligands for various proteins; however, it is not an efficient solution in evaluating conformational change of the receptor after binding with a ligand. In most of the docking methods, including AutoDock Vina in this study, only the ligand is treated as “flexible” molecule while the protein is treated as “rigid” object, which ignores the conformational change of protein during the docking process of ligands. To verify the docking results, 100 ns MD simulations were conducted on the docking complex with the most negative score for each ligand.

4.4.3 Molecular Dynamic Simulations and Stability Analysis of Protein-Ligand Complexes

To explore the interaction of the protein-ligand complex, MD simulations were applied for 100 ns at 303.15 K. Parameters of RMSD, SASA, number of H-bonds and total energy derived from MD trajectories were used to evaluate the dynamic stability of protein-ligand complexes through modules of GROMACS. The last frames of ligands were taken from trajectories and superimposed (Figure 29B). Results derived from the last 30 ns of well-equilibrated trajectories for each system simulation. After MD simulation, it can be clearly observed that ML277 remains in the pocket, while the three tested ligands have slightly adjusted their orientations within the binding site.

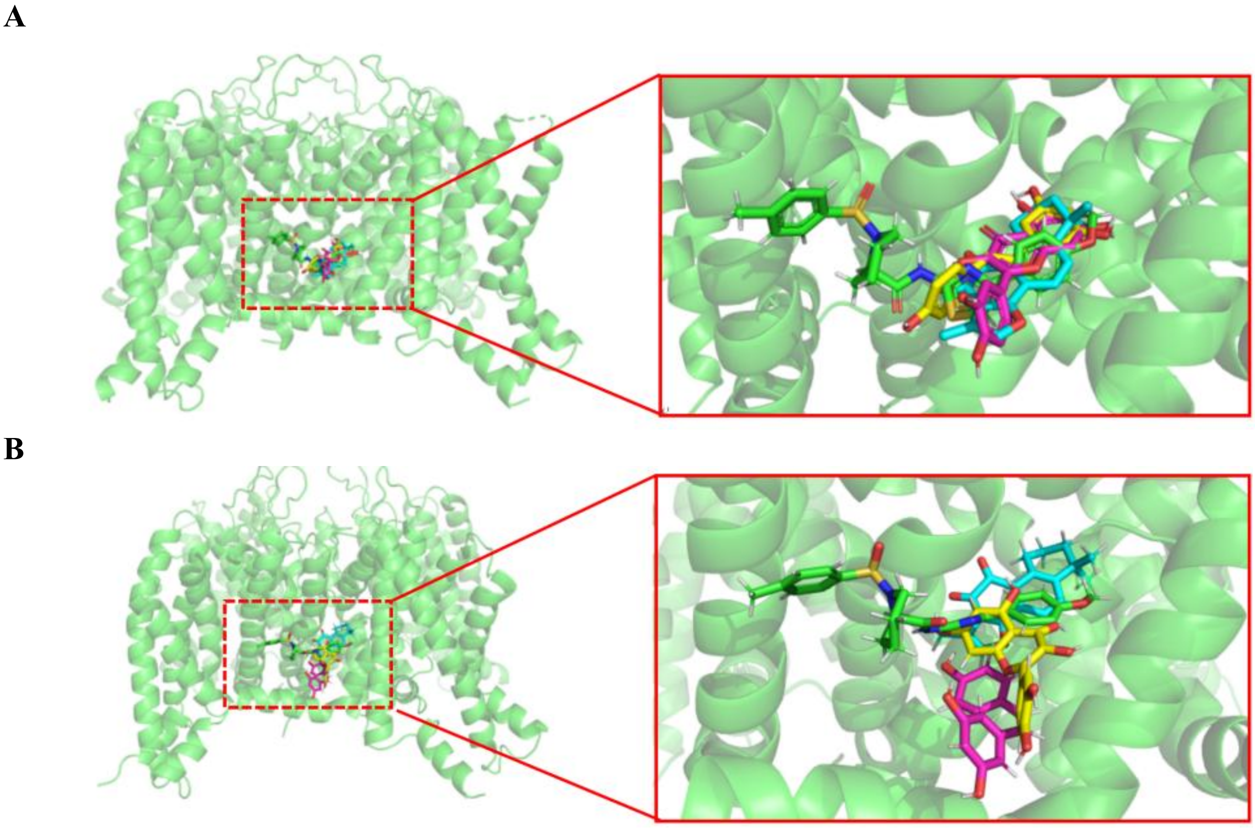

Figure 29. Comparison of the binding poses of selected ligands and the intrinsic ligand ML277. (A) The best binding pose of tanshinone IIA, resveratrol and quercetin were selected as representative and compared with native ML277; (B) The last snapshot of native ML277 and docking results of tanshinone IIA, resveratrol and quercetin in complex with KCNQ1 after 100 ns MD simulation were superimposed. The ML277 and the tanshinone IIA, resveratrol and quercetin are represented as sticks in green, cyan, magenta and yellow respectively. Proteins are represented as cartoon representation.

The 100 ns simulation timeframe was selected based on established protocols for membrane protein-ligand systems. Extended timescales are required to characterize full unbinding events. However, the selected duration is sufficient to observe the "induced-fit" arrangements of the binding pocket and the equilibration of ligand poses within the bound state, which is the major focus of this interaction stability analysis. The temperature of 303.15 K was chosen following established protocols for ion channel MD simulations, as consistently used in recent studies of voltage-gated potassium channels [210-211]. This temperature represents a compromise between physiological relevance and computational stability, providing sufficient thermal energy for conformational sampling while maintaining membrane integrity during extended simulations.

The observed positional adjustments of test ligands during MD simulation reflect the natural conformational sampling process, indicating that these compounds undergo adaptive binding that may enhance their interaction specificity with KCNQ1 (to be further supported by contact-occupancy analyses below).

RMSD of Protein and Ligands

The RMSD analysis provides information regarding the conformational variations compared to the reference structure. In the present study, the starting structure of the production MD run was used as the reference structure to calculate RMSDs to determine the convergence of the MD simulations over the course of MD simulations. Figure 30A displays the RMSD of C-alpha backbone atoms of KCNQ1 under conditions of binding with different ligands. The results showed that the structure of KCNQ1 bound with different ligands was equilibrated with minor fluctuations. Tanshinone IIA, resveratrol and quercetin show comparable overall protein RMSD levels to ML277. Inspection of Figure 30A reveals that RMSD of KCNQ1-Tanshinone IIA quickly achieved a plateau at ~8 ns and maintained stable till the end of simulation, compared to that of KCNQ1 bound to the other three ligands. Not only was the equilibration achieved quickly for KCNQ1-Tanshinone IIA, the average RMSD value was also the lowest (0.19 nm) while that of KCNQ1-ML277, KCNQ1- resveratrol and KCNQ1-quercetin were close with values of 0.25 nm, 0.23 nm and 0.25 nm, respectively.

Besides, RMSD of KCNQ1-quercetin was observed to be stable after 60 ns of simulation while RMSD of KCNQ1-ML277 and KCNQ1- resveratrol encountered a slightly higher fluctuation, ranging from 0.21~0.28 nm. Generally, the simulation system is considered to be in equilibrium state when average RMSD fluctuations are less than 0.2 nm [212]. These observations indicate that tanshinone IIA and resveratrol maintain a stable protein conformation throughout the simulation, with tanshinone IIA exhibiting the lowest backbone fluctuations among the tested ligands, which may lead to slightly reduced backbone fluctuations under the present simulation conditions. Studies have used molecular docking to explore the interaction between tanshinone IIA and other targets. Zeng and co-workers used a molecular docking method to find that tanshinone IIA can bind to liver X receptor alpha, which may lead to transcriptional activation [213]. The docking study from Liu et al. revealed that tanshinone IIA has a high affinity for NF-kappa B1, p53 and Bcl-2, and the results were further validated through Western blotting experiment [214].

To evaluate the stability of ligands, the RMSD values of ligands were calculated and shown in Figure 30B. Resveratrol was very flexible from 0-45 ns and then became stable till the end of MD simulation. The trajectories of resveratrol demonstrated that two hydroxyl (-OH) groups at C3 and C5 located in ring A moved toward solvent environment, leading to the drastic fluctuation of RMSD. In the equilibrium stage, RMSD of tanshinone IIA and resveratrol are higher with the similar value of 0.1 nm, while the RMSD of ML277 and quercetin are lower with the similar value of 0.05 nm. Therefore, it can be concluded that the native ligand and tested ligands become stable during MD simulations in terms of remaining bound and reaching RMSD plateaus. Interactions between KCNQ1 and other ligands also have been studied. Wang et al. found that KCNQ1 can bind to hesperidin and tetrahydropalmatine with high affinity [215].

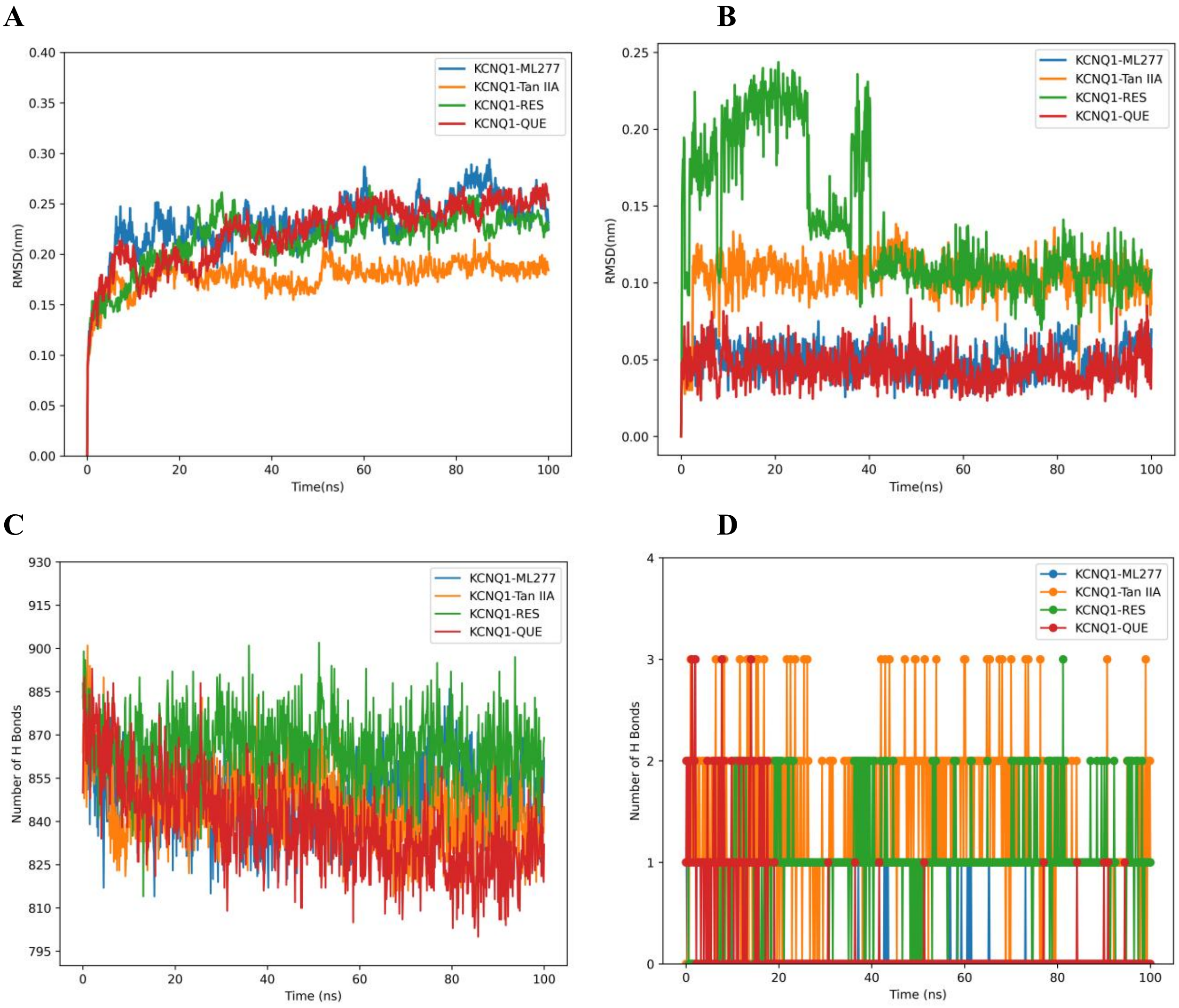

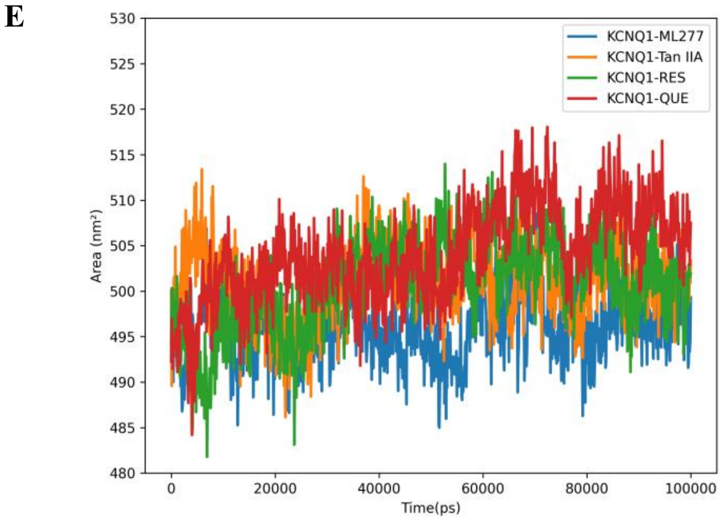

Figure 30. Characterization of conformational stability of KCNQ1 bound to different ligands. (A) Cα-RMSD of KCNQ1. (B) RMSD of four ligands. (C) H-bonds for KCNQ1 bound with different ligands. (D) H-bonds formed between KCNQ1 and different ligands. (E) Solvent accessible surface (SASA) analysis of KCNQ1, KCNQ1-ML277, KCNQ1-Tan IIA, KCNQ1-RES and KCNQ1-QUE are displayed in blue, orange, green and red, respectively. Tan IIA, tanshinone IIA; RES, resveratrol; QUE, quercetin.

Hydrogen-Bond Analysis

H-bond analysis is commonly used in examining protein-ligand interactions[216]. The number of H-bonds and distributions were calculated to examine the stability of KCNQ1-ligand complexes during MD simulations. The obtained data is based on H-bonds between acceptor and donor with distance less than 3.5 Å and angle more than 120°. The number of intramolecular hydrogen bonds within KCNQ1 (approximately 827-864 across systems) provides an initial indicator of global protein hydrogen-bonding patterns. As these are not protein-ligand hydrogen bonds, they should be interpreted as background stability descriptors rather than direct measures of ligand binding strength.

Furthermore, the intermolecular H-bonds between KCNQ1 and ligands were also explored, which can be observed in Figure 30D. In the last 30ns simulation, the minimum number of intermolecular H-bonds was identified to be zero in the KCNQ1-ML277 complex while the maximum number of intermolecular H-bonds were observed in KCNQ1-Tanshinone IIA with 2-3 H-bonds. The observation that the KCNQ1-ML277 complex contained fewer intermolecular H-bonds suggests that ML277 binding is dominated by hydrophobic contacts (with polar interactions playing a transient orienting role), whereas tanshinone IIA involves in more persistent hydrogen bonding, suggesting that more KCNQ1 residues participate in polar interactions with tanshinone IIA, potentially contributing to pose stabilization.

The higher number of intermolecular hydrogen bonds observed for tanshinone IIA (2-3 inter-molecular H-bonds) compared to ML277 (0-1 H-bonds) suggests increased polar-contact stabilization and potentially improved pose persistence. These additional polar contacts create multiple stabilization points between the ligand and protein, which may facilitate more consistent channel gating.

Analysis of solvent accessible surface area

The time-dependent SASA was calculated to identify the protein surface area accessible to solvent molecules, as SASA of a protein is viewed as a significant factor in protein stability determination. Less protein surface area exposed to solvent signify that those amino acids tend to bury inside the hydrophobic core. Protein interacts with solvent molecules at its surface by polar and nonpolar interactions. As shown in the graph of SASA (Figure 30E), the SASA profiles of KCNQ1 remained noticeably consistent across different ligand-bound states. The average SASA values for KCNQ1-ML277, KCNQ1-Tan IIA, KCNQ1- resveratrol and KCNQ1-quercetin were close with values of 497, 501, 502 and 507 nm^2, respectively, this lack of significant deviation suggests that the binding of these ligands preserves the global structural integrity of the channel without inducing major unfolding or compaction events. This minimal variation in SASA indicates that these TCM-derived ligands (tanshinone IIA, resveratrol, and quercetin) induce subtle conformational adjustments in KCNQ1, at the whole-protein level. In comparison, previous studies have reported more marked SASA alterations upon ligand binding in other systems. Elebeedy et al. found that tanshinone IIA interacts with hemagglutinin and neuraminidase and cause large conformational change with SASA fluctuations ranging from 50-350 nm² [217], highlighting capacity of tanshinone IIA for significant structural modulation in viral proteins, which contrasts with the milder effects observed here on KCNQ1 and suggests context-dependent binding behaviors. Similarly, Sajedeh et al. reported that resveratrol binds to phospholipase A2 and leads to the reduction of SASA by 1.21 nm² [218], implying a compaction effect that could enhance enzyme inhibition; this aligns partially with our findings, where resveratrol binding to KCNQ1 results in a slightly lower SASA compared to quercetin, potentially contributing to reduced protein mobility as seen in RMSD analyses. Furthermore, study from Dahiya et al. showed that pyruvate dehydrogenase kinase 3(PK3) and PK3-quercetin possesses similar SASA value [219]. supporting the notion that quercetin tends to maintain structural integrity without major solvent accessibility shifts, consistent with our observation of quercetin's SASA (507 nm²) being comparable to the ML277 control.

ML277-Phe335 interaction

Current studies have reported that in cryo-EM structure, Phe335 in S6 of KCNQ1 establishes a hydrogen bond with the amide group in ML277 [14], shown in Figure 31A. To investigate the stability of this interaction, we calculated the distance between the carbonyl oxygen of Phe335 and the amide nitrogen of ML277 throughout the MD simulation.

The results, presented in Figure 31B, reveal that the interaction is highly dynamic under the simulated conditions. The distance between the two groups exhibits large and rapid fluctuations, ranging from a minimum of approximately 0.4 nm to a peak of nearly 0.7 nm. Early in the simulation, it increases to a maximum of approximately 0.65 nm before decreasing to around 0.44 nm. It is critical to note that a stable hydrogen bond typically maintains a donor-acceptor distance below 0.35 nm. Throughout the simulation, the measured distance fluctuates significantly, frequently exceeding this threshold. This suggests that under dynamic physiological conditions, the ML277-Phe335 interaction is not a rigid anchor but a transient contact. We propose that the stability of ML277 binding is predominantly driven by the cumulative hydrophobic enclosure of the pocket, with the polar interaction serving a secondary role in transiently guiding ligand orientation rather than acting as a permanent thermodynamic lock. Accordingly, this contact is better considered as a dynamic orientational interaction than as a rigid object. Such a binding mode aligns with the nonpolar property of the surrounding residues, suggesting a model where modulate complementarity drives affinity while electrostatics determine specificity.

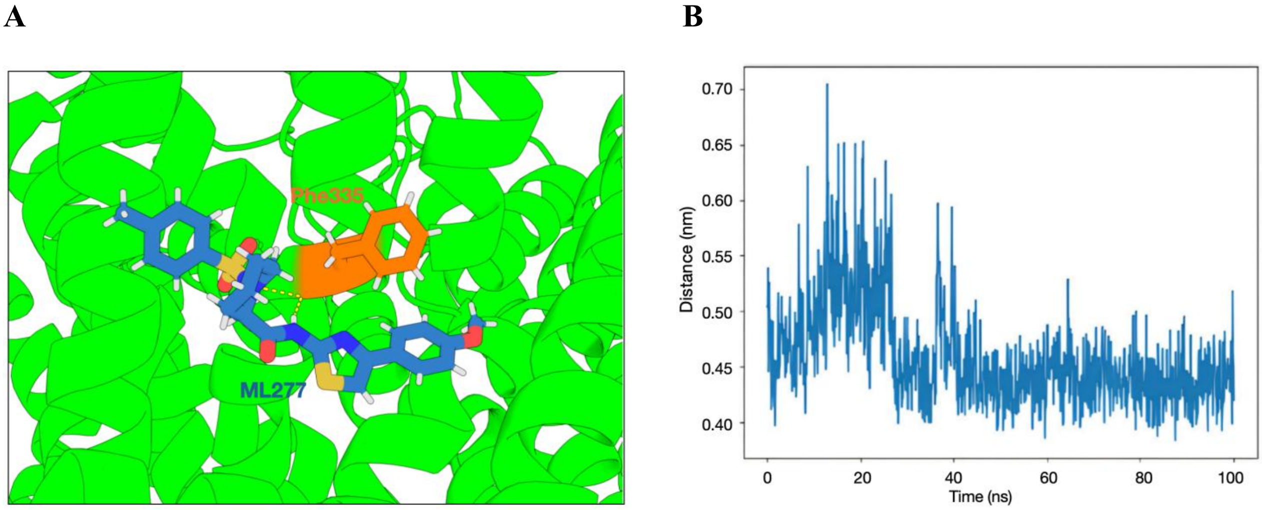

Figure 31. Molecular dynamics simulation of the interaction between KCNQ1 and ML277. (A) A representative snapshot from the simulation showing the hydrogen bond (yellow dashed line) formed between the backbone carbonyl group of Phe335 in KCNQ1 (orange) and the amide group of the ligand ML277 (blue). The KCNQ1 protein is shown as a green ribbon. (B) A plot tracking the distance between the carbonyl oxygen of Phe335 and the amide nitrogen of ML277 over the 100 ns simulation time.

Protein-ligand interactions

The systems were well-equilibrated after 100-ns MD simulation. The interaction of native ligand ML277 and ligands of interest with best binding pose (tanshinone IIA, resveratrol and quercetin) was observed and compared. The protein-ligand analysis generated from LigPlot+ given in Figure 32A-D demonstrates the possible hydrogen interaction as well as hydrophobic interaction between KCNQ1 residues and ligands. ML277 and resveratrol interact with KCNQ1 only via hydrophobic interactions. Specifically, more residues of KCNQ1, including Ile268, Gly272, Phe275, Val334, Phe335, Ala336, Ser338, Phe339 from chain A, and Thr265, Leu266, Pro343, Phe339 from chain D were involved in the interaction with ML277, while fewer pocket residues of KCNQ1, including Val255, Leu262, Leu266 and Leu347 from chain D, participated in interaction with RES. Meanwhile, the hydroxyl groups of tanshinone IIA and quercetin formed H-bonds with polar residues of KCNQ1(Figure 32B and Figure 32D). Specifically, tanshinone IIA formed H-bonds with Ser338, Ile337 and Ala336 from chain A of KCNQ1 with bond length of 3.3 Å, 2.9 Å and 3.0 Å respectively. For quercetin, it forms H-bonds with Val334, Phe335 from chain A of KCNQ1, with bond length of 2.6 Å and 3.2 Å respectively. Furthermore, the red arcs represented as hydrophobic residues of KCNQ1 interact with tanshinone IIA are Val334, Phe335 and Phe339 from chain A, in addition to Phe340, Gly269 and

Pro343 from chain D while that with quercetin are Phe339, Ser338 from chain A, in addition to Leu347, Leu262, Arg259, Ile263, Leu266, Pro343 from chain D.

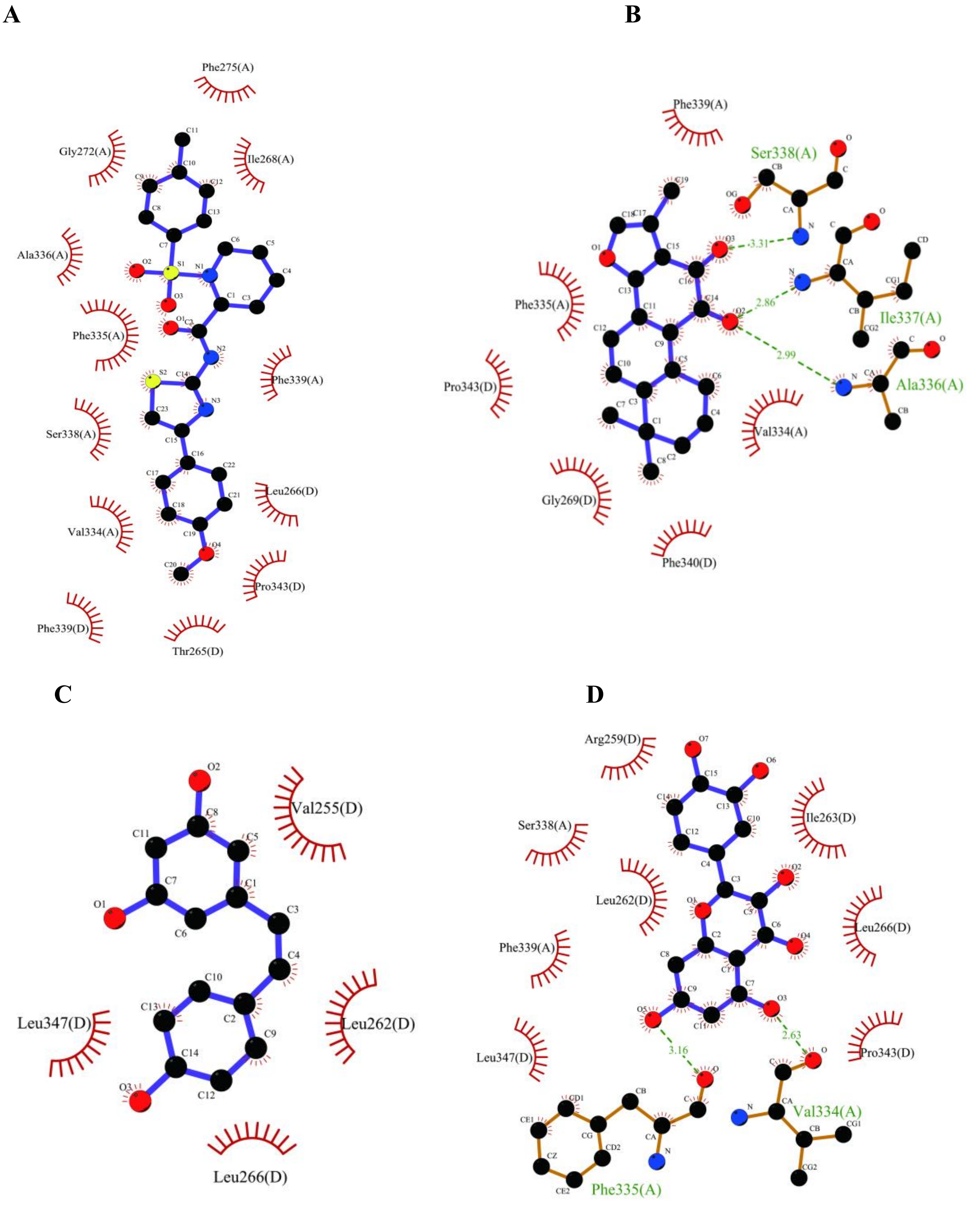

Figure 32. Analysis of protein-ligand interactions. (A) KCNQ1-ML277 complex. (B) KCNQ1-Tan IIA docked complex. (C) KCNQ1-RES docked complex. (D) KCNQ1-QUE docked complex. Structures were extracted from last frame of trajectories and the images of receptor-ligand binding domain were generated by LigPlot+ program. The H-bonds and hydrophobic interactions are shown in dashed green lines and red arcs respectively.

In conclusion, tanshinone IIA and quercetin can form plausible and persistent complex with KCNQ1 comparing with ML277 and resveratrol in this simulation, with tanshinone IIA showing more frequent polar contacts and quercetin showing extensive hydrophobic contacts. As there are more residues form the hydrophobic cavity for ML277, the interaction between KCNQ1 and ML277 is supported by a larger hydrophobic-contact network than that of resveratrol. Among the tested compounds, quercetin bound to KCNQ1 displayed greatly higher number of hydrophobic contacts than the other two. Despite similar molecular sizes, the different binding orientations observed for tanshinone IIA, resveratrol and quercetin after MD simulation likely demonstrate differences in their rotatable bond numbers and polar-group placement, which can influence local relaxation within the pocket.

4.4.4 Impact of Binding-Pocket Mutations on Ligand Affinity

ML277 has been reported to mainly interact with the nearby hydrophobic residues, including Trp248, Leu251, and Val255 in the S4-S5 linker, Leu262 and Leu266 in S5, Leu271 in neighboring S5’, and Phe335 and Phe339 in neighboring S6’. Additionally, studies by Ma et al. revealed that mutation of L271A and F335A impair the interaction between KCNQ1 and ML277 [14]. A comparison of WT (Figure 33A) and mutant (Figure 33B) KCNQ1 reveals that the binding pocket of KCNQ1-L271A/F335A is disrupted, as crucial hydrophobic interactions identified in the WT complex are altered. Further docking studies demonstrate that the top five predicted binding poses showed that ML277 adopted configurations that deviated more significantly from its known binding orientation (observed in the cryo-EM structure) when docked to the KCNQ1 L271A/F335A mutant compared to the WT protein. The mutant exhibited a broader range of less optimal binding poses (Figure 33C and Figure 33D). The replacement of L271 and F335 with alanine reduces the size and hydrophobicity of the side chains. Consequently, the docking algorithm, in seeking the most energetically favorable poses, cannot achieve the same optimal fit for the ligand in the mutated pocket, resulting in a wider distribution of binding orientations and increased spatial deviation from the native cryo-EM binding mode. Consistent with the altered binding poses, the predicted binding energies for ML277 with the KCNQ1 L271A/F335A mutant were less favorable (higher energy values) compared to those calculated for the WT KCNQ1 complex. Specifically, the top five docking scores for the WT protein were -9.2, -9.2, -8.9, -8.7, and -8.6 kcal/mol (average: -8.9 ± 0.3 kcal/mol), while those for the mutant were -8.3, -8.2, -8.1, -8.1, and -8.1 kcal/mol (average: -8.15 ± 0.10 kcal/mol). This represents an average energy penalty of approximately 0.76 kcal/mol in the mutant, indicating reduced binding affinity. While docking scores are semi-quantitative, this consistent energy gap suggests a reduction in shape complementarity and van der Waals contacts in the mutated pocket. These findings provide a structural rationale for the experimentally observed reduced efficacy, highlighting the sensitivity of ML277 binding to the precise hydrophobic packing of the S5-S6 linker region.

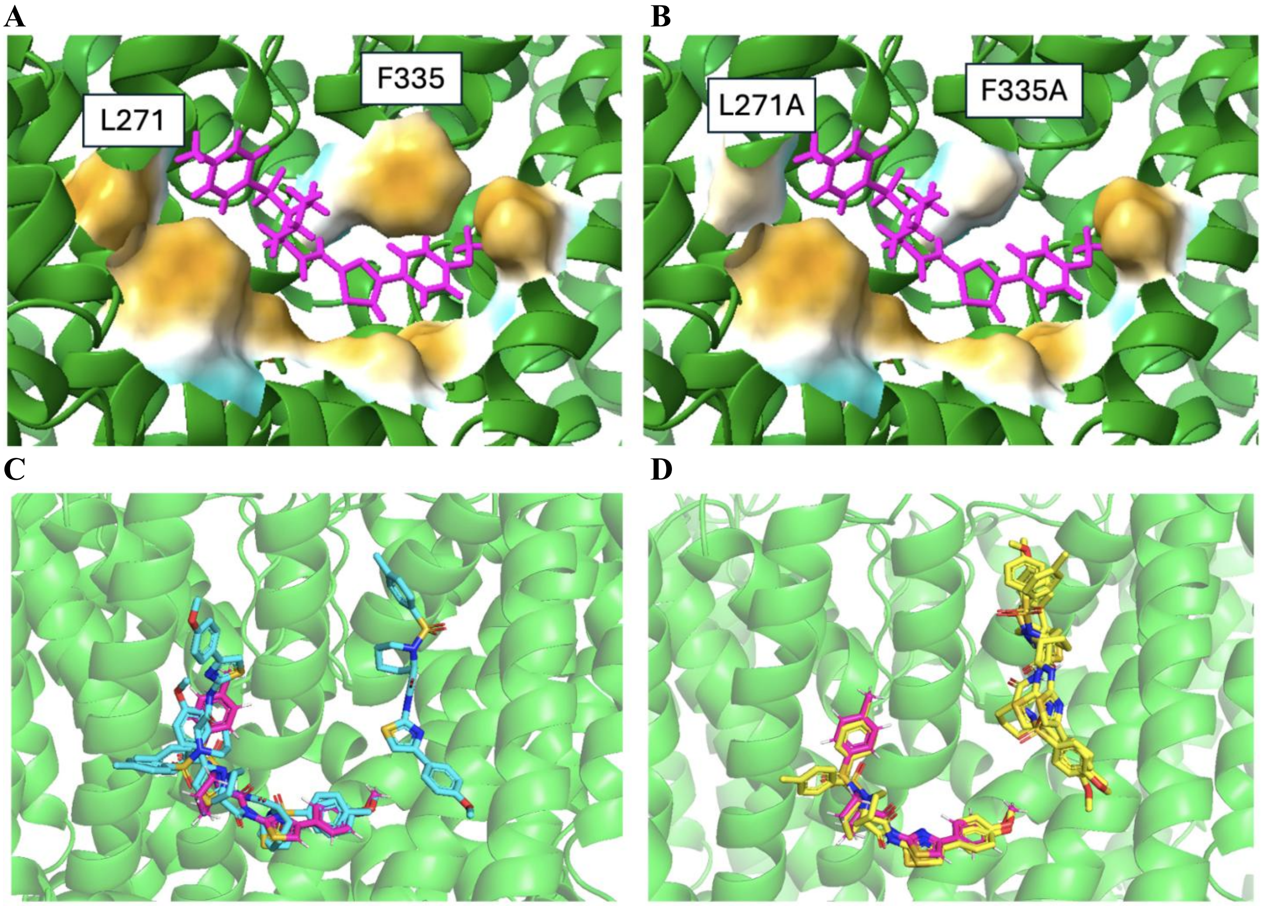

Figure 33. (A) The ML277 binding pocket in wild-type KCNQ1 and (B) in the L271A/F335A mutant. In both panels, ML277 is shown as a magenta stick representation. Key residues lining the hydrophobic pocket are displayed using a hydrophobic surface representation. (C, D) Superposition of the top five predicted binding poses of ML277 docked to (C) wild-type KCNQ1 and (D) the KCNQ1-L271A/F335A mutant, respectively. In both panels, the poses are ranked by docking score and shown for comparison with the reference cryo-EM pose of ML277 (magenta).

These mutational effects support the critical role of hydrophobic residues in stabilizing ML277 binding. Mechanistically, the L271A/F335A mutations diminish van der Waals interactions and reduce hydrophobic packing of the pocket, leading to less favorable docking scores and a broader distribution of poses. While docking results are not a quantitative free-energy measurement, this may correlate with reduced channel activation efficacy, as altered binding disrupts KCNQ1 conformational dynamics essential for ion conductance [14]. Clinically, such insights highlight vulnerabilities in ML277-based therapies for LQT1, where genetic polymorphisms at these sites could confer resistance.

These computational predictions match experimental observations. When introducing L271A/F335A mutations, binding affinity was predicted to decrease by 0.76 kcal/mol, which represents a moderate decrease in docking score that may reduce drug effectiveness in terms of pocket complementarity. This has practical implications for treating LQT1 patients. If patients carry genetic variants in these binding sites, they might respond differently to KCNQ1 activators. Understanding how specific residues affect ligand binding helps us design better compounds that work even when these sites are altered.

4.5 Antioxidant Screening and KCNQ1 Docking of Lead TCM Constituents

The preceding sections established that KCNQ1 function can be modulated through direct binding of small molecules to specific channel sites. In addition to ligand-mediated gating, channel dysfunction also can be caused by oxidative modification of susceptible residues, particularly under conditions of increased ROS. Therefore, a comprehensive therapeutic strategy requires not only physical activation but also chemical protection. In this final section, we investigate an integrative mechanism where effective therapeutics might function by both systematically scavenging ROS and associating with the channel to provide a localized antioxidant microenvironment for sensitive residues.

To investigate this, we integrated biochemical screening with computational modeling. We first evaluated aqueous extracts from nine Traditional Chinese Medicines (TCMs) to identify the candidate with superior antioxidant capacity. Subsequently, we used molecular docking approach to examine whether the main bioactive constituents of the lead extract could physically associate with the KCNQ1 channel surface, specifically targeting the redox-sensitive Cys214 region of KCNQ1 to evaluate potential localized protection.

4.5.1 Quantification of Total Phenolic Content

The selection of the nine TCM species was based on the inclusion in the 2020 MFH list and their documented cardiovascular benefits in traditional practice, providing a rational foundation for investigating their potential KCNQ1-protective mechanisms. The aqueous extracts of dry preparations of the studied plants were used because these agents are traditionally consumed in the form of medicinal infusions and decoctions in TCM, thereby ensuring the assessment of antioxidant activity reflects clinically relevant conditions.

As antioxidant capacity is significantly associated with phenolic compounds, the total phenolic content (TPC) of aqueous extracts from nine TCM plants and fungi was determined using a modified Folin-Ciocalteu method. The results were expressed as micrograms of chlorogenic acid equivalents per milliliter (µg/mL) of sample, calculated from the standard curve (Absorbance = 0.0027 × chlorogenic acid (µg/mL) + 0.0372, $R^2 = 0.995$). As shown in Figure 34, the TPC varied greatly among the tested species, ranging from 131.56 to 1258.52 µg/mL, indicating nearly a ten-fold difference.

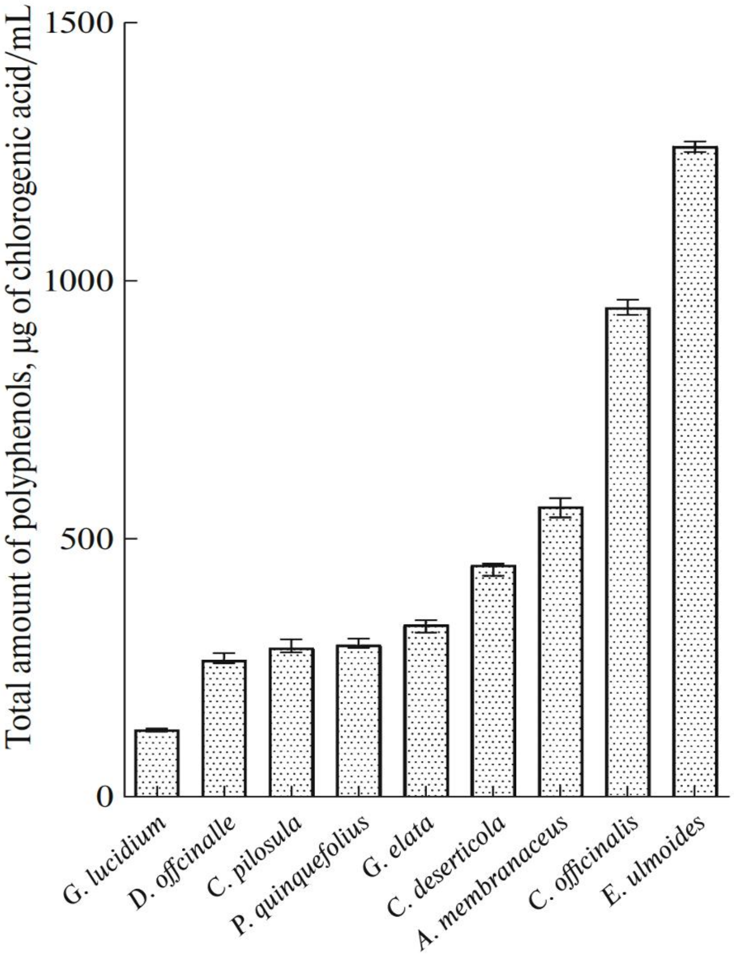

Figure 34. Evaluation of the total amount of polyphenols in aqueous extracts of traditional Chinese medicine.

E. ulmoides exhibited the highest phenolic content at a median of 1259.0 µg/mL (IQR: 1248.0-1269.0), followed by *C. officinalis* at 948.2 µg/mL (IQR: 933.3-963.0). In contrast, *G. lucidum* and *D. officinale* had the lowest TPC values, at 132.2 µg/mL and 266.7 µg/mL, respectively. These results highlight significant differences in phenolic compound content among TCM extracts, suggesting substantial variability in their antioxidant potential. This diversity likely stems from variations in phytochemical profiles, which are influenced by factors such as geographical origin, harvesting conditions, extraction methods, and environmental determinants like soil composition and climate. For instance, the high level of TPC in *E. ulmoides* could be attributed to its rich composition of flavonoids and lignans, which are known to confer robust free radical scavenging abilities [141]. This variability suggests substantial differences in their antioxidant potential, a critical consideration for therapeutic applications in oxidative stress-related disorders.

4.5.2 Evaluation of Total Antioxidant Activity via FRAP Assay

The Ferric Reducing Antioxidant Power (FRAP) assay was employed to evaluate the electron-donating capacity of the extracts. Figure 35 reveals considerable variation in total antioxidant activities. *E. ulmoides* and *C. deserticola* displayed the highest antioxidant activities, with values exceeding 6000 µmol/L and 4000 µmol/L, respectively, while *C. officinalis* also showed substantial activity at around 3000 µmol/L. In contrast, the remaining TCMs, including *G. lucidum*, *D. officinale*, *C. pilosula*, *P. quinquefolius*, *G. elata*, and *A. membranaceus*, exhibited much lower FRAP values, generally below 800 µmol/L.

These observations suggest that *E. ulmoides, C. deserticola* and *C. officinalis* are particularly rich in compounds capable of reducing oxidative stress through electron donation. These findings reveal the diversity in antioxidant potential among TCMs and highlight the importance of selecting specific herbs for antioxidant-related therapeutic applications.

A regression analysis was performed to correlate the results obtained with FRAP and TPC methods. The correlation coefficient between FRAP and TPC was positive ($R = 0.838$), indicating a strong positive correlation between phenolic content and ferric reducing capacity. As a result, the phenolic contents in aqueous extracts of plants significantly contribute to their antioxidant capacity. This result is consistent with previous research stating that phenolic compounds relate to ferric reducing potential [122, 220].

However, while the FRAP assay provides valuable insight into the electron-donating capacity of these extracts, it is a chemical assay performed under non-physiological conditions and does not directly establish biological efficacy. Therefore, we next evaluated the extracts using a lipid peroxidation model to obtain an orthogonal readout of protection against oxidative damage.

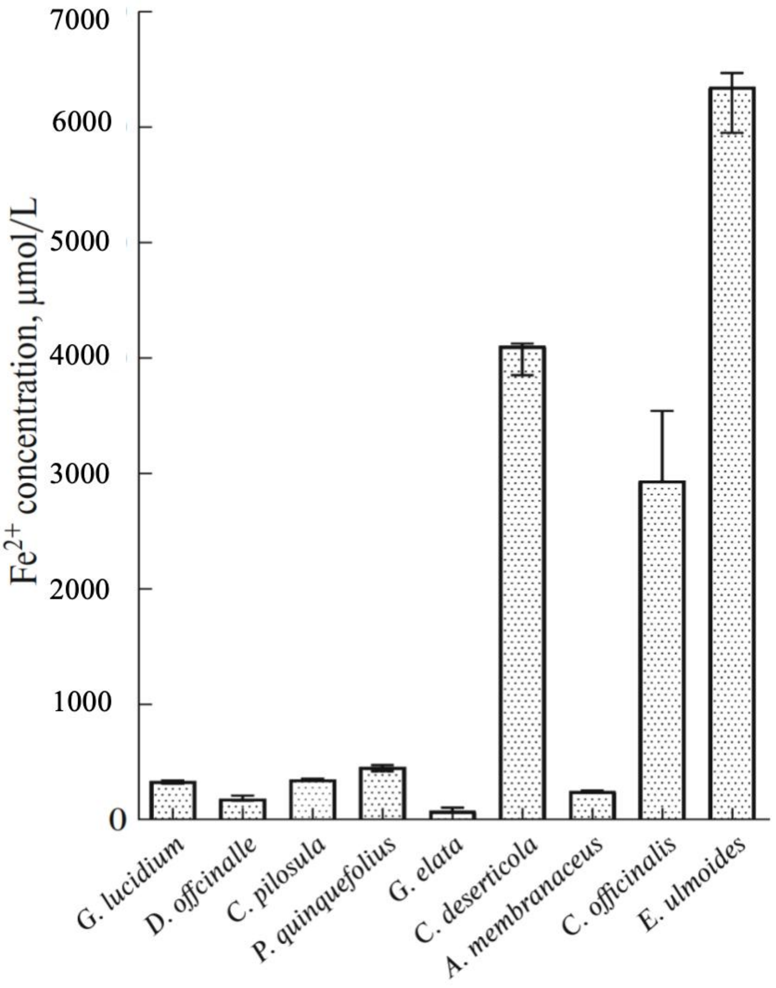

Figure 35. Total antioxidant activities in aqueous extracts of traditional Chinese medicine determined by FRAP.

4.5.3 Inhibition of Lipid Peroxidation

As the FRAP assay demonstrated the total antioxidant capacities of TCMs, we then proceeded with the lipid peroxidation assay which quantified MDA formation from lipid peroxides at 532 nm, providing a complementary analytical perspective by directly measuring oxidative damage in lipid membranes. While the FRAP assay evaluated the electron-donating capacity and general antioxidant potential, the lipid peroxidation assay specifically evaluates the efficacy of these compounds in preventing lipid degradation, a crucial aspect of oxidative stress-induced cellular damage. Evaluating MDA formation allows for a deeper understanding of the oxidative processes and potential protective effects of these compounds in biological systems.

Specifically, plasma incubation with Fe^{2+} led to oxidation of plasma lipoproteins, followed by the generation of secondary oxidized products (MDA). To ensure experimental design, the assay design included defined controls. Control 1 (Spontaneous Oxidation Control) consisted of human blood plasma and water incubated for 1 h at 37 °C without the addition of H_2O_2 and Fe^{2+}, establishing the background MDA level caused by thermal incubation alone. Control 2 (Time-zero Fenton Control) consisted of plasma to which H_2O_2 and Fe^{2+} were added, followed by immediate initiation of the TBARS measurement without incubation, capturing the baseline signal at the very start of the oxidative challenge. The Experiment Group (Fenton Induction) comprised plasma incubated with the Fenton reagent (H_2O_2 + Fe^{2+}) for 1 h; this group exhibited significantly elevated MDA levels compared to the controls, thereby validating the oxidative challenge model. Statistical analysis confirmed that the Experiment group was significantly different from both Control 1 and Control 2 (Figure 36A), demonstrating that the external Fenton reagent can notably increase MDA content in human blood plasma beyond spontaneous oxidation levels.

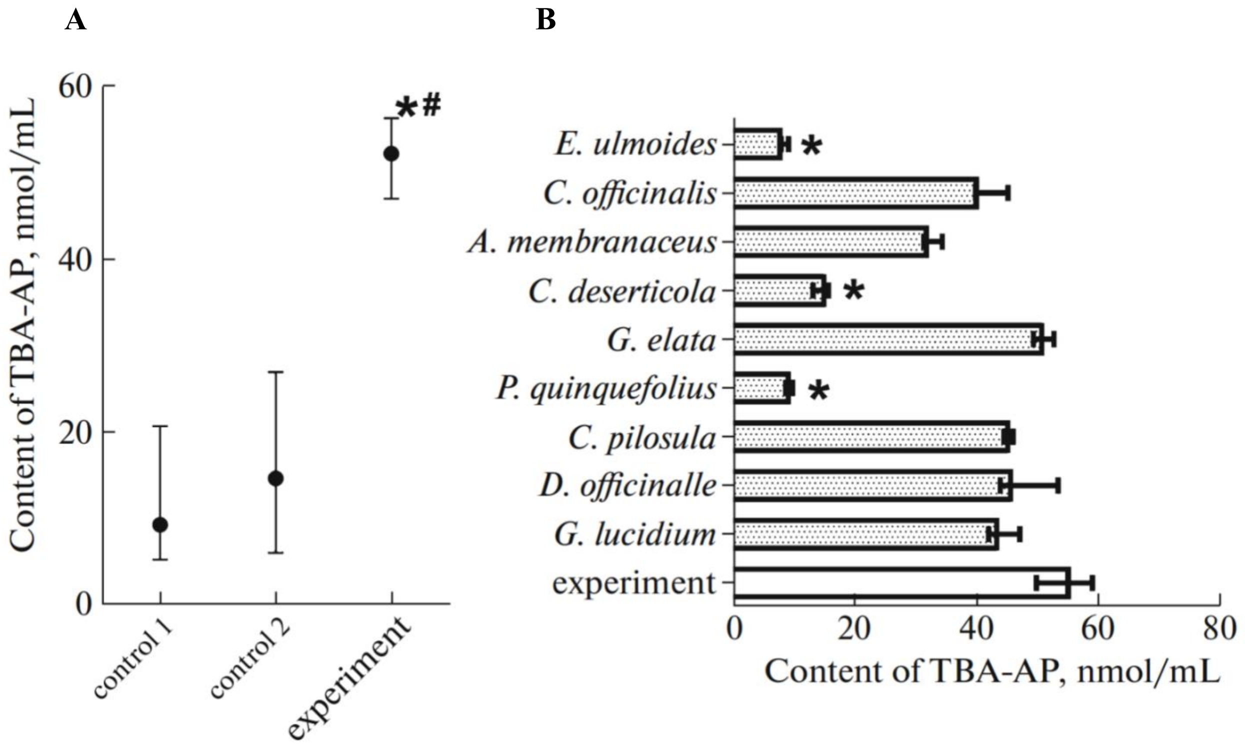

Figure 36. Evaluation of the antioxidant activity of aqueous extracts of traditional Chinese medicine according to their ability to inhibit the accumulation of TBA-active products in blood plasma induced by the Fenton reaction. (A) Accumulation of TBA active products 1 h after starting the Fenton reaction (experiment); the reaction was not started in control 1; TBA-active products were measured immediately after starting the reaction in control 2; (B) Accumulation of TBA-active products in the blood plasma induced by the Fenton reaction, without (experiment) and after the addition of TCM extracts; (*#) significant differences between groups (for A: * control 1 and experiment, # control 2 and experiment; for B: experiment and with the addition of extracts, respectively); differences were assessed using the Kruskal-Wallis test followed by a Dunn's post hoc test ($p < 0.05$).

Lipid peroxidation was assessed by measuring the formation of MDA using the thiobarbituric acid (TBA) method [201]. TBA-active products are the secondary oxidative product of lipid peroxidation. As a result, a higher concentration of MDA (TBA-reactive products) formed in the assay indicated a weaker the inhibitory effect of the extract on lipid peroxidation. According to the results, lipid peroxidation levels of 9 TCMs, measured as the content of TBA-active product (MDA), are given in Figure 36B. The experiments were performed in 3 replicates. By comparison with the Experiment (Fenton reaction without samples), aqueous extracts of the 9 samples reduced the Fenton reaction in plasma to varying degrees. The content of TBA-active products after treatment with *E. ulmoides*, *P. quinquefolius*, and *C. deserticola* was significantly different from that of the Experiment group (Fenton Reaction without sample), revealing that these three TCMs exert a strong inhibitory effect on the Fenton reaction. In other words, they exhibited strong antioxidant capacity. In particular, *E. ulmoides* showed the strongest oxidation resistance among all samples. However, *G. elata* showed the weakest antioxidant capacity. The remaining samples show moderate levels of inhibition.

The integrated application of TPC, FRAP, and lipid peroxidation assays demonstrates the antioxidant properties of the nine TCM extracts, with a strong correlation observed between phenolic content and overall antioxidative efficacy as assessed by the FRAP assay (R = 0.838). Notably, *E. ulmoides* consistently demonstrated superior activity across all methods, attributed to its high levels of flavonoids and lignans, while extracts like *C. deserticola* also showed robust performance in FRAP and MDA inhibition, highlighting its potential in mitigating oxidative damage. These findings demonstrate the variability in antioxidant potential among TCMs and emphasize the importance of phenolic compounds in electron donation and lipid protection mechanisms. However, limitations such as assay specificity and environmental influences on extract composition warrant further validation in more complex biological systems.

Despite these methodological limitations, the consistent results from three independent assays with different mechanisms collectively identify *E. ulmoides* as the best candidate among the nine screened TCM extracts for follow-up KCNQ1-focused, ROS-related mechanistic investigation. This biochemical advantage, shown through the highest phenolic content, excellent electron-donating ability, and most effective lipid protection, provides evidence for focusing future molecular modeling studies of *E. ulmoides* on its representative flavonoids, specifically rutin and quercetin. These investigations will help clarify the plausible molecular mechanisms by which these compounds protect the KCNQ1 channel, connecting traditional medicinal uses with modern understanding of cardiovascular ion channel function.

4.5.4 Molecular Docking of Rutin and Quercetin to the Redox-Sensitive Region of KCNQ1

The experimental analysis presented above demonstrated that *E. ulmoides* exhibits the strongest antioxidant capacity among the nine tested TCMs. However, effective protection of membrane proteins requires more than just systemic ROS scavenging; it requires the presence of antioxidant agents at the specific cellular compartments where oxidative damage occurs. Considering that *E. ulmoides* is characterized by a high abundance of flavonoids, specifically rutin and quercetin [140], these two compounds were selected as representative ligands to test for direct interaction with the Cys214 region, as these amphiphilic molecules preferentially partition into the membrane-water interface, effectively increasing their local concentration near the lipid bilayer compared to the bulk cytosol. While the wet-lab results confirm that *E. ulmoides* extracts show strong antioxidant activity in vitro, a critical question remains: Can these molecules associate with KCNQ1 in a manner consistent with a localized protective mechanism? Literature evidence highlights that Cys214 can act as a critical redox sensor for the channel. Bates et al. have found that Cys214 plays a crucial role in facilitating the tetramer formation and stability of KCNQ1 [101]. Moreover, research by Kerst et al. identified that the sulfhydryl-oxidizing agent thimerosal can interact with Cys214 residing in the KCNQ1 S3 segment, leading to an increase in I_{Ks} current [28]. To bridge the gap between wet-lab observation of systemic ROS-scavenging capacity in *E. ulmoides* extracts and the specific protection of KCNQ1, the biophysical behavior of its active constituents were considered. Since flavonoids like rutin and quercetin are amphiphilic and can partition into lipid bilayers, they may accumulate near the channel surface. Based on this information, we employed molecular docking as an exploratory tool to assess the geometric compatibility of these flavonoids with the redox-sensitive Cys214 region. This computational step aims to examine the structural plausibility of a localized interaction that could complement the systemic antioxidant effects.

Cys214-Proximal Docking Poses of Rutin and Quercetin

A binding box was configured to encompass the extracellular domain of a single KCNQ1 subunit including Cys214. The docking results show that rutin and quercetin possess the structural complementarity to occupy a pocket proximal to Cys214 (Figure 37A). It is important to acknowledge that Cys214 is located in a solvent-exposed region, making specific ligand targeting challenging. Molecular docking simulations suggest that both ligands possess the geometric complementarity to occupy a shallow, amphiphilic pocket near Cys214 (Figure 37B). Considering the solvent-accessible nature of this region and the known tendency of polyphenols like quercetin to exhibit non-specific binding behaviors (often classified as PAINS), we interpret these poses not as high-affinity, specific lock-and-key binding, but rather as evidence supporting a model of non-covalent interfacial enrichment. This concept aligns with the known biophysical tendency of flavonoids to partition into the membrane-water interface, thereby increasing their local abundance near the channel surface relative to the bulk solution. Thus, the protective mechanism is likely driven by a high local concentration of antioxidant moieties near the redox sensor, rather than a singular, high-affinity binding event. Consequently, we propose a proximal antioxidant defense mechanism: the transient association of these compounds with the channel surface may allow them to intercept ROS within the immediate microenvironment of Cys214.

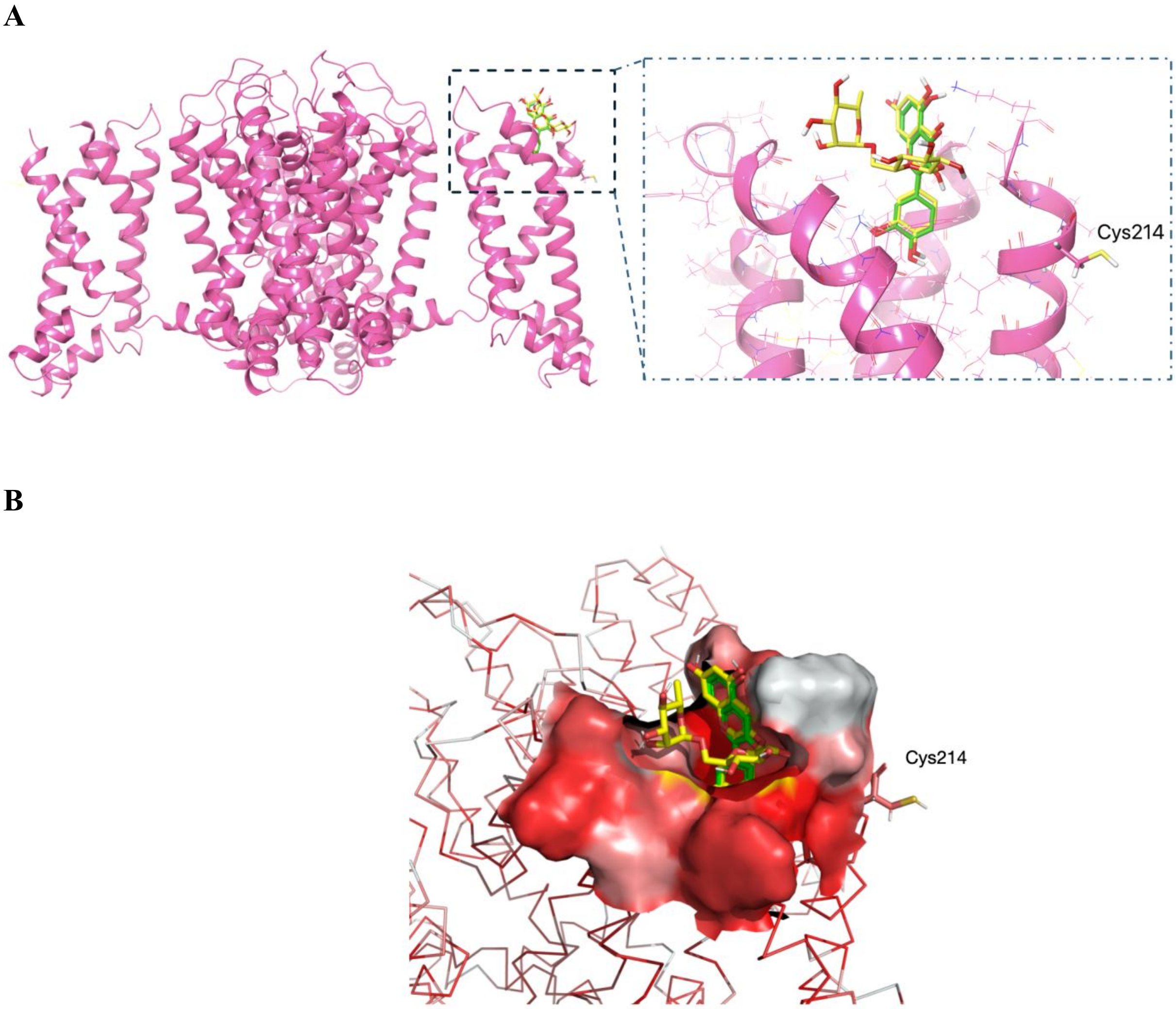

Figure 37. Molecular Docking of Rutin and Quercetin into the KCNQ1 Putative Binding Site. (A) The predicted binding poses of rutin (yellow sticks) and quercetin (green sticks) in the KCNQ1 channel (pink cartoon). The enlarged view provides a detailed view of the ligand proximity to the critical Cys214 residue (highlighted as sticks). (B) The binding pocket surface is colored by hydrophobicity (red: hydrophobic, white: neutral). This view illustrates that both ligands are situated within a predominantly hydrophobic pocket, which stabilizes their interaction near Cys214.

While this structural model provides a plausible mechanistic link between the observed systemic antioxidant capacity and specific channel protection, definitive verification of this local interaction awaits future site-directed mutagenesis studies. The predicted docking score for rutin was -6.5 kcal/mol, and for quercetin was -6.4 kcal/mol. While these scores indicate a lower affinity compared to the deep-pocket binding observed for activators (Section 4.4), they are consistent with a transient, surface-associated interaction typical of antioxidant shielding. A detailed analysis of the docking poses suggests that the ligands are primarily stabilized by insertion into a predominantly nonpolar but mixed (hydrophobic/polar) pocket, as visualized in Figure 37B. The aromatic scaffolds of both quercetin and rutin are positioned within this pocket, which is lined with residues including nonpolar side chains (e.g., Phe157, Trp158, Ile230, Val211, and Leu213) and polar contributors (e.g., Thr153 and Ser217). These residues stabilize the ligands through significant van der Waals forces. The observed binding affinities are attributed to the shape complementarity and the favorable hydrophobic environment of the binding site near Cys214.

The results suggest a potential dual-protection mechanism. While the biochemical assays confirm the systemic ROS-scavenging capacity, the molecular docking provides a theoretical framework for a complementary local effect. By occupying a solvent-exposed pocket near Cys214, flavonoids such as rutin may position themselves adjacent to this redox-sensitive residue. We emphasize that this is not a decisive conclusion, but a structure-based hypothesis linking macroscopic antioxidant efficacy to specific molecular interactions on the channel surface. This hypothesis further suggests that *E. ulmoides* flavonoids may bind to a surface region in the vicinity of Cys214 on KCNQ1. Notably, while both flavonoids exhibit similar docking scores, additional glycoside moiety of rutin may provide enhanced solubility and bioavailability compared to quercetin, potentially influencing their pharmacokinetics *in vivo*, though this requires further experimental elucidation. In addition to van der Waals interactions, the aromatic rings of these compounds may participate in π-π stacking with residues like Phe157 and Trp158, further stabilizing the complex and potentially influencing the local microenvironment near Cys214.

In conclusion, these results support an integrative framework combining systemic scavenging with potential local shielding. The high phenolic content and FRAP activity (wet-lab) confirm the chemical capacity for systemic protection, while the docking results (*in silico*) provide a complementary structural rationale, suggesting that its key constituents (rutin and quercetin) possess the structural complementarity to bind near the redox-sensitive Cys214. Although definitive confirmation of this local interaction requires future site-directed mutagenesis, this study establishes a coherent structure-activity relationship linking traditional efficacy to molecular targets. Importantly, for quercetin, previous studies have characterized quercetin as a KCNQ1 activator, engaging a hydrophobic pocket within the transmembrane domain (as discussed in Section 4.4). In contrast, the binding mode of quercetin identified in this section involves a distinct, solvent-exposed region near Cys214. This suggests that quercetin may possess a unique pharmacological characteristics, with the potential to involve spatially separated regions of the channel. Such multi-site investigation implies that flavonoid molecules could be optimized to achieve a synergistic effect: allosteric activation from the membrane phase and structural protection from the extracellular environment.

Concluding Remarks

This dissertation integrates computational biophysics, structural modeling, and biochemical assays to investigate the complex structure-function relationships of the KCNQ1 channel, providing novel insights into its regulation, pathogenic mechanisms, and pharmacological targeting.

We firstly established that the electrostatic landscape of the channel pore is a critical determinant of ligand specificity and function. Comparative modeling of KCNQ1-KCNE1 and KCNQ1-KCNE3 complexes demonstrated that the dual regulatory effects of Mallotoxin (MTX) are determined by subunit-specific electrostatic potentials (ESP). In KCNQ1-KCNE3 complex, a unique central region with high positive ESP facilitates the attraction of anionic MTX into the pore, leading to occlusion and inhibition. Conversely, the absence of this central positive potential in KCNQ1-KCNE1 redirects MTX to a peripheral site, where it stabilizes the open state and enhances current. This finding highlights the role of auxiliary subunits in modulating the inner cavity environment to determine pharmacological effect.

To address an unresolved structural region, we addressed a significant structural gap in the KCNQ1 cryo-EM data regarding the intracellular C-terminal domain. By combining electron density-guided modeling with AlphaFold predictions, we proposed a novel "domain-swapped" topology for the previously unresolved HC-HD linker. This model, characterized by an extended HD helix and inter-subunit connectivity, resolves the density discontinuities observed in experimental maps of cryo-EM structure. Importantly, this topology places known phosphorylation sites (S571, S577) on the solvent-accessible surface, providing a structural rationale for their accessibility to cytosolic kinases and regulatory partners like calmodulin and Yotiao.

At the mechanistic level, molecular dynamics (MD) simulations provided a comprehensive atomic-level explanation for the loss-of-function phenotypes in LQT1-associated mutations (D242N and R243H). Our analysis revealed that these mutations operate through distinct biophysical mechanisms despite their proximity. The D242N mutation enhances local electrostatic interactions with PIP_2, leading to an electrostatically-locked state that increases the energy barrier for voltage sensor activation. In contrast, the R243H mutation disrupts the critical salt-bridge network, resulting in structural decoupling between the VSD and the pore, characterized by increased entropic fluctuations and a rugged free-energy landscape. These results highlight that LQT1 pathogenicity can arise from excessive rigidity or excessive flexibility, suggesting the necessary for genotype-specific pharmacological strategies.

In terms of therapeutic translation, dual modulatory modes targeting both channel activation and oxidative protection were explored. We validated that natural compounds (tanshinone IIA, quercetin, and resveratrol) can stably occupy the ML277 activator pocket, with tanshinone IIA exhibiting superior stability driven by a network of polar and hydrophobic interactions. Complementing this direct modulation, biochemical screening identified *E. ulmoides* as a rich antioxidant source. Molecular docking of its key constituents, rutin and quercetin, suggested a mechanism of localized antioxidant shielding, where these flavonoids bind transiently to a surface pocket near the redox-sensitive Cys214. This implies a synergistic therapeutic potential where compounds may simultaneously enhance channel gating and protect against oxidative modification.

In conclusion, this work provides a multi-scale structural framework for understanding KCNQ1 physiology and pathology. By defining the atomic determinants of ligand selectivity, linker topology, and mutational dysfunction, these findings lay the groundwork for the rational design of next-generation modulators that are not only potent but also mechanism-specific for the treatment of cardiac arrhythmias.

Conclusions

1. The different effects of mallotoxin (MTX**)** on KCNQ1/KCNE1 and KCNQ1/KCNE3 complexes are explained by differences in the distribution of electrostatic potential in the inner cavity of the channel. The computational analysis suggests that the negatively charged MTX molecule preferentially binds to a region of high positive electrostatic potential present in KCNQ1-KCNE3 but absent in KCNQ1-KCNE1, providing a structural rationale for the observed inhibitory versus activating effects.

2. The structural model of the HC-HD linker in the KCNQ1 channel was constructed using modern molecular modeling algorithms and cryo-EM electron density mapping (EMD-20966). This study revealed an unprecedented domain displacement, specifically a 90° rotation of the HD tetrameric coiled-coil relative to the HC coiled-coil.

3. PCA of 100-nanosecond molecular dynamics (MD) trajectories for KCNQ1 channel molecules in native and mutant forms containing the pathogenic amino acid substitutions D242N and R243H revealed distinct conformational behavior patterns. Unlike the compact fluctuations observed in the native form, the D242N and R243H mutant forms exhibited greater flexibility. The same applies to Gibbs free energy landscapes derived from RMSD and Rg values.

4. For natural KCNQ1 channel activators including quercetin, tanshinone IIA, and resveratrol, molecular docking has identified potential binding sites. The primary binding site is located in a pocket formed by the S4-S5 helical linker, the S5 helix of one subunit, and the S6' helix of the adjacent subunit. This site corresponds to the binding site of the ML277 activator described in the literature, for which the spatial structure of the KCNQ1 channel complex is known, suggesting a similar activation mechanism.

5. Among the 9 plant extracts studied, *E. ulmoides* extract demonstrated the highest total phenolic content, the strongest iron-reducing capacity, and the most potent lipid peroxidation inhibitory activity. The molecular mechanism of *E. ulmoides* extract's protective effect on KCNQ1 channel involves its key antioxidant components, rutin and quercetin, which associate with the region surrounding the redox-sensitive Cys214 residue, potentially providing a localized antioxidant protection.

Acknowledgments

It is with the deepest gratitude that I wish to thank my supervisor, Professor Valery Novoseletsky. He was not just my supervisor, but a true mentor. I am deeply thankful for his thorough guidance, his extraordinary patience, and his constant encouragement that guided me forward, one step at a time. I will always remember our tireless discussions on the most challenging research problems, which took place in offices, libraries, and computer labs, both in Moscow and in Shenzhen. From him, I learned that to be a true scientist requires more than just knowledge. It requires passion, a strong commitment to rigor, and a spirit of giving without expectation of return. It was through our collaborative research and countless in-depth discussions on scientific questions that I truly came to understand the challenges and joys in creative research. The spirit of research he has passed on to me is a priceless inheritance.

I would also like to express my sincere gratitude to Professor Adil Bayzhumanov and Professor Maksimov for their expert guidance with the antioxidant capacity experiments. I am thankful for Professor Andrey V. Moiseenko's valuable help on building the model of KCNQ1 HC-HD linker. I am also grateful to Professor Olga Sokolova and Professor Andrey Kitashov for their help with the application for Shenzhen supercomputing resources. My special thanks go to Professor Jiangtao Guo from Zhejiang University for his generosity in sharing the original KCNQ1 Cryo-EM density map data.

This doctoral journey became infinitely more meaningful and fulfilling thanks to my friends. I want to thank my dear friends Dr. Zhang QY, and Wei YC, Isabella D and Sandycai, for the years of help, encouragement, and support. I am also deeply grateful for a friendship of more than 15 years with Dr. Guan Jingyi and Dr. Xie Miner, whose wise and practical advice has guided me in both research and life itself.

These past five years have been a transformative chapter in my life. There were many difficult moments, but the happiness was always greater. I feel so lucky for the people I've met, for the chance to pursue research that I was passionate about, and for the person I've become along the way. I will carry the spirit of curiosity and truth-seeking with me always as I step bravely into the future.

Life brings tears, smiles and memories. The tears will dry; the smiles will fade; but the memories will last a lifetime.

List of publications on the topic of the dissertation in peer-reviewed scientific journals indexed in the core database of the Russian Science Citation Index "eLibrary Science Index", recommended for defense in the Dissertation Council of Moscow State University in the specialty 1.5.2 Biophysics (biological sciences)

(the impact factor of the journal, the volume of publications in printed sheets/the author's contribution in printed sheets are given in parentheses):

1. **Mai L.**, Novoseletsky V. Investigating Dual Modulatory Role of Mallotoxin on KCNQ1-KCNE Complexes Using Molecular Modeling // Biochemistry (Moscow), Supplement Series A: Membrane and Cell Biology. — 2025. — Vol. 19, №2. — pp. 188–193. **(IF 0.336** (SJR)**, 0.6 / 0.4) EDN FWXEOR**
2. Li B., Karlova M.G., Zhang H., Pustovit O.B., **Mai L.**; Novoseletsky V.N., Podolyak D., Zaklyazminskaya E.V., Abramochkin D.V., Sokolova O.S. A mutation in the cardiac Kv7.1 channel possibly disrupts interactions with Yotiao protein // Biochemical and Biophysical Research Communications. — 2024. — Vol. 714, — P.149947. **(IF 0.748** (SJR)**, 0.8 / 0.1) EDN: JRGAUI**
3. Bayzhumanov A.A., **Mai L.,** Yusipovich A.I., Maksimov G.V. Antioxidant Activity of Certain Aquatic Extracts Used in Traditional Chinese Medicine //Moscow University Biological Sciences Bulletin. — 2022. — Vol. 77, — pp. 13–17 **(IF 0.161** (SJR)**, 0,6 / 0.1) EDN: OPUDJT**

Other publications on the topic of the dissertation:

4. Kravchuk E.V., **Mai L.**, Moiseenko A.V., Novoseletsky V.N., Sokolova O.S. Structural analysis of KCNQ1 channel distal C-terminus based on cryogenic electron microscopy and molecular modeling data // Microscopy and Microanalysis. — 2024. — P. ozae044-373. **(IF 0.465** (SJR)**, 0,1 / 0.05) EDN: WJWQIA**

LIST OF ABBREVIATIONS

CaM - Calmodulin

Cryo-EM - Cryo-Electron Microscopy

E-M - electromechanical

ESP - Electrostatic Potential

FEL - Free Energy Landscape

FRAP - Ferric Reducing Antioxidant Power

GAE - Gallic Acid Equivalents

HC - Helix C (distal C-terminus)

HD - Helix D (distal C-terminus)

IKs - Slow Delayed Rectifier Potassium Current

KCNE - Potassium Voltage-Gated Channel Subfamily E Regulatory Subunit

KCNQ1 - Potassium Voltage-Gated Channel Subfamily Q Member 1 (Kv7.1)

LOO• - lipid peroxyl radicals

LQT1 - Long QT Syndrome Type 1

MD - Molecular Dynamics

MDA - Malondialdehyde

MFH - Medicine and Food Homology

MTX - Mallotoxin

NPT - Constant Number of Particles, Pressure, and Temperature

NVT - Constant Number of Particles, Volume, and Temperature

PCA - Principal Component Analysis

PD - Pore Domain

PIP$_2$ - Phosphatidylinositol 4,5-bisphosphate

PKA - Protein Kinase A

PME - Particle Mesh Ewald

POPC - 1-palmitoyl-2-oleoyl-sn-glycero-3-phosphocholine

POPG - 1-palmitoyl-2-oleoyl-sn-glycero-3-phospho-(1'-rac-glycerol)

PP1 - Protein Phosphatase 1

PTMs - post-translational modifications

PUFA - polyunsaturated fatty acids

Rg - Radius of Gyration

RMSD - Root Mean Square Deviation

RMSF - Root Mean Square Fluctuation

ROS - Reactive Oxygen Species

SASA - Solvent Accessible Surface Area

TBA - Thiobarbituric Acid

TBARS - Thiobarbituric Acid Reactive Substances

TCM - Traditional Chinese Medicine

TPC - Total Phenolic Content

TPTZ - 2,4,6-tripyridyl-s-triazine

VSD - Voltage-Sensing Domain

WT - wild-type

References

1. Nerbonne JM, Kass RS. Molecular physiology of cardiac repolarization / Nerbonne JM // Physiol Rev. — 2005. — Vol. 85. — P. 1205-1253.

2. Sanguinetti MC, Curran ME, Zou A, et al. Coassembly of KVLQT1 and minK (IsK) proteins to form cardiac IKS potassium channel / Sanguinetti MC // Nature. — 1996. — Vol. 384. — P. 80-83.

3. Schwartz PJ, Stramba-Badiale M, Crotti L, et al. Prevalence of the congenital long-QT syndrome / Schwartz PJ // Circulation. — 2009. — Vol. 120. — P. 1761-1767.

4. Kunzelmann K, Mall M. Electrolyte transport in the mammalian colon: mechanisms and implications for disease / Kunzelmann K // Physiol Rev. — 2002. — Vol. 82. — P. 245-289.

5. Grahammer F, Wittekindt OH, Nitschke R, et al. The cardiac K+ channel KCNQ1 is essential for gastric acid secretion / Grahammer F // Gastroenterology. — 2001. — Vol. 120. — P. 1363-1371.

6. Melman YF, Domènech A, de la Luna S, et al. Structural determinants of KvLQT1 control by the KCNE family of proteins / Melman YF // J Biol Chem. — 2001. — Vol. 276. — P. 6439-6444.

7. Mandala VS, MacKinnon R. The membrane electric field regulates the PIP2-binding site to gate the KCNQ1 channel / Mandala VS // Proc Natl Acad Sci U S A. — 2023. — Vol. 120(21). — P. e2301985120.

8. Zhang H, Craciun LC, Mirshahi T, et al. PIP2 activates KCNQ channels, and its hydrolysis underlies receptor-mediated inhibition of M currents / Zhang H // Neuron. — 2003. — Vol. 37. — P. 963-975.

9. Wiener R, Haitin Y, Shamgar L, et al. The KCNQ1 (Kv7.1) COOH terminus, a multitiered scaffold for subunit assembly and protein interaction / Wiener R // J Biol Chem. — 2008. — Vol. 283. — P. 5815-5830.

10. Sun J, MacKinnon R. Cryo-EM structure of a KCNQ1/CaM complex reveals insights into congenital long QT syndrome / Sun J // Cell. — 2017. — Vol. 169. — P. 1042-1050.

11. Marx SO, Kurokawa J, Reiken S, et al. Requirement of a macromolecular signaling complex for β adrenergic receptor modulation of the KCNQ1-KCNE1 potassium channel / Marx SO // Science. — 2002. — Vol. 295. — P. 496-499.

12. Li Y, Chen L, Kass RS, et al. The A-kinase anchoring protein Yotiao facilitates complex formation between adenylyl cyclase type 9 and the IKs potassium channel in heart / Li Y // J Biol Chem. — 2012. — Vol. 287. — P. 29815-29824.

13. Sun J, MacKinnon R. Structural basis of human KCNQ1 modulation and gating / Sun J // Cell. — 2020. — Vol. 180. — P. 340-347.

14. Ma D, Zhong L, Yan Z, et al. Structural mechanisms for the activation of human cardiac KCNQ1 channel by electro-mechanical coupling enhancers / Ma D // Proc Natl Acad Sci U S A. — 2022. — Vol. 119(45). — P. e2207067119.

15. Willegems K, Eldstrom J, Kyriakis E, et al. Structural and electrophysiological basis for the modulation of KCNQ1 channel currents by ML277 / Willegems K // Nat Commun. — 2022. — Vol. 13. — P. 3760.

16. Matschke V, Piccini I, Schubert J, et al. The natural plant product rottlerin activates Kv7.1/KCNE1 channels / Matschke V // Cell Physiol Biochem. — 2016. — Vol. 40. — P. 1549-1558.

17. De Silva AM, Manville RW, Abbott GW. Deconstruction of an African folk medicine uncovers a novel molecular strategy for therapeutic potassium channel activation / De Silva AM // Sci Adv. — 2018. — Vol. 4. — P. eaav0824.

18. Li B, Karlova M, Zhang H, et al. A mutation in the cardiac KV7.1 channel possibly disrupts interaction with Yotiao protein / Li B // Biochem Biophys Res Commun. — 2024. — Vol. 714. — P. 149947.

19. Chen L, Marquardt ML, Tester DJ, et al. Mutation of an A-kinase-anchoring protein causes long-QT syndrome / Chen L // Proc Natl Acad Sci U S A. — 2007. — Vol. 104. — P. 20990-20995.

20. Moreno C, Oliveras A, Bartolucci C, et al. D242N, a KV7.1 LQTS mutation uncovers a key residue for IKs voltage dependence / Moreno C // J Mol Cell Cardiol. — 2017. — Vol. 110. — P. 61-69.

21. Park K-H, Piron J, Dahimene S, et al. Impaired KCNQ1–KCNE1 and phosphatidylinositol-4,5-bisphosphate interaction underlies the long QT syndrome / Park K-H // Circ Res. — 2005. — Vol. 96. — P. 730-739.

22. Hou P, Shi J, White KM, et al. ML277 specifically enhances the fully activated open state of KCNQ1 by modulating VSD-pore coupling / Hou P // Elife. — 2019. — Vol. 8. — P. e48576.

23. Mattmann ME, Yu H, Lin Z, et al. Identification of (R)-N-(4-(4-methoxyphenyl)thiazol-2-yl)-1-tosylpiperidine-2-carboxamide, ML277, as a novel, potent and selective Kv7.1 (KCNQ1) potassium channel activator / Mattmann ME // Bioorg Med Chem Lett. — 2012. — Vol. 22. — P. 5936-5941.

24. Shang Q, Xu H, Huang L. Tanshinone IIA: a promising natural cardioprotective agent / Shang Q // Evid Based Complement Alternat Med. — 2012. — Vol. 2012. — P. 716459.

25. Sun D-D, Wang H-C, Wang X-B, et al. Tanshinone IIA: a new activator of human cardiac KCNQ1/KCNE1 (IKs) potassium channels / Sun D-D // Eur J Pharmacol. — 2008. — Vol. 590. — P. 317-321.

26. Li J, Hu D, Song X, et al. The role of biologically active ingredients from natural drug treatments for arrhythmias in different mechanisms / Li J // Biomed Res Int. — 2017. — Vol. 2017. — P. 1-10.

27. Redford KE, Abbott GW. The ubiquitous flavonoid quercetin is an atypical KCNQ potassium channel activator / Redford KE // Commun Biol. — 2020. — Vol. 3. — P. 356.

28. Kerst G, Brousos H, Schreiber R, et al. The oxidant thimerosal modulates gating behavior of KCNQ1 by interaction with the channel outer shell / Kerst G // J Membr Biol. — 2002. — Vol. 186. — P. 89-100.

29. Wang H-S, Pan Z, Shi W, et al. KCNQ2 and KCNQ3 potassium channel subunits: molecular correlates of the M-channel / Wang H-S // Science. — 1998. — Vol. 282. — P. 1890-1893.

30. Li T, Wu K, Yue Z, et al. Structural basis for the modulation of human KCNQ4 by small-molecule drugs / Li T // Mol Cell. — 2021. — Vol. 81. — P. 25-37.

31. Schmitt N, Schwarz M, Peretz A, et al. A recessive C-terminal Jervell and Lange-Nielsen mutation of the KCNQ1 channel impairs subunit assembly / Schmitt N // EMBO J. — 2000. — Vol. 19. — P. 332-340.

32. Li X, Zhang Q, Guo P, et al. Molecular basis for ligand activation of the human KCNQ2 channel / Li X // Cell Res. — 2021. — Vol. 31. — P. 52-61.

33. Delmas P, Brown DA. Pathways modulating neural KCNQ/M (Kv7) potassium channels / Delmas P // Nat Rev Neurosci. — 2005. — Vol. 6. — P. 850-862.

34. Huang H, Trussell LO. KCNQ5 channels control resting properties and release probability of a synapse / Huang H // Nat Neurosci. — 2011. — Vol. 14. — P. 840-847.

35. Tan A, Costi S, Morris LS, et al. Effects of the KCNQ channel opener ezogabine on functional connectivity of the ventral striatum and clinical symptoms in patients with major depressive disorder / Tan A // Mol Psychiatry. — 2020. — Vol. 25. — P. 1323-1333.

36. Gollasch M, Welsh DG, Schubert R. Perivascular adipose tissue and the dynamic regulation of Kv7 and Kir channels: implications for resistant hypertension / Gollasch M // Microcirculation. — 2018. — Vol. 25. — P. e12434.

37. Kasuya G, Zempo B, Yamamoto Y, et al. Identification of KCNE6, a new member of the KCNE family of potassium channel auxiliary subunits / Kasuya G // Commun Biol. — 2024. — Vol. 7. — P. 1662.

38. Dixit G, Dabney-Smith C, Lorigan GA. The membrane protein KCNQ1 potassium ion channel: functional diversity and current structural insights / Dixit G // Biochim Biophys Acta Biomembr. — 2020. — Vol. 1862. — P. 183148.

39. Kanki H, Kupershmidt S, Yang T, et al. A structural requirement for processing the cardiac K+ channel KCNQ1 / Kanki H // J Biol Chem. — 2004. — Vol. 279. — P. 33976-33983.

40. Chen J, Zheng R, Melman YF, et al. Functional interactions between KCNE1 C-terminus and the KCNQ1 channel / Chen J // PLoS One. — 2009. — Vol. 4. — P. e5143.

41. Zheng R, Thompson K, Obeng-Gyimah E, et al. Analysis of the interactions between the C-terminal cytoplasmic domains of KCNQ1 and KCNE1 channel subunits / Zheng R // Biochem J. — 2010. — Vol. 428. — P. 75-84.

42. Kapplinger JD, Tseng AS, Salisbury BA, et al. Enhancing the predictive power of mutations in the C-terminus of the KCNQ1-encoded Kv7.1 voltage-gated potassium channel / Kapplinger JD // J Cardiovasc Transl Res. — 2015. — Vol. 8. — P. 187-197.

43. Aromolaran AS, Subramanyam P, Chang DD, et al. LQT1 mutations in KCNQ1 C-terminus assembly domain suppress IKs using different mechanisms / Aromolaran AS // Cardiovasc Res. — 2014. — Vol. 104. — P. 501-511.

44. Kashiwa A, Itoh H, Makiyama T, et al. Clinical characterization of type 1 long QT syndrome caused by C-terminus Kv7.1 variants / Kashiwa A // Heart Rhythm. — 2024. — Vol. 21. — P. 1113-1120.

45. Thompson E, Eldstrom J, Westhoff M, et al. cAMP-dependent regulation of IKs single-channel kinetics / Thompson E // J Gen Physiol. — 2017. — Vol. 149. — P. 781-798.

46. Giudicessi JR, Ackerman MJ. Potassium-channel mutations and cardiac arrhythmias—diagnosis and therapy / Giudicessi JR // Nat Rev Cardiol. — 2012. — Vol. 9. — P. 319-332.

47. Cui C, Zhao L, Kermani AA, et al. Mechanisms of KCNQ1 gating modulation by KCNE1/3 for cell-specific function / Cui C // Cell Res. — 2025. — Vol. 35. — P. 876-886.

48. Barhanin J, Lesage F, Guillemare E, et al. KvLQT1 and IsK (minK) proteins associate to form the IKS cardiac potassium current / Barhanin J // Nature. — 1996. — Vol. 384. — P. 78-80.

49. Hou P, Kang PW, Kongmeneck AD, et al. Two-stage electro-mechanical coupling of a KV channel in voltage-dependent activation / Hou P // Nat Commun. — 2020. — Vol. 11. — P. 676.

50. Zaydman MA, Kasimova MA, McFarland K, et al. Domain-domain interactions determine the gating, permeation, pharmacology, and subunit modulation of the IKs ion channel / Zaydman MA // Elife. — 2014. — Vol. 3. — P. e03606.

51. Franqueza L, Lin M, Splawski I, et al. Long QT syndrome-associated mutations in the S4-S5 linker of KvLQT1 potassium channels modify gating and interaction with minK subunits / Franqueza L // J Biol Chem. — 1999. — Vol. 274. — P. 21063-21070.

52. Schroeder BC, Waldegger S, Fehr S, et al. A constitutively open potassium channel formed by KCNQ1 and KCNE3 / Schroeder BC // Nature. — 2000. — Vol. 403. — P. 196-199.

53. Kroncke BM, Van Horn WD, Smith J, et al. Structural basis for KCNE3 modulation of potassium recycling in epithelia / Kroncke BM // Sci Adv. — 2016. — Vol. 2. — P. e1501228.

54. Barro-Soria R, Perez ME, Larsson HP. KCNE3 acts by promoting voltage sensor activation in KCNQ1 / Barro-Soria R // Proc Natl Acad Sci U S A. — 2015. — Vol. 112. — P. E7286-E7292.

55. Melman YF, Krumerman A, McDonald T V. A single transmembrane site in the KCNE-encoded proteins controls the specificity of KvLQT1 channel gating / Melman YF // J Biol Chem. — 2002. — Vol. 277. — P. 25187-25194.

56. Ohno S, Toyoda F, Zankov DP, et al. Novel KCNE3 mutation reduces repolarizing potassium current and associated with long QT syndrome / Ohno S // Hum Mutat. — 2009. — Vol. 30. — P. 557-563.

57. Lundby A, Ravn LS, Svendsen JH, et al. KCNE3 mutation V17M identified in a patient with lone atrial fibrillation / Lundby A // Cell Physiol Biochem. — 2008. — Vol. 21. — P. 47-54.

58. Alzamora R, O'Mahony F, Bustos V, et al. Sexual dimorphism and oestrogen regulation of KCNE3 expression modulates the functional properties of KCNQ1 K+ channels / Alzamora R // J Physiol. — 2011. — Vol. 589. — P. 5091-5107.

59. Sachyani D, Dvir M, Strulovich R, et al. Structural basis of a Kv7.1 potassium channel gating module: studies of the intracellular C-terminal domain in complex with calmodulin / Sachyani D // Structure. — 2014. — Vol. 22. — P. 1582-1594.

60. Ghosh S, Nunziato DA, Pitt GS. KCNQ1 assembly and function is blocked by long-QT syndrome mutations that disrupt interaction with calmodulin / Ghosh S // Circ Res. — 2006. — Vol. 98. — P. 1048-1054.

61. Makita N, Yagihara N, Crotti L, et al. Novel calmodulin mutations associated with congenital arrhythmia susceptibility / Makita N // Circ Cardiovasc Genet. — 2014. — Vol. 7. — P. 466-474.

62. Walsh KB, Kass RS. Regulation of a heart potassium channel by protein kinase A and C / Walsh KB // Science. — 1988. — Vol. 242. — P. 67-69.

63. Collins KB, Scott JD. Phosphorylation, compartmentalization, and cardiac function / Collins KB // IUBMB Life. — 2023. — Vol. 75. — P. 353-369.

64. Li Y, Baldwin TA, Wang Y, et al. Loss of type 9 adenylyl cyclase triggers reduced phosphorylation of Hsp20 and diastolic dysfunction / Li Y // Sci Rep. — 2017. — Vol. 7. — P. 5522.

65. Terrenoire C, Houslay MD, Baillie GS, et al. The cardiac IKs potassium channel macromolecular complex includes the phosphodiesterase PDE4D3 / Terrenoire C // J Biol Chem. — 2009. — Vol. 284. — P. 9140-9146.

66. Wang X, Fitts RH. Cardiomyocyte slowly activating delayed rectifier potassium channel: regulation by exercise and β-adrenergic signaling / Wang X // J Appl Physiol. — 2020. — Vol. 128. — P. 1177-1185.

67. Manville RW, Abbott GW. Ancient and modern anticonvulsants act synergistically in a KCNQ potassium channel binding pocket / Manville RW // Nat Commun. — 2018. — Vol. 9. — P. 3845.

68. Guan X, Li Q, Yan J. Relationship between auxiliary gamma subunits and mallotoxin on BK channel modulation / Guan X // Sci Rep. — 2017. — Vol. 7. — P. 42240.

69. Redford KE, Abbott GW. KCNQ potassium channels as targets of botanical folk medicines / Redford KE // Annu Rev Pharmacol Toxicol. — 2022. — Vol. 62. — P. 447-464.

70. Lübke M, Schreiber JA, Le Quoc T, et al. Rottlerin: structure modifications and KCNQ1/KCNE1 ion channel activity / Lübke M // ChemMedChem. — 2020. — Vol. 15. — P. 1078-1088.

71. Zakharov SI, Morrow JP, Liu G, et al. Activation of the BK (SLO1) potassium channel by mallotoxin / Zakharov SI // J Biol Chem. — 2005. — Vol. 280. — P. 30882-30887.

72. Kam MK, Park J-Y, Yun GH, et al. Rottlerin enhances the autophagic degradation of phosphorylated tau in neuronal cells / Kam MK // Mol Neurobiol. — 2024. — Vol. 61. — P. 9633-9645.

73. Nakano Y, Shimizu W. Genetics of long-QT syndrome / Nakano Y // J Hum Genet. — 2016. — Vol. 61. — P. 51-55.

74. Iwahashi Y, Toyama Y, Imai S, et al. Conformational equilibrium shift underlies altered K+ channel gating as revealed by NMR / Iwahashi Y // Nat Commun. — 2020. — Vol. 11. — P. 5168.

75. Curran ME, Splawski I, Timothy KW, et al. A molecular basis for cardiac arrhythmia: HERG mutations cause long QT syndrome / Curran ME // Cell. — 1995. — Vol. 80. — P. 795-803.

76. Lubberding AF, Juhl CR, Skovhøj EZ, et al. Celebrities in the heart, strangers in the pancreatic beta cell: voltage-gated potassium channels Kv7.1 and Kv11.1 bridge long QT

syndrome with hyperinsulinaemia as well as type 2 diabetes / Lubberding AF // Acta Physiol (Oxf). — 2022. — Vol. 234(3). — P. e13781.

77. Yasuda K, Miyake K, Horikawa Y, et al. Variants in KCNQ1 are associated with susceptibility to type 2 diabetes mellitus / Yasuda K // Nat Genet. — 2008. — Vol. 40. — P. 1092-1097.

78. Ng MCY, Shriner D, Chen BH, et al. Meta-analysis of genome-wide association studies in African Americans provides insights into the genetic architecture of type 2 diabetes / Ng MCY // PLoS Genet. — 2014. — Vol. 10. — P. e1004517.

79. Preston P, Wartosch L, Günzel D, et al. Disruption of the K+ channel β-subunit KCNE3 reveals an important role in intestinal and tracheal Cl− transport / Preston P // J Biol Chem. — 2010. — Vol. 285. — P. 7165-7175.

80. Zheng W, Verlander JW, Lynch IJ, et al. Cellular distribution of the potassium channel KCNQ1 in normal mouse kidney / Zheng W // Am J Physiol Renal Physiol. — 2007. — Vol. 292. — P. F456-F466.

81. Zhou L, Köhncke C, Hu Z, et al. The KCNE2 potassium channel β subunit is required for normal lung function and resilience to ischemia and reperfusion injury / Zhou L // FASEB J. — 2019. — Vol. 33. — P. 9762-9774.

82. Heitzmann D, Koren V, Wagner M, et al. KCNE beta subunits determine pH sensitivity of KCNQ1 potassium channels / Heitzmann D // Cell Physiol Biochem. — 2007. — Vol. 19. — P. 21-32.

83. Nakajo K, Kasuya G. Modulation of potassium channels by transmembrane auxiliary subunits via voltage-sensing domains / Nakajo K // Physiol Rep. — 2024. — Vol. 12. — P. e15980.

84. Suh B-C, Hille B. Recovery from muscarinic modulation of M current channels requires phosphatidylinositol 4,5-bisphosphate synthesis / Suh B-C // Neuron. — 2002. — Vol. 35. — P. 507-520.

85. Ford CP, Stemkowski PL, Smith PA. Possible role of phosphatidylinositol 4,5, bisphosphate in luteinizing hormone releasing hormone-mediated M-current inhibition in bullfrog sympathetic neurons / Ford CP // Eur J Neurosci. — 2004. — Vol. 20. — P. 2990-2998.

86. Hou P, Eldstrom J, Shi J, et al. Inactivation of KCNQ1 potassium channels reveals dynamic coupling between voltage sensing and pore opening / Hou P // Nat Commun. — 2017. — Vol. 8. — P. 1730.

87. Chouabe C. Novel mutations in KvLQT1 that affect Iks activation through interactions with Isk / Chouabe C // Cardiovasc Res. — 2000. — Vol. 45. — P. 971-980.

88. Packer L. Oxygen radicals in biological systems / Packer L. — Elsevier, 1994. — Vol. 233.

89. Koppenol WH. Chapter 1 - Chemistry of iron and copper in radical reactions / Koppenol WH // New Comprehensive Biochemistry / ed. by Rice-Evans CA, Burdon RH. — Elsevier, 1994. — Vol. 28. — P. 3-24.

90. Matés JM, Sánchez-Jiménez F. Antioxidant enzymes and their implications in pathophysiologic processes / Matés JM // Front Biosci. — 1999. — Vol. 4. — P. 339-345.

91. Johnson LJ, Susan LM, Kruskall LJ. The antioxidants-vitamin C, vitamin E, selenium, and carotenoids / Johnson LJ // J Agromedicine. — 2003. — Vol. 9. — P. 65-82.

92. Ooi L, Gigout S, Pettinger L, et al. Triple cysteine module within M-type K+ channels mediates reciprocal channel modulation by nitric oxide and reactive oxygen species / Ooi L // J Neurosci. — 2013. — Vol. 33. — P. 6041-6046.

93. Abdullaeva OS, Sahalianov I, Silverå Ejneby M, et al. Faradaic pixels for precise hydrogen peroxide delivery to control M-type voltage-gated potassium channels / Abdullaeva OS // Adv Sci (Weinh). — 2022. — Vol. 9. — P. 2103132.

94. Gamper N, Zaika O, Li Y, et al. Oxidative modification of M-type K+ channels as a mechanism of cytoprotective neuronal silencing / Gamper N // EMBO J. — 2006. — Vol. 25. — P. 4996-5004.

95. Hilgers RHP, Das KC. Redox regulation of K+ channel: role of thioredoxin / Hilgers RHP // Antioxid Redox Signal. — 2024. — Vol. 41. — P. 818-844.

96. Lu J, Holmgren A. The thioredoxin antioxidant system / Lu J // Free Radic Biol Med. — 2014. — Vol. 66. — P. 75-87.

97. Nordberg J, Arnér ESJ. Reactive oxygen species, antioxidants, and the mammalian thioredoxin system / Nordberg J // Free Radic Biol Med. — 2001. — Vol. 31. — P. 1287-1312.

98. Nuñez E, Jones F, Muguruza-Montero A, et al. Redox regulation of KV7 channels through EF3 hand of calmodulin / Nuñez E // Elife. — 2023. — Vol. 12. — P. e81961.

99. Asada K, Kurokawa J, Furukawa T. Redox- and calmodulin-dependent S-nitrosylation of the KCNQ1 channel / Asada K // J Biol Chem. — 2009. — Vol. 284. — P. 6014-6020.

100. Dutta D, Show S, Pal A, et al. The association of cysteine to thiomersal attenuates its apoptosis-mediated cytotoxicity in zebrafish / Dutta D // Chemosphere. — 2024. — Vol. 350. — P. 141070.

101. Bates A, Stowe RB, Travis EM, et al. The role of native cysteine residues in the oligomerization of KCNQ1 channels / Bates A // Biochem Biophys Res Commun. — 2023. — Vol. 659. — P. 34-39.

102. Asiamah I, Obiri SA, Tamekloe W, et al. Applications of molecular docking in natural products-based drug discovery / Asiamah I // Sci Afr. — 2023. — Vol. 20. — P. e01593.

103. Dias R, Filgueira De Azevedo W. Molecular docking algorithms / Dias R // Curr Drug Targets. — 2008. — Vol. 9. — P. 1040-1047.

104. Li J, Fu A, Zhang L. An overview of scoring functions used for protein-ligand interactions in molecular docking / Li J // Interdiscip Sci. — 2019. — Vol. 11. — P. 320-328.

105. Hollingsworth SA, Dror RO. Molecular dynamics simulation for all / Hollingsworth SA // Neuron. — 2018. — Vol. 99. — P. 1129-1143.

106. Shaw DE, Adams PJ, Azaria A, et al. Anton 3: twenty microseconds of molecular dynamics simulation before lunch / Shaw DE // Proceedings of the International Conference for High Performance Computing, Networking, Storage and Analysis. — 2021. — P. 1-11.

107. Sanbonmatsu KY, Tung C-S. High performance computing in biology: multimillion atom simulations of nanoscale systems / Sanbonmatsu KY // J Struct Biol. — 2007. — Vol. 157. — P. 470-480.

108. Li X, Yang Z, Chen Y, et al. Dissecting the molecular mechanisms of the co-aggregation of Aβ40 and Aβ42 peptides: a REMD simulation study / Li X // J Phys Chem B. — 2023. — Vol. 127. — P. 4050-4060.

109. Blumer O, Reuveni S, Hirshberg B. Combining stochastic resetting with metadynamics to speed-up molecular dynamics simulations / Blumer O // Nat Commun. — 2024. — Vol. 15. — P. 240.

110. Vant JW, Sarkar D, Nguyen J, et al. Exploring cryo-electron microscopy with molecular dynamics / Vant JW // Biochem Soc Trans. — 2022. — Vol. 50. — P. 569-581.

111. Kaur C, Kapoor HC. Anti-oxidant activity and total phenolic content of some Asian vegetables / Kaur C // Int J Food Sci Technol. — 2002. — Vol. 37. — P. 153-161.

112. Kırca A, Arslan E. Antioxidant capacity and total phenolic content of selected plants from Turkey / Kırca A // Int J Food Sci Technol. — 2008. — Vol. 43. — P. 2038-2046.

113. Prakash D, Samiksha S, Garima U, et al. Total phenol, antioxidant and free radical scavenging activities of some medicinal plants / Prakash D // Int J Food Sci Nutr. — 2007. — Vol. 58. — P. 18-28.

114. Sengul M, Yildiz H, Gungor N, et al. Total phenolic content, antioxidant and antimicrobial activities of some medicinal plants / Sengul M // Pak J Pharm Sci. — 2009. — Vol. 22.

115. Fu L, Xu B-T, Xu X-R, et al. Antioxidant capacities and total phenolic contents of 62 fruits / Fu L // Food Chem. — 2011. — Vol. 129(2). — P. 345-350.

116. Ainsworth EA, Gillespie KM. Estimation of total phenolic content and other oxidation substrates in plant tissues using Folin-Ciocalteu reagent / Ainsworth EA // Nat Protoc. — 2007. — Vol. 2. — P. 875-877.

117. Benzie IFF, Strain JJ. The ferric reducing ability of plasma (FRAP) as a measure of "antioxidant power": the FRAP assay / Benzie IFF // Anal Biochem. — 1996. — Vol. 239. — P. 70-76.

118. Benzie IFF, Szeto YT. Total antioxidant capacity of teas by the ferric reducing/antioxidant power assay / Benzie IFF // J Agric Food Chem. — 1999. — Vol. 47. — P. 633-636.

119. Benzie IFF, Devaki M. The ferric reducing/antioxidant power (FRAP) assay for non-enzymatic antioxidant capacity: concepts, procedures, limitations and applications / Benzie IFF // Measurement of Antioxidant Activity & Capacity: Recent Trends and Applications. — 2018. — P. 77-106.

120. Ou B, Huang D, Hampsch-Woodill M, et al. Analysis of antioxidant activities of common vegetables employing oxygen radical absorbance capacity (ORAC) and ferric reducing antioxidant power (FRAP) assays: a comparative study / Ou B // J Agric Food Chem. — 2002. — Vol. 50. — P. 3122-3128.

121. Ozgen M, Reese RN, Tulio AZ, et al. Modified 2, 2-azino-bis-3-ethylbenzothiazoline-6-sulfonic acid (ABTS) method to measure antioxidant capacity of selected small fruits and comparison to ferric reducing antioxidant power (FRAP) and 2, 2 '-diphenyl-1-picrylhydrazyl (DPPH) methods / Ozgen M // J Agric Food Chem. — 2006. — Vol. 54. — P. 1151-1157.

122. Pulido R, Bravo L, Saura-Calixto F. Antioxidant activity of dietary polyphenols as determined by a modified ferric reducing/antioxidant power assay / Pulido R // J Agric Food Chem. — 2000. — Vol. 48. — P. 3396-3402.

123. El-Beltagi HS, Mohamed HI. Reactive oxygen species, lipid peroxidation and antioxidative defense mechanism / El-Beltagi HS // Not Bot Horti Agrobot Cluj Napoca. — 2013. — Vol. 41. — P. 44-57.

124. Wang B, Wang Y, Zhang J, et al. ROS-induced lipid peroxidation modulates cell death outcome: mechanisms behind apoptosis, autophagy, and ferroptosis / Wang B // Arch Toxicol. — 2023. — Vol. 97. — P. 1439-1451.

125. Niki E, Yoshida Y, Saito Y, et al. Lipid peroxidation: mechanisms, inhibition, and biological effects / Niki E // Biochem Biophys Res Commun. — 2005. — Vol. 338. — P. 668-676.

126. Valgimigli L. Lipid peroxidation and antioxidant protection / Valgimigli L // Biomolecules. — 2023. — Vol. 13. — P. 1291.

127. Yin H, Xu L, Porter NA. Free radical lipid peroxidation: mechanisms and analysis / Yin H // Chem Rev. — 2011. — Vol. 111. — P. 5944-5972.

128. Zhang J, Stanley RA, Melton LD. Lipid peroxidation inhibition capacity assay for antioxidants based on liposomal membranes / Zhang J // Mol Nutr Food Res. — 2006. — Vol. 50. — P. 714-724.

129. Kristinova V, Mozuraityte R, Storrø I, et al. Antioxidant activity of phenolic acids in lipid oxidation catalyzed by different prooxidants / Kristinova V // J Agric Food Chem. — 2009. — Vol. 57. — P. 10377-10385.

130. Zhong H, Tang Z-Q, Li Y-F, et al. The evolution and significance of medicine and food homology / Zhong H // Acupunct Herb Med. — 2024. — Vol. 4. — P. 19-35.

131. Zhang X, Luo Y, Wei G, et al. Physicochemical and antioxidant properties of the degradations of polysaccharides from Dendrobium officinale and their suitable molecular weight range on inducing HeLa cell apoptosis / Zhang X // Evid Based Complement Alternat Med. — 2019. — Vol. 2019. — P. 4127360.

132. Boh B, Berovic M, Zhang J, et al. Ganoderma lucidum and its pharmaceutically active compounds / Boh B // Biotechnol Annu Rev. — 2007. — Vol. 13. — P. 265-301.

133. Zhu M, Chang Q, Wong LK, et al. Triterpene antioxidants from Ganoderma lucidum / Zhu M // Phytother Res. — 1999. — Vol. 13. — P. 529-531.

134. Chen W-C, Lai Y-S, Lin S-H, et al. Anti-depressant effects of Gastrodia elata Blume and its compounds gastrodin and 4-hydroxybenzyl alcohol, via the monoaminergic system and neuronal cytoskeletal remodeling / Chen W-C // J Ethnopharmacol. — 2016. — Vol. 182. — P. 190-199.

135. Jung JW, Yoon BH, Oh HR, et al. Anxiolytic-like effects of Gastrodia elata and its phenolic constituents in mice / Jung JW // Biol Pharm Bull. — 2006. — Vol. 29. — P. 261-265.

136. Kim H-J, Moon K-D, Oh S-Y, et al. Ether fraction of methanol extracts of Gastrodia elata, a traditional medicinal herb, protects against kainic acid-induced neuronal damage in the mouse hippocampus / Kim H-J // Neurosci Lett. — 2001. — Vol. 314. — P. 65-68.

137. He K, Song S, Zou Z, et al. The hypoglycemic and synergistic effect of loganin, morroniside, and ursolic acid isolated from the fruits of Cornus officinalis / He K // Phytother Res. — 2016. — Vol. 30. — P. 283-291.

138. Wang W, Sun F, An Y, et al. Morroniside protects human neuroblastoma SH-SY5Y cells against hydrogen peroxide-induced cytotoxicity / Wang W // Eur J Pharmacol. — 2009. — Vol. 613. — P. 19-23.

139. Yen G-C, Hsieh C-L. Antioxidant activity of extracts from Du-zhong (Eucommia ulmoides) toward various lipid peroxidation models in vitro / Yen G-C // J Agric Food Chem. — 1998. — Vol. 46. — P. 3952-3957.

140. Wu M, Zhuang Q, Lin J, et al. Enrichment of the flavonoid fraction from Eucommia ulmoides leaves by a liquid antisolvent precipitation method and evaluation of antioxidant activities in vitro and in vivo / Wu M // RSC Adv. — 2023. — Vol. 13. — P. 17406-17419.

141. Peng M, Zhou Y, Liu B. Biological properties and potential application of extracts and compounds from different medicinal parts (bark, leaf, staminate flower, and seed) of Eucommia ulmoides: a review / Peng M // Heliyon. — 2024. — Vol. 10. — P. e27870.

142. Cai R, Yang M, Shi Y, et al. Antifatigue activity of phenylethanoid-rich extract from Cistanche deserticola / Cai R // Phytother Res. — 2010. — Vol. 24. — P. 313-315.

143. Guo Y, Cao L, Zhao Q, et al. Preliminary characterizations, antioxidant and hepatoprotective activity of polysaccharide from Cistanche deserticola / Guo Y // Int J Biol Macromol. — 2016. — Vol. 93. — P. 678-685.

144. Shao B-M, Xu W, Dai H, et al. A study on the immune receptors for polysaccharides from the roots of Astragalus membranaceus, a Chinese medicinal herb / Shao B-M // Biochem Biophys Res Commun. — 2004. — Vol. 320. — P. 1103-1111.

145. Liu P, Zhao H, Luo Y. Anti-aging implications of Astragalus membranaceus (Huangqi): a well-known Chinese tonic / Liu P // Aging Dis. — 2017. — Vol. 8. — P. 868.

146. Zhang W-D, Chen H, Zhang C, et al. Astragaloside IV from Astragalus membranaceus shows cardioprotection during myocardial ischemia in vivo and in vitro / Zhang W-D // Planta Med. — 2006. — Vol. 72. — P. 4-8.

147. Lin E, Wang Y, Mehendale S, et al. Antioxidant protection by American ginseng in pancreatic ß-cells / Lin E // Am J Chin Med (Gard City N Y). — 2008. — Vol. 36. — P. 981-988.

148. Liu M, Xue M, Wang X-R, et al. Panax quinquefolium saponin attenuates cardiomyocyte apoptosis induced by thapsigargin through inhibition of endoplasmic reticulum stress / Liu M // J Geriatr Cardiol. — 2015. — Vol. 12. — P. 540.

149. Qin T, Ren Z, Liu X, et al. Study of the selenizing Codonopsis pilosula polysaccharides protects RAW264.7 cells from hydrogen peroxide-induced injury / Qin T // Int J Biol Macromol. — 2019. — Vol. 125. — P. 534-543.

150. Zhang H, Yang G, Sun H, et al. Application of reversed electroosmotic flow capillary electrophoresis in determination of chlorogenic acid in Eucommia ulmoides Olive leaf and its cortex cell culture / Zhang H // Anal Lett. — 1997. — Vol. 30. — P. 1293-1304.

151. Kulomaa A, Sirén H, Riekkola M-L. Identification of antioxidative compounds in plant beverages by capillary electrophoresis with the marker index technique / Kulomaa A // J Chromatogr A. — 1997. — Vol. 781. — P. 523-532.

152. Zhou J, Zhang T, Chen W, et al. Comparative analysis of chemical components between barks and leaves of Eucommia ulmoides Oliver / Zhou J // J Cent South Univ Technol. — 2009. — Vol. 16. — P. 371-379.

153. Xu D, Hu M-J, Wang Y-Q, et al. Antioxidant activities of quercetin and its complexes for medicinal application / Xu D // Molecules. — 2019. — Vol. 24. — P. 1123.

154. Enogieru AB, Haylett W, Hiss DC, et al. Rutin as a potent antioxidant: implications for neurodegenerative disorders / Enogieru AB // Oxid Med Cell Longev. — 2018. — Vol. 2018. — P. 6241017.

155. Hou P, Wang Q, Qi W, et al. Comprehensive determination of seven polyphenols in Eucommia ulmoides and its anti-oxidative stress activity in C. elegans / Hou P // J Food Meas Charact. — 2019. — Vol. 13. — P. 2903-2909.

156. Kenan Kinaci M, Erkasap N, Kucuk A, et al. Effects of quercetin on apoptosis, NF-κB and NOS gene expression in renal ischemia/reperfusion injury / Kenan Kinaci M // Exp Ther Med. — 2012. — Vol. 3. — P. 249-254.

157. Bukhari SB, Memon S, Mahroof-Tahir M, et al. Synthesis, characterization and antioxidant activity copper-quercetin complex / Bukhari SB // Spectrochim Acta A Mol Biomol Spectrosc. — 2009. — Vol. 71. — P. 1901-1906.

158. Fabre G, Bayach I, Berka K, et al. Synergism of antioxidant action of vitamins E, C and quercetin is related to formation of molecular associations in biomembranes / Fabre G // Chem Commun (Camb). — 2015. — Vol. 51. — P. 7713-7716.

159. Pawlikowska-Pawlęga B, Gruszecki WI, Misiak L, et al. Modification of membranes by quercetin, a naturally occurring flavonoid, via its incorporation in the polar head group / Pawlikowska-Pawlęga B // Biochim Biophys Acta Biomembr. — 2007. — Vol. 1768. — P. 2195-2204.

160. de Granada-Flor A, Sousa C, Filipe HAL, et al. Quercetin dual interaction at the membrane level / de Granada-Flor A // Chem Commun (Camb). — 2019. — Vol. 55. — P. 1750-1753.

161. Kosinova P, Berka K, Wykes M, et al. Positioning of antioxidant quercetin and its metabolites in lipid bilayer membranes: implication for their lipid-peroxidation inhibition / Kosinova P // J Phys Chem B. — 2012. — Vol. 116. — P. 1309-1318.

162. Patel RV, Mistry BM, Shinde SK, et al. Therapeutic potential of quercetin as a cardiovascular agent / Patel RV // Eur J Med Chem. — 2018. — Vol. 155. — P. 889-904.

163. Ademosun AO, Oboh G, Bello F, et al. Antioxidative properties and effect of quercetin and its glycosylated form (rutin) on acetylcholinesterase and butyrylcholinesterase activities / Ademosun AO // J Evid Based Complementary Altern Med. — 2016. — Vol. 21. — P. NP11-NP17.

164. Erlund I, Kosonen T, Alfthan G, et al. Pharmacokinetics of quercetin from quercetin aglycone and rutin in healthy volunteers / Erlund I // Eur J Clin Pharmacol. — 2000. — Vol. 56. — P. 545-553.

165. Kurisawa M, Chung JE, Uyama H, et al. Enzymatic synthesis and antioxidant properties of poly (rutin) / Kurisawa M // Biomacromolecules. — 2003. — Vol. 4. — P. 1394-1399.

166. Sanver D, Sadeghpour A, Rappolt M, et al. Structure and dynamics of dioleoyl-phosphatidylcholine bilayers under the influence of quercetin and rutin / Sanver D // Langmuir. — 2020. — Vol. 36. — P. 11776-11786.

167. Saponara S, Sgaragli G, Fusi F. Quercetin as a novel activator of L-type Ca2+ channels in rat tail artery smooth muscle cells / Saponara S // Br J Pharmacol. — 2002. — Vol. 135. — P. 1819-1827.

168. Cermak R, Kuhn G, Wolffram S. The flavonol quercetin activates basolateral K+ channels in rat distal colon epithelium / Cermak R // Br J Pharmacol. — 2002. — Vol. 135. — P. 1183-1190.

169. Gao S, Liu Z, Li H, et al. Cardiovascular actions and therapeutic potential of tanshinone IIA / Gao S // Atherosclerosis. — 2012. — Vol. 220. — P. 3-10.

170. Gao C, Xu T, Ye LL, et al. Traditional Chinese medicine for anti-arrhythmias: mechanisms via potassium channels / Gao C // Basic Clin Pharmacol Toxicol. — 2025. — Vol. 1. — P. e70059.

171. Shan H, Li X, Pan Z, et al. Tanshinone IIA protects against sudden cardiac death induced by lethal arrhythmias via repression of microRNA-1 / Shan H // Br J Pharmacol. — 2009. — Vol. 158. — P. 1227-1235.

172. Liang Q, Yang L, Wang Z, et al. Tanshinone IIA selectively enhances hyperpolarization-activated cyclic nucleotide-modulated (HCN) channel instantaneous current / Liang Q // J Pharmacol Sci. — 2009. — Vol. 110. — P. 381-388.

173. Huang Y, Ma S, Wang Y, et al. The role of traditional Chinese herbal medicines and bioactive ingredients on ion channels: a brief review and prospect / Huang Y // CNS Neurol Disord Drug Targets. — 2019. — Vol. 18. — P. 257-265.

174. Yan Z, Zhong L, Zhu W, et al. Chinese herbal medicine for the treatment of cardiovascular diseases - targeting cardiac ion channels / Yan Z // Pharmacol Res. — 2023. — Vol. 192. — P. 106765.

175. Evans R, O'neill M, Pritzel A, et al. Protein complex prediction with AlphaFold-Multimer / Evans R // biorxiv. — 2021. — P. 2021-10.

176. Mirdita M, Schütze K, Moriwaki Y, et al. ColabFold: making protein folding accessible to all / Mirdita M // Nat Methods. — 2022. — Vol. 19. — P. 679-682.

177. Pettersen EF, Goddard TD, Huang CC, et al. UCSF ChimeraX: structure visualization for researchers, educators, and developers / Pettersen EF // Protein Sci. — 2021. — Vol. 30. — P. 70-82.

178. DeLano WL. Pymol: an open-source molecular graphics tool / DeLano WL // CCP4 Newsl Protein Crystallogr. — 2002. — Vol. 40. — P. 82-92.

179. Humphrey W, Dalke A, Schulten K. VMD: visual molecular dynamics / Humphrey W // J Mol Graph. — 1996. — Vol. 14. — P. 33-38.

180. Jo S, Kim T, Iyer VG, et al. CHARMM-GUI: a web-based graphical user interface for CHARMM / Jo S // J Comput Chem. — 2008. — Vol. 29. — P. 1859-1865.

181. Morris GM, Huey R, Lindstrom W, et al. AutoDock4 and AutoDockTools4: automated docking with selective receptor flexibility / Morris GM // J Comput Chem. — 2009. — Vol. 30. — P. 2785-2791.

182. Trott O, Olson AJ. AutoDock Vina: improving the speed and accuracy of docking with a new scoring function, efficient optimization, and multithreading / Trott O // J Comput Chem. — 2010. — Vol. 31. — P. 455-461.

183. Abraham MJ, Murtola T, Schulz R, et al. GROMACS: high performance molecular simulations through multi-level parallelism from laptops to supercomputers / Abraham MJ // SoftwareX. — 2015. — Vol. 1-2. — P. 19-25.

184. Laskowski RA, Swindells MB. LigPlot+: multiple ligand-protein interaction diagrams for drug discovery / Laskowski RA // J Chem Inf Model. — 2011. — Vol. 51. — P. 2778-2786.

185. Wood CW, Woolfson DN. CCBuilder 2.0: powerful and accessible coiled-coil modeling / Wood CW // Protein Sci. — 2018. — Vol. 27. — P. 103-111.

186. Kim S, Thiessen PA, Bolton EE, et al. PubChem substance and compound databases / Kim S // Nucleic Acids Res. — 2016. — Vol. 44. — P. D1202-D1213.

187. Blum M, Andreeva A, Florentino LC, et al. InterPro: the protein sequence classification resource in 2025 / Blum M / Nucl. Acids Res. — 2025. — V.53 (D1). — P. D444–D456.

188. Laskowski RA, MacArthur MW, Moss DS, et al. PROCHECK: a program to check the stereochemical quality of protein structures / Laskowski RA // J Appl Crystallogr. — 1993. — Vol. 26. — P. 283-291.

189. Cole JC, Murray CW, Nissink JWM, et al. Comparing protein-ligand docking programs is difficult / Cole JC // Proteins. — 2005. — Vol. 60. — P. 325-332.

190. Jo S, Lim JB, Klauda JB, et al. CHARMM-GUI membrane builder for mixed bilayers and its application to yeast membranes / Jo S // Biophys J. — 2009. — Vol. 97. — P. 50-58.

191. Jorgensen WL, Chandrasekhar J, Madura JD, et al. Comparison of simple potential functions for simulating liquid water / Jorgensen WL // J Chem Phys. — 1983. — Vol. 79. — P. 926-935.

192. Huang J, Rauscher S, Nawrocki G, et al. CHARMM36m: an improved force field for folded and intrinsically disordered proteins / Huang J // Nat Methods. — 2017. — Vol. 14. — P. 71-73.

193. Klauda JB, Venable RM, Freites JA, et al. Update of the CHARMM all-atom additive force field for lipids: validation on six lipid types / Klauda JB // J Phys Chem B. — 2010. — Vol. 114. — P. 7830-7843.

194. Vanommeslaeghe K, MacKerell AD. Automation of the CHARMM general force field (CGenFF) I: bond perception and atom typing / Vanommeslaeghe K // J Chem Inf Model. — 2012. — Vol. 52. — P. 3144-3154.

195. Berendsen HJC, Postma JPM van, Van Gunsteren WF, et al. Molecular dynamics with coupling to an external bath / Berendsen HJC // J Chem Phys. — 1984. — Vol. 81. — P. 3684-3690.

196. Nosé S. A unified formulation of the constant temperature molecular dynamics methods / Nosé S // J Chem Phys. — 1984. — Vol. 81. — P. 511-519.

197. Parrinello M, Rahman A. Polymorphic transitions in single crystals: a new molecular dynamics method / Parrinello M // J Appl Phys. — 1981. — Vol. 52. — P. 7182-7190.

198. Darden T, York D, Pedersen L. Particle mesh Ewald: an N ·log(N) method for Ewald sums in large systems / Darden T // J Chem Phys. — 1993. — Vol. 98. — P. 10089-10092.

199. He F, Chen J, Dong K, et al. Multi-technical analysis on the antioxidative capacity and total phenol contents of 94 traditional Chinese dietary medicinal herbs / He F // Food Sci Nutr. — 2018. — Vol. 6. — P. 1358-1369.

200. Agil A, Fuller CJ, Jialal I. Susceptibility of plasma to ferrous iron/hydrogen peroxide-mediated oxidation: demonstration of a possible Fenton reaction / Agil A // Clin Chem. — 1995. — Vol. 41. — P. 220-225.

201. Ohkawa H, Ohishi N, Yagi K. Assay for lipid peroxides in animal tissues by thiobarbituric acid reaction / Ohkawa H // Anal Biochem. — 1979. — Vol. 95. — P. 351-358.

202. Kongmeneck AD, Kasimova MA, Tarek M. Modulation of the IKS channel by PIP2 requires two binding sites per monomer / Kongmeneck AD // BBA Adv. — 2023. — Vol. 3. — P. 100073.

203. Dellin M, Rohrbeck I, Asrani P, et al. The second PI(3,5)P2 binding site in the S0 helix of KCNQ1 stabilizes PIP2-at the primary PI1 site with potential consequences on intermediate-to-open state transition / Dellin M // Biol Chem. — 2023. — Vol. 404. — P. 241-254.

204. Lee S, Antony L, Hartmann R, et al. Conformational diversity in prion protein variants influences intermolecular β-sheet formation / Lee S // EMBO J. — 2010. — Vol. 29. — P. 251-262.

205. Sakuma K, Kobayashi N, Sugiki T, et al. Design of complicated all-α protein structures / Sakuma K // Nat Struct Mol Biol. — 2024. — Vol. 31. — P. 275-282.

206. Chung C-R, Tang Y, Chiu Y-P, et al. dbPTM 2025 update: comprehensive integration of PTMs and proteomic data for advanced insights into cancer research / Chung C-R // Nucleic Acids Res. — 2025. — Vol. 53. — P. D377-D386.

207. Zou X, Shanmugam SK, Kanner SA, et al. Divergent regulation of KCNQ1/E1 by targeted recruitment of protein kinase A to distinct sites on the channel complex / Zou X // Elife. — 2023. — Vol. 12. — P. e83466.

208. Ramasubramanian S, Rudy Y. The structural basis of IKs ion-channel activation: mechanistic insights from molecular simulations / Ramasubramanian S // Biophys J. — 2018. — Vol. 114. — P. 2584-2594.

209. Fusani L, Palmer DS, Somers DO, et al. Exploring ligand stability in protein crystal structures using binding pose metadynamics / Fusani L // J Chem Inf Model. — 2020. — Vol. 60. — P. 1528-1539.

210. Costa F, Ocello R, Guardiani C, et al. Integrated approach including docking, MD simulations, and network analysis highlights the action mechanism of the cardiac hERG activator RPR260243 / Costa F // J Chem Inf Model. — 2023. — Vol. 63. — P. 4888-4899.

211. Costa F, Guardiani C, Giacomello A. Molecular dynamics simulations suggest possible activation and deactivation pathways in the hERG channel / Costa F // Commun Biol. — 2022. — Vol. 5. — P. 165.

212. Liang F, Shi Y, Shi J, et al. Exploring the binding mechanism of pumpkin seed protein and apigenin: spectroscopic analysis, molecular docking and molecular dynamics simulation / Liang F // Food Hydrocoll. — 2023. — Vol. 137. — P. 108318.

213. Gao W-Y, Chen P-Y, Hsu H-J, et al. Tanshinone IIA downregulates lipogenic gene expression and attenuates lipid accumulation through the modulation of LXRα/SREBP1 pathway in HepG2 cells / Gao W-Y // Biomedicines. — 2021. — Vol. 9. — P. 326.

214. Liu J, Zhang C, Liu S, et al. Tanshinone IIA promotes apoptosis by downregulating BCL2 and upregulating TP53 in triple-negative breast cancer / Liu J // Naunyn Schmiedebergs Arch Pharmacol. — 2023. — Vol. 396. — P. 365-374.

215. Wang X, Zhang X, Li J, et al. Network pharmacology and LC-MS approachs to explore the active compounds and mechanisms of Yuanjiang decoction for treating bradyarrhythmia / Wang X // Comput Biol Med. — 2023. — Vol. 152. — P. 106435.

216. Chen D, Oezguen N, Urvil P, et al. Regulation of protein-ligand binding affinity by hydrogen bond pairing / Chen D // Sci Adv. — 2016. — Vol. 2. — P. e1501240.

217. Elebeedy D, Badawy I, Elmaaty AA, et al. In vitro and computational insights revealing the potential inhibitory effect of Tanshinone IIA against influenza A virus / Elebeedy D // Comput Biol Med. — 2022. — Vol. 141. — P. 105149.

218. Sharifpour S, Fakhraee S, Behjatmanesh-Ardakani R. Insights into the mechanism of inhibition of phospholipase A2 by resveratrol: an extensive molecular dynamics simulation and binding free energy calculation / Sharifpour S // J Mol Graph Model. — 2020. — Vol. 100. — P. 107649.

219. Dahiya R, Mohammad T, Roy S, et al. Investigation of inhibitory potential of quercetin to the pyruvate dehydrogenase kinase 3: towards implications in anticancer therapy / Dahiya R // Int J Biol Macromol. — 2019. — Vol. 136. — P. 1076-1085.

220. Boyer RF, Clark HM, LaRoche AP. Reduction and release of ferritin iron by plant phenolics / Boyer RF // J Inorg Biochem. — 1988. — Vol. 32. — P. 171-181.